

AN INVESTIGATION OF γ -Fe₂O₃
BY THE MÖSSBAUER EFFECT

A Thesis
submitted to the
Faculty of Graduate Studies
The University of Manitoba

In Partial Fulfillment of the
Requirements for the Degree of
Master of Science

by
R. J. Armstrong
Winnipeg, Manitoba, Canada
April 1967

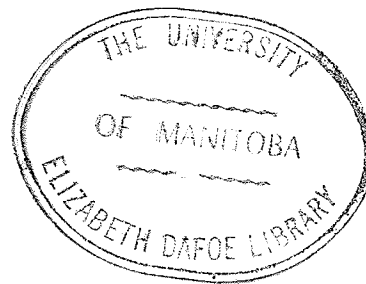


TABLE OF CONTENTS

	Page
LIST OF FIGURES	i
ACKNOWLEDGEMENTS	iii
ABSTRACT.	iv
I. INTRODUCTION	1
II. STRUCTURE OF Fe, α -Fe ₂ O ₃ , γ -Fe ₂ O ₃	2
2-1: Fe	2
2-1.1: Properties.	2
2-1.2: Ferromagnetism	2
2-2: α -Fe ₂ O ₃	5
2-2.1: Properties.	5
2-2.2: Antiferromagnetism	5
2-3: γ -Fe ₂ O ₃	5
2-3.1: Properties.	8
2-3.2: Ferrimagnetism	12
III. THE MÖSSBAUER EFFECT.	16
3-1: Introduction to the Mössbauer Effect	16
3-2: General Theory of the Mössbauer Effect	17
3-2.1: Resonance fluorescence	17
3-2.2: Cross section for resonance processes.	22
3-2.3: Lattice vibrations	26
3-2.4: Classical theory	28
3-2.5: Physical picture.. . . .	32
3-2.6: Fundamental theory	35
3-2.7: Nuclear properties	42

Table of Contents

	Page
3-3: Mössbauer Spectra	51
3-3.1: Introduction	51
3-3.2: Fe ⁵⁷ in unmagnetized Fe	51
3-3.3: Fe ⁵⁷ in α -Fe ₂ O ₃	55
3-3.4: Fe ⁵⁷ in γ -Fe ₂ O ₃	58
IV. EXPERIMENTAL TECHNIQUES	62
4-1: The Elron Mössbauer effect radiation analyzer	62
4-1.1: Description of apparatus	62
4-1.2: Theory of operation	65
4-2: Preparation of sources and absorbers	69
4-3: Experimental difficulties encountered and overcome	72
V. EXPERIMENTAL RESULTS AND DISCUSSION	76
5-1: Magnetic field determination	76
5-1.1: Data analysis procedures	76
5-1.2: Results and discussion	83
5-2: Temperature conversion rate determination	96
VI. SUMMARY	104
LIST OF REFERENCES	106

LIST OF FIGURES

FIGURE	PAGE
2-1 Cubic lattices, with lattice constant a	3
2-1 Structure of α -Fe ₂ O ₃	6
2-3 Magnetic structure of α -Fe ₂ O ₃	9
2-4 Crystal structure of γ -Fe ₂ O ₃	10
3-1 Decay of free atomic system by photon emission	18
3-2 Energy distributions involved in resonance fluorescence . .	20
3-3 Spectrum of a classical electromagnetic wave of finite length emitted by an Einstein solid	31
3-4 Co-ordinates employed in the determination of the transition matrix element	38
3-5 Experimental setup, emission and absorption lines, and velocity spectrum obtained in a typical Mössbauer transmission experiment	44
3-6 Details of isomeric shift	49
3-7 Properties of Fe ⁵⁷ bound in paramagnetic materials	52
3-8 Properties of Fe ⁵⁷ bound in unmagnetized iron	53
3-9 Properties of Fe ⁵⁷ bound in α -Fe ₂ O ₃	56
3-10 Properties of Fe ⁵⁷ bound in γ -Fe ₂ O ₃	59-60
4-1 Experimental Apparatus	63
4-2 Experimental Setup	64
5-1 Mössbauer spectrum of γ -Fe ₂ O ₃ in a 17kOe magnetic field provided by an electromagnet	84
5-2 The change in the effective magnetic field at the nucleus caused by an applied magnetic field	86
5-3 Mössbauer spectrum of α -Fe ₂ O ₃ with zero applied magnetic field	91

List of Figures

Figure	Page
5-4	97
5-5	100
5-6	102

5-4 Summary of results of the magnetic field determination

5-5 Mossbauer spectrum of β -Fe₂O₃ heated at 900°F for 15 hr. α peak 43% α -Fe₂O₃, 57% β -Fe₂O₃

5-6 Summary of results of the conversion rate determination

ACKNOWLEDGEMENTS

This thesis is based upon work performed in the Physics Department at The University of Manitoba from September 1964 to April 1967.

I would like to express my sincere appreciation to Dr. A. H. Morrish, my research supervisor, for his invaluable encouragement and helpful suggestions during the course of the research project.

I am indebted to my fellow graduate student, Mr. G. A. Sawatzky, without whose assistance this work could not have been completed.

Finally, my thanks to Mrs. B. Kischuk for typing the manuscript, to Miss F. E. Floweday for proofreading the typed copy, and to those individuals too numerous to mention here who have aided and contributed to this work over the past two years.

The financial assistance of the National Research Council of Canada is gratefully acknowledged.

ABSTRACT

An Investigation of γ -Fe₂O₃ by the Mössbauer Effect

by

R. J. Armstrong

The Mössbauer spectrum of γ -Fe₂O₃ was studied in the presence of an applied magnetic field. It was concluded that the zero-applied-field hyperfine fields at the tetrahedral and octahedral sites of the γ -Fe₂O₃ spinel crystal lattice are 489 ± 5 kOe and 499 ± 5 kOe respectively, the covalency of the tetrahedral ions is greater than that of the octahedral ions, and all the cation vacancies are located at the octahedral sites.

The Mössbauer spectrum of the reaction γ -Fe₂O₃ \longrightarrow α -Fe₂O₃ was studied with zero applied magnetic field. It was concluded that the reaction obeys the equation $m(T) = s \exp(-T_A/T)$ with $s = (6.6 \pm 0.5) \times 10^{18} \text{ hr}^{-1}$ and $T_A = (35.2 \pm 0.1) \times 10^3 \text{ }^\circ\text{K}$.

I. INTRODUCTION

Some aspects of γ -Fe₂O₃, a ferrimagnetic iron oxide of the spinel crystal structure, are investigated with the use of an Elron Electronic Industries Mössbauer Effect Radiation Analyzer.

The magnetic fields at the iron nuclei situated at the two different iron sites of the spinel lattice are determined for the two sites by splitting the γ -Fe₂O₃ Mössbauer spectrum with an applied magnetic field produced by a Magnion electromagnet. The resulting spectrum is separated into two distinct spectra by computer techniques, and the magnetic fields are calculated.

The rate of the reaction γ -Fe₂O₃ \longrightarrow α -Fe₂O₃ is studied at different temperatures by separating the Mössbauer spectrum of the α - γ mixture and evaluating the relative intensities of the two types of Fe₂O₃ present.

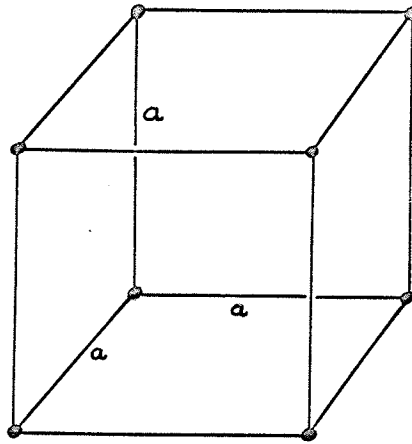
II. STRUCTURE OF Fe, α -Fe₂O₃, γ -Fe₂O₃

2-1: Fe

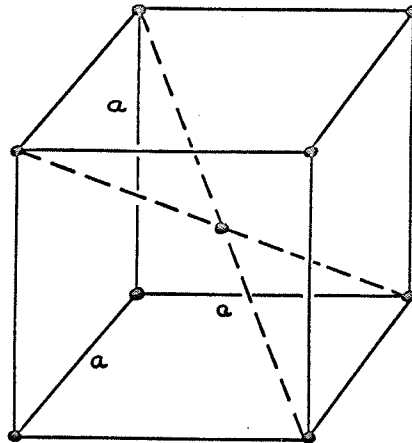
2-1.1: Properties. Fe occurs in one of four possible types of crystal structure, depending upon the temperature (Hodgman 1963 p. 2783). Below 800°C (α -Fe) its structure is bcc with a lattice constant of 2.86106 Å and with 2 atoms per unit cell. Between 800°C and 1100°C (β -Fe) its structure is bcc with a lattice constant of 2.90 Å and with 2 atoms per unit cell. Between 1100°C and 1425°C (γ -Fe) its structure is fcc with a lattice constant of 3.63 Å and with 4 atoms per unit cell. Above 1425°C (δ -Fe) its structure is bcc with a lattice constant of 2.93 Å and with 2 atoms per unit cell. See Fig. 2-1 (Dekker 1965 p. 7). While Fe does occur in the free state in nature (for example, in Greenland and Missouri), it is rare; in general, it occurs in the combined state. Fe is a silver-colored metal, has a density of 7.86 gm/cm³, and melts at 1535°C. Fe has a Curie temperature of 1043°K; below this temperature, it is ferromagnetic (Morrish 1965 p.270).

2-1.2: Ferromagnetism. (Morrish 1965 p. 259ff) A ferromagnetic material is one in which the strongly coupled atomic dipole moments tend to be aligned parallel. Thus, in such materials a spontaneous magnetization exists: there is a magnetic moment even in the absence of a magnetic field. Above an initial temperature T_f (the ferromagnetic Curie temperature), the spontaneous magnetization

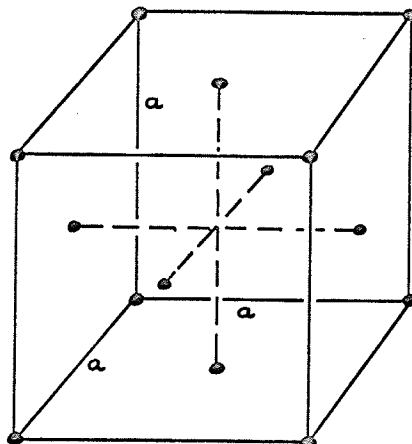
Fig. 2-1. Cubic lattices, with lattice constant a .



(1) Simple cubic.



(2) Body-centered cubic (bcc).



(3) Face-centered cubic (fcc).

vanishes. The material is then paramagnetic.

Classical Molecular Field Theory of Ferromagnetism

In a ferromagnetic material, the strong interaction tending to align the atomic dipoles parallel may be considered as equivalent to some internal magnetic field H_m . Assuming that H_m is proportional to the spontaneous magnetization M yields $H_m = N_w M$ (2-1). The constant of proportionality N_w is called the molecular field constant, and H_m is called the molecular field. In the presence of any applied magnetic field H , the actual field acting on a given dipole is $\vec{H}_T = \vec{H} + N_w \vec{M}$ (2-2). The demagnetizing field and the Lorentz (dipole-dipole) fields are omitted since their effects are small compared to the molecular field.

In order to obtain an idea of the order of magnitude of H_m , the following argument is considered:

The Curie point is the temperature at which the thermal agitation energy is sufficient to destroy the spontaneous magnetization. For Fe atoms with a dipole moment of 1 Bohr magneton and a Curie temperature $T_f \approx 10^3 \text{K}$, $\mu_B H_m \approx kT_f$ (2-3) yields $H_m \approx 10^7 \text{Oe}$. The field produced by the dipole-dipole interaction $\mu_B/a^3 \approx 10^3 \text{Oe}$ (where a is the lattice constant of the Fe unit cell) is much smaller than H_m . Since M is defined as the ratio of the magnetic moment of a small volume at some point to that volume, $M \approx \mu/a^3$ and thus the molecular field constant $N_w = H_m/M \approx 10^7 \text{Oe}/10^3 \text{Oe} = 10^4$ which is much larger than the Lorentz factor of $4\pi/3$.

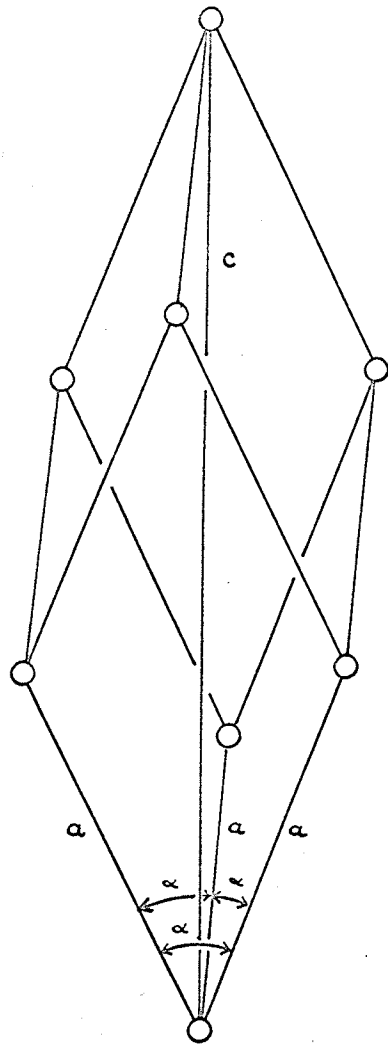
2-2: α -Fe₂O₃

2-2.1: Properties. α -Fe₂O₃ (hematite) occurs with the rhombohedral crystal structure (see Fig. 2-2). Its lattice constant is $a=5.42 \text{ \AA}$, its axial angle is $\alpha=55^{\circ}17'$, and it has 2 molecules per unit cell (Hodgman 1963 p. 2796). Hematite is found in nature in the free state, both as a powder and as large ($\cong 1\text{cm}^3$) single crystals (black diamond). Large ($\cong 1\text{cm}^3$) single crystals have been artificially grown by the flux technique (Curry et al. 1965) from powder. Large single crystals of hematite are black, but in powder form hematite is various shades of reddish brown, depending upon the particle size. Hematite is a nonconductor of electricity, is extremely hard and brittle, has a density of 5.24 gm/cm^3 , and melts at 1565°C .

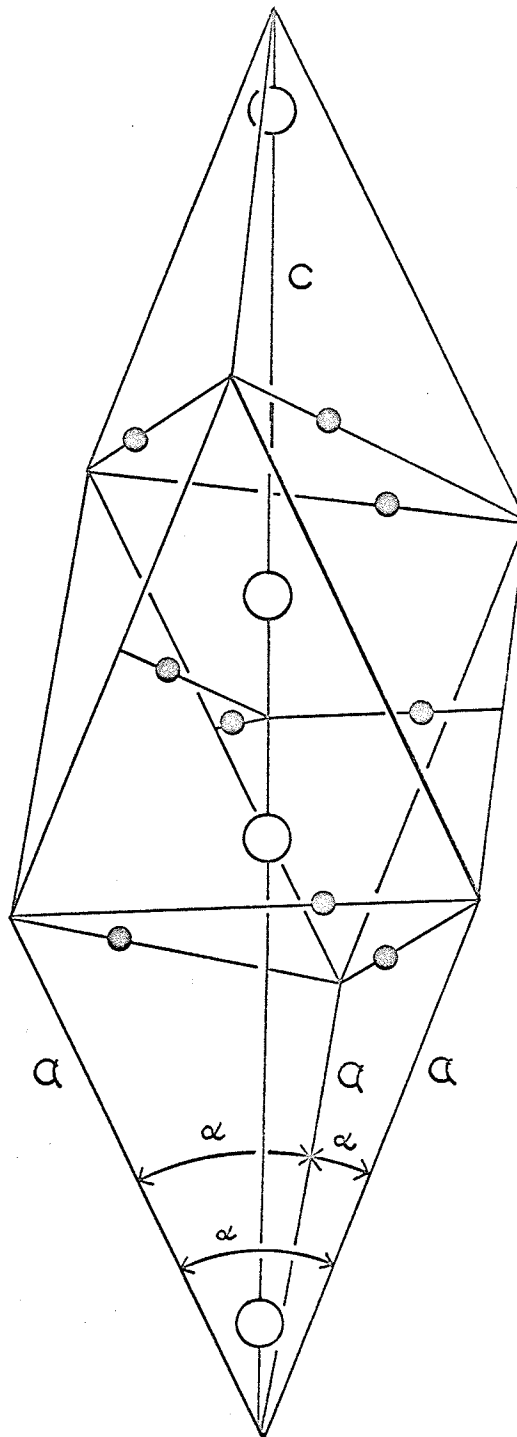
Hematite is an antiferromagnetic material which is weakly ferromagnetic in the region $263^{\circ}\text{K} < T < 945^{\circ}\text{K}$. Below 263°K , pure specimens appear to be purely antiferromagnetic, and above 945°K (the Néel temperature), hematite is paramagnetic (Morrish 1965 p. 479).

2-2.2: Antiferromagnetism. (Morrish 1965 p. 432ff) An antiferromagnetic material is one in which the strongly coupled atomic dipole moments are arranged in an antiparallel manner. In such materials the net spontaneous magnetization is zero: there is no magnetic moment in the absence of a magnetic field. Above a critical temperature T_N (the antiferromagnetic Néel temperature), the ordered

Fig. 2-2. Structure of $\alpha\text{-Fe}_2\text{O}_3$



(1) Rhombohedral lattice
(Dekker 1965 p.7)



(2) 1 unit cell of $\alpha\text{-Fe}_2\text{O}_3$

- - Cations (Fe^{3+})
- - Anions (O^{2-})

antiparallel arrangement of the dipoles disappears. The material is then paramagnetic.

Classical Molecular Field Theory of Antiferromagnetism

Only the simplest case, for illustrative purposes, will be developed here. Consider an antiferromagnetic material with two sublattices A and B. Specifically, let us choose the bcc lattice with the A lattice consisting of the corner positions and the B lattice the body positions. An atom at an A site has nearest neighbors that all lie on B sites and next nearest neighbors that all lie on A sites. A B site atom is in a similar environment. The molecular field \vec{H}_{mA} acting on an atom at an A site may be written

$$\vec{H}_{mA} = -N_{AA}\vec{M}_A - N_{AB}\vec{M}_B \quad (2-4)$$

where \vec{M}_A and \vec{M}_B are the magnetizations of the A and B sublattices, respectively; N_{AB} is a molecular field constant for the nearest neighbor interaction; and N_{AA} is a molecular field constant for the next nearest neighbor interaction. The molecular field \vec{H}_{mB} acting on an atom at a B site is similarly $\vec{H}_{mB} = -N_{BA}\vec{M}_A - N_{BB}\vec{M}_B$. Since the same type of atoms occupy the A and B lattice sites, $N_{AA} = N_{BB} = N_{ii}$, and $N_{AB} = N_{BA}$.

If a field is also applied, the fields \vec{H}_A and \vec{H}_B at an atom on the A and B lattices, respectively, are given by $\vec{H}_A = \vec{H} - N_{ii}\vec{M}_A - N_{AB}\vec{M}_B$ (2-5.1)

$$\text{and } \vec{H}_B = \vec{H} - N_{AB}\vec{M}_A - N_{ii}\vec{M}_B \quad (2-5.2)$$

The interaction between nearest neighbors is antiferromagnetic, thus $N_{AB} > 0$. However, N_{ii} may be +ve, -ve, or zero, depending upon the material in question.

Canted Spins

According to neutron diffraction experiments performed on α -Fe₂O₃ (Shull et al. 1951, Morrish et al. 1963), the magnetic moments lie in the (111) plane from 263°K to 945°K, whereas below 263°K they lie close to the [111] - (trigonal) - direction.

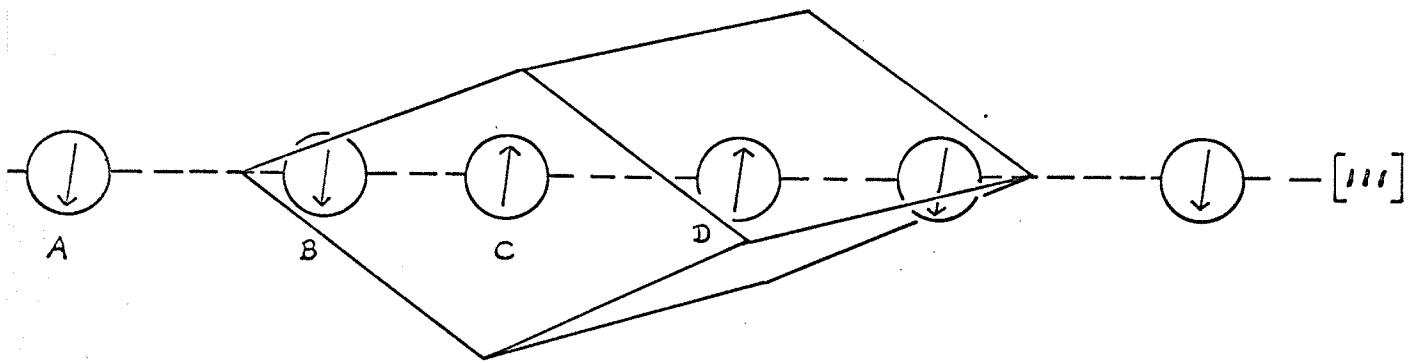
A mechanism to explain the presence of weak ferromagnetism for 263°K < T < 945°K has been proposed: a tilting of the magnetic moments towards one another will result in a net magnetic moment, as illustrated in Fig. 2-3 (Morrish 1965 p. 480). The Dzialoshinsky vector \vec{D} lies along the [111] direction. This is a purely phenomenological theory.

2-3: γ -Fe₂O₃

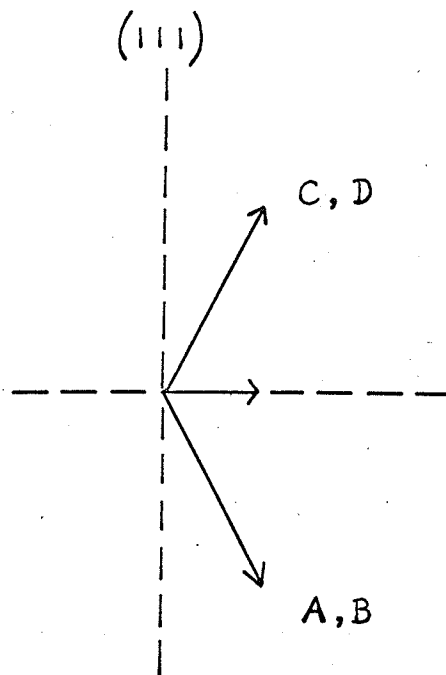
2-3.1: Properties. γ -Fe₂O₃ occurs with the spinel crystal structure (see Fig. 2-4). A description of this particular type of crystal structure follows (Goodenough and Loeb 1955).

Many oxides consist of a face-centered cubic lattice of O²⁻ ions which is held together by interstitial cations. There are two kinds of interstices between the elements of such a lattice: in the first, the cation is surrounded by 4 O²⁻ ions located at the corners of a tetrahedron (tetrahedral or A site: 4 nearest neighbors); in the second, the cation is surrounded by 6 O²⁻ ions located at the corners of an octahedron (octahedral or B site: 6 nearest neighbors). If all the tetrahedral sites are empty and all the octahedral sites

Fig. 2-3. Magnetic structure of $\alpha\text{-Fe}_2\text{O}_3$

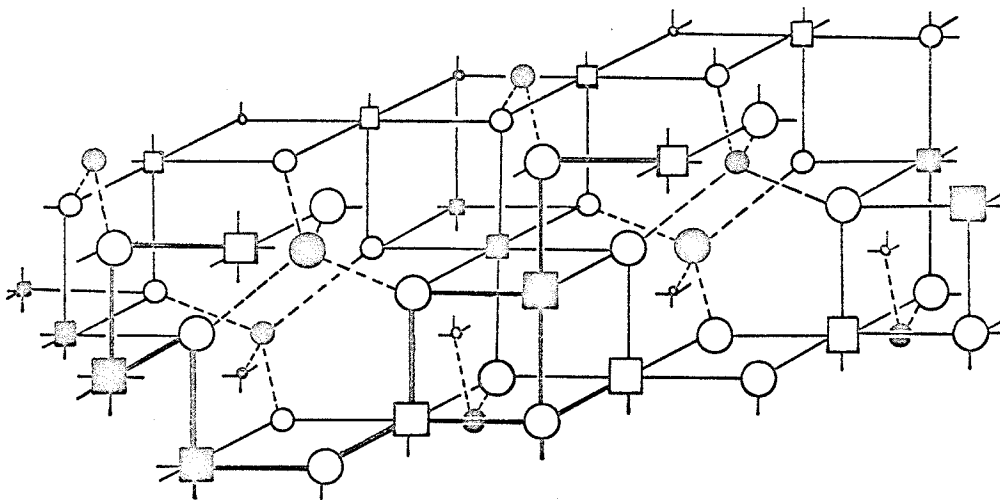


(1) The magnetic structure of $\alpha\text{-Fe}_2\text{O}_3$ for $263^\circ\text{K} < T < 945^\circ\text{K}$.
Only the Fe^{3+} ions in the rhombohedral unit cell are indicated.



(2) Weak ferromagnetism arising from canting of the atomic magnetic moments.

Fig. 2-4. Crystal structure of γ -Fe₂O₃



The spinel lattice, with ordering in the B sites

- , □ - octahedral cations
- - tetrahedral cations
- - anions

(Goodenough and Loeb 1955)

are filled, the crystal has the rock-salt structure. If only tetrahedral sites are occupied, the crystal has the zinc-blende structure. In oxides with the spinel structure there are cations in each type of interstice; twice as many octahedral as tetrahedral sites are occupied. The spinel lattice may be thought of as an ordered mixture of the zinc-blende and rock-salt structure.

There are two general classes which have the spinel lattice: the 2-4 spinel and the 2-3 spinel. The 2-4 spinel has the formula $2X^{2+}O \cdot Z^{4+}O_2$. In order to describe the cation distribution this may be written $Z[X_2]O_4$ or $X[Z_2]O_4$, where the ions within the parentheses occupy octahedral sites. The 2-3 spinel has the formula $X^{2+}O \cdot Y_2^{3+}O_3$, which may be written $X[Y_2]O_4$ or $Y[X_2]O_4$. If there is only one kind of cation in the octahedral sites, the spinel is called normal ($Z[X_2]O_4$ and $X[Y_2]O_4$). If there are equal numbers of both kinds of cations generally distributed at random in the octahedral sites, the spinel is called inverse ($X[Z_2]O_4$ and $Y[X_2]O_4$). If there is an unequal number of each kind of cation in the octahedral sites, the spinel is called mixed.

The smallest cubic unit cell consists of 8 molecules ($32 O^{2-}$ ions). Not all interstitials are occupied; those that are occupied have certain symmetry properties. Eight A sites and 16 B sites are occupied per unit cell. The length of an edge of the unit cell is approximately 8 \AA .

$\gamma\text{-Fe}_2\text{O}_3$ is an example of a 2-3 inverse spinel with vacancies in some of the usually occupied B sites (Henry and Boehm 1955, Ferguson

and Hass 1958). In the spinel notation, it is $\text{Fe}^{3+} \left[\square \frac{1}{3} \text{Fe}_5^{3+} \right] \text{O}_4$. Due to the 1:5 order on the B- sublattice (that is, the ratio of vacancies to ions), the c-axis is trebled and the structure becomes tetragonal with $a = 8.33 \text{ \AA}$, $c = 3a$ (Blasse 1964).

$\gamma\text{-Fe}_2\text{O}_3$ is found in nature in the free state as a reddish-brown powder; it may also be prepared chemically. However, no natural single crystals are known, and none has ever been grown artificially. $\gamma\text{-Fe}_2\text{O}_3$ is a poor conductor of electricity, and slowly converts irreversibly to $\alpha\text{-Fe}_2\text{O}_3$ upon being heated to 500°C .

$\gamma\text{-Fe}_2\text{O}_3$ has a Néel temperature of 1020°K . Below this temperature, it is ferrimagnetic (Morrish 1965 p. 507).

2-3.2: Ferrimagnetism. (Morrish 1965 p. 486ff) A ferrimagnetic material is one which, below a certain temperature T_{FN} (the ferrimagnetic Néel temperature), possesses a spontaneous magnetization that arises from a nonparallel arrangement of the strongly coupled atomic dipoles. Above this temperature it is paramagnetic. Ferrimagnetism was first found in crystals with the spinel crystal structure.

To consider a specific example, let us take a two-sublattice system with sublattices A and B, with the magnetic moments of one sublattice antiparallel to those of the other. There are several schemes which can lead to ferrimagnetism:

1. N magnetic ions per unit volume have identical moments at both A and B sites. In this case, suppose the fraction occupying A sites is λ , and the fraction occupying B sites is μ ($\lambda + \mu = 1$).

If $\lambda \neq \mu$, the material has a net moment. This unequal partitioning of the ions occurs if:

- (a) there are unequal numbers of sites on the 2 sublattices,
- and (b) the ions prefer the sites on one sublattice over those on the other.

This preference may be caused by:

- (i) the ion size in relationship to the ion site
- (ii) the electronic configuration of the ion
- (iii) the symmetry and strength of the crystalline field at a particular site.

If $\lambda = \mu$, the material is antiferromagnetic. There is no clear dividing line between ferrimagnetic materials and those antiferromagnetic materials which have a small net magnetic moment.

However, the magnetization of a ferrimagnetic material is usually assumed to be "appreciable", although this particular term has not been precisely defined.

2. The magnetic ions have unequal moments at the A and B sites. In this case, the material is ferrimagnetic except in one possible instance where λ and μ could have just the right values for the material to be antiferromagnetic. The unequal moments at the A and B sites may be caused by:

- 1. the same element in different ionic states, e.g. Fe^{2+} , Fe^{3+}
- 2. different elements in the same or different ionic states, e.g. Fe^{2+} , Co^{2+} or Fe^{3+} , Co^{2+} .
- 3. different crystalline fields acting at the 2 sites;

combinations of these 3 causes are frequent.

$\gamma\text{-Fe}_2\text{O}_3$ is an example of the first case, with an unequal

number of identical ions in the A and B sites. The theoretical magnetic moments in Bohr magnetons per formula unit at 0°K of the lattice sites are: A site, 5; B site, 8.3; net, 3.3. The experimental value is 3.2 (Morrish 1965 p. 507).

The Molecular Field Theory of Ferrimagnetism

For a ferrimagnet with 2 sublattices, the molecular fields are formally the same as those for an antiferromagnet. Considering a bcc lattice with the A lattice the corner positions and the B lattice the body positions, the equations are:

$$\vec{H}_{mA} = -N_{AA}\vec{M}_A - N_{AB}\vec{M}_B \quad (2-6.1)$$

$$\vec{H}_{mB} = -N_{BA}\vec{M}_A - N_{BB}\vec{M}_B \quad (2-6.2)$$

where \vec{H}_{mA} is the molecular field at an A site

\vec{H}_{mB} is the molecular field at a B site

\vec{M}_A is the magnetization of the A sublattice

\vec{M}_B is the magnetization of the B sublattice

N_{AB} is the molecular field constant for the nearest-neighbor (A-B) interaction

N_{BA} is the molecular field constant for the nearest-neighbor (B-A) interaction

N_{AA} is the molecular field constant for the next-nearest-neighbor (A-A) interaction

N_{BB} is the molecular field constant for the next-nearest-neighbor (B-B) interaction

At equilibrium, as before $N_{AB} = N_{BA}$. However, now $N_{AA} \neq N_{BB}$, since the sublattices are crystallographically inequivalent. In addition,

$M_A \neq M_B$. Applying a field \vec{H} , the resulting fields \vec{H}_A and \vec{H}_B at an atom on the A and B sublattices, respectively, are:

$$\begin{aligned}\vec{H}_A &= \vec{H} - N_{AA}\vec{M}_A - N_{AB}\vec{M}_B \\ \vec{H}_B &= \vec{H} - N_{AB}\vec{M}_A - N_{BB}\vec{M}_B\end{aligned}$$

Here $N_{AB} > 0$, since the interaction between the 2 sublattices is antiferromagnetic. In principle, the other molecular field constants, N_{AA} and N_{BB} , may be positive or negative; but, for the great majority of ferrimagnetic materials, are positive. Also, they are usually small compared to N_{AB} .

III. THE MÖSSBAUER EFFECT

3-1: INTRODUCTION TO THE MÖSSBAUER EFFECT

In 1957 R.L. Mössbauer discovered (1958a, 1958b, 1959) the physical phenomenon which now bears his name: the Mössbauer Effect. This phenomenon may be qualitatively described as follows: Nuclei embedded in solids can both emit and absorb low-energy gamma rays which display the natural line width and possess the full transition energy, without energy being transferred to lattice vibrations.

Mössbauer's discovery was accidentally made during the course of investigating nuclear resonance scattering of the Ir^{191} 129-keV gamma ray. At room temperature the emission and absorption spectra overlap considerably, since the free recoil energy is $\sim 0.05\text{eV}$ and the Doppler broadening is $\sim 0.1\text{eV}$, thereby permitting resonance scattering to be observed. When Mössbauer cooled both source and absorber in order to reduce residual scattering, instead of the expected decrease occurring, the scattering increased. Mössbauer then made an investigation of the nature of this surprising new effect, and was able to explain his experimental results.

The next major advance was the discovery of the Mössbauer Effect in Fe^{57} (Pound and Rebka 1959, Schiffer and Marshall 1959, Hanna et al. 1960, De Pasquali et al. 1960).

The Mössbauer Effect is easily demonstrated with Fe^{57} ; the

effect is very large, persists at temperatures over 1200°C, and has a very narrow natural linewidth --- the most accurately defined electromagnetic radiation available for physical experiments. These facts at once changed this particular field of physics from one accessible to only a few laboratories, to ones in which even modestly equipped groups could compete. It was soon realized that an elegant new research tool was available --- a tool simple in its basic ideas, requiring only a minimum of equipment, and allowing many applications in nuclear physics, relativity, and solid-state physics. Many more nuclei exhibiting recoilless resonance absorption were soon found and many new experiments were performed.

At present, the Mössbauer Effect, having evolved from a phenomenon worthy of study by itself, is used in many sectors of physics as an investigation technique.

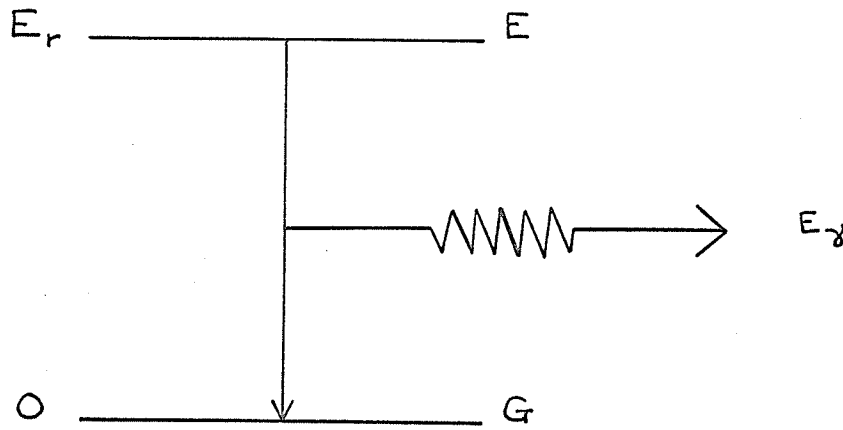
3-2: GENERAL THEORY OF THE MÖSSBAUER EFFECT
(Frauenfelder 1962 p. 1ff)

3-2.1: Resonance Fluorescence. In describing the mechanism of the Mössbauer Effect, it is first necessary to consider gamma ray emission by a free nucleus.

Consider a free atomic system at rest, of mass M , with 2 energy levels G and E separated by an energy E_x . When the system decays from E to G by emission of a photon of energy E_γ and momentum \vec{p} , the recoiling system receives an energy R and momentum \vec{P} .

(Fig. 3-1).

Fig. 3-1. Decay of free atomic system by photon emission



$$\text{Conservation of momentum yields } \vec{p} + \vec{P} = \vec{0} \quad (3-1)$$

$$\text{and Conservation of energy yields } E_{\gamma} = E_{\gamma} + R \quad (3-2)$$

$$\text{Thus } R = \frac{p^2}{2M} = \frac{p^2}{2Mc^2} = \frac{E_{\gamma}^2}{2Mc^2} \quad (3-3)$$

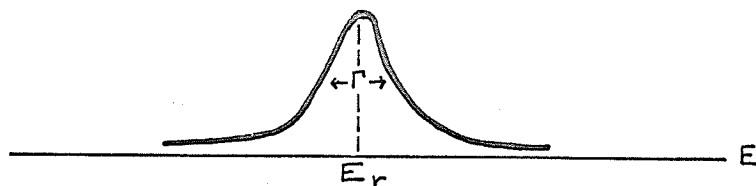
It has been assumed in stating these equations that the recoiling system may be treated nonrelativistically. This assumption is valid in both atomic and nuclear spectroscopy, since $E_{\gamma} \ll Mc^2$ in all cases. Thus, $R \ll E_{\gamma}$. Using this approximation in equation (3-3),

$$R = \frac{E_{\gamma}^2}{2Mc^2} = \frac{(E_{\gamma} - R)^2}{2Mc^2} \doteq \frac{E_{\gamma}^2}{2Mc^2} \quad (3-4)$$

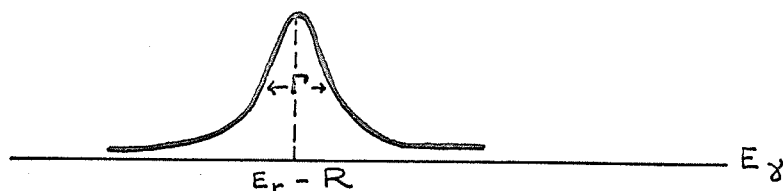
If the mean lifetime of the excited state E is τ , according to the Heisenberg uncertainty principle, the width Γ of the excited state E is given by $\tau \Gamma = \frac{\hbar}{2}$ (3-5). The energy E of the state is distributed about the center energy E_{γ} as shown in Fig. 3-2(1). According to equation (3-5), the energy of the stable ground state is sharp. Photons emitted in the $E \rightarrow G$ transition will therefore exhibit an energy distribution E_{γ} centered around $E_{\gamma} - R$, and displaying a "natural line shape" of width Γ (Fig. 3-2(2)).

When a photon of energy E_{γ} and momentum \vec{p} strikes a target of mass M initially at rest, by conservation of momentum all of \vec{p} is transferred to the target, which thus recoils with an energy R given by equation (3-4). Since this energy must be supplied by the gamma ray, only an energy $E_{\gamma} - R$ (Fig. 3-2(2)) is available for excitation. In order to excite an energy level E_{γ} , the incident γ -ray must have an energy $E_{\gamma} + R$ (Fig. 3-2(3)). Resonance fluorescence occurs only

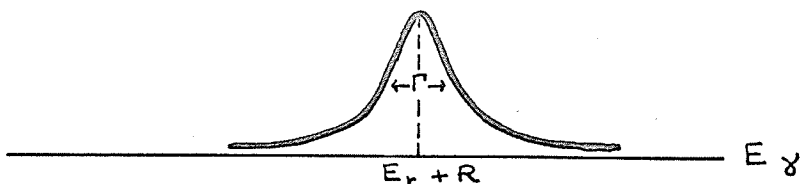
Fig. 3-2. Energy distributions involved in resonance fluorescence



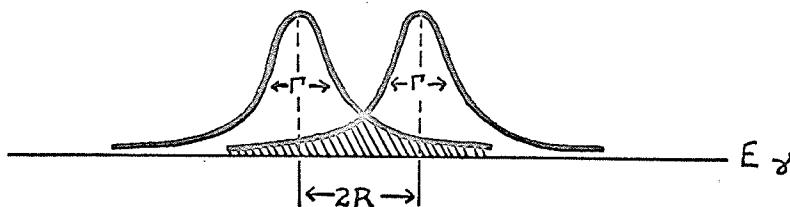
(1) Energy distribution of excited state E .



(2) Energy distribution of photons emitted in a transition $E \rightarrow G$.



(3) Energy spectrum required to excite state E in target and provide center-of-mass energy R .



(4) Overlap of (2) and (3).

if some of the incoming photons possess enough energy to simultaneously reach the state E and supply an energy R to the recoiling system. Accordingly, only the overlapping part of the two spectra ((2) and (3)) is responsible for resonance fluorescence (Fig. 2-3(4)). The necessary requirement for overlap to occur is evidently $2R \geq \Gamma$ (3-6). Optical transitions fulfil this requirement, but nuclear transitions do not.

The derivation of equations (3-2) to (3-6) assumed that both the emitting system and absorbing system were at rest. In reality, source and target atoms are in thermal motion; this motion introduces an additional broadening of the emission and absorption lines, termed Döppler broadening. In this case, the recoil energy R^1 is:

$$R^1 = \frac{|\vec{P} - \vec{p}|^2}{2M} - \frac{p^2}{2M} = \frac{p^2}{2M} - \frac{\vec{p} \cdot \vec{P}}{M} = R - \frac{\vec{p} \cdot \vec{P}}{M} \quad (3-7)$$

If φ is the angle between \vec{p} and \vec{P} , the second term on the right of equation (3-7), representing the Döppler broadening, may be written

$\frac{pP}{M} \cos \varphi$. The photon energy then is

$$E_{\gamma}^1 = E_x - R^1 = E_x - R + \frac{pP}{M} \cos \varphi \quad (3-8)$$

Since φ varies from 0 to 2π , there is a spread in the photon energy E_{γ}^1 of the order of $\frac{pP}{M}$. For optical radiation, the recoil energy R is small compared to the Döppler broadening, emission and absorption lines overlap, and resonance conditions are obtained. For gamma rays, the recoil energy is comparable to, or greater than, the Döppler broadening. Thus, in order to determine the conditions for the

occurrence of resonance fluorescence, an examination of the resonance fluorescence cross section under various conditions is required.

3-2.2: Cross section for resonance processes. When performing resonance experiments with gamma rays, either the scattered intensity or the attenuation of a beam due to resonance absorption is measured. The cross sections σ_s and σ_a of these two processes, for an incident gamma ray of energy E and wavelength λ are, for thin absorbers (Jackson 1955):

$$\sigma_s(E) = \sigma_0 \frac{\Gamma_2^2}{4(E-E_R)^2 + \Gamma^2} \quad (3-9.1)$$

$$\sigma_a(E) = \sigma_0 \frac{\Gamma \Gamma_2}{4(E-E_R)^2 + \Gamma^2} \quad (3-9.2)$$

where Γ is the total width of the absorption line, Γ_2 is its gamma ray width, and σ_0 is the maximum resonance cross section given by

$$\sigma_0 = \frac{2I_E + 1}{2I_G + 1} \frac{\lambda^2}{2\pi} \quad (3-10)$$

where I_G and I_E are the (nuclear) spins of the ground state G and excited state E respectively. Thus, both scattering and absorption cross sections exhibit a characteristic energy dependence of the

form $I(E) = \frac{\Gamma}{2\pi} \frac{1}{(E-E_R)^2 + (\frac{1}{2}\Gamma)^2}$ (3-11) which is normalized to

$\int_0^\infty I(E) dE = 1$ (3-12). This is the Lorentz distribution, and Γ is the full width of the distribution at half maximum. Curves corresponding to E_R , $E_R - R$, $E_R + R$ appear in Fig. 3-2.

For thin absorbers, the experimentally observed line shape

is the result (Wertheim 1964 p. 15) of a folding of the source and observer lines according to the equation

$$\sigma_{\text{expt}}(E) = \int_{-\infty}^{\infty} \omega(e) \sigma(E - e) de \quad (3-13)$$

where $\omega(e)$ is the spectral line shape of the emitted gamma ray:

$$\omega(e) = \frac{\Gamma_{\text{source}}^2}{\Gamma_{\text{source}}^2 + 4(e - E_0)^2} \quad (3-14)$$

and $\sigma(E)$ is the energy dependence of the absorption cross section (line shape of the absorption line) given by the Breit-Wigner formula (Abragam 1964 p. 6):

$$\sigma(E) = \sigma_0 \frac{\Gamma_{\text{absorber}}^2}{\Gamma_{\text{absorber}}^2 + 4(E - E_0)^2} \quad (3-15)$$

Integrating, we obtain

$$\sigma_{\text{expt}}(E) = \sigma_0 \frac{(\Gamma_{\text{source}} + \Gamma_{\text{absorber}})^2}{(\Gamma_{\text{source}} + \Gamma_{\text{absorber}})^2 + 4(E - E_0)^2} \quad (3-16)$$

Thus, the linewidths of the source and absorber are additive. If both source and absorber possess the natural linewidth, the experimentally observed Mössbauer linewidths is twice the linewidth of the gamma ray.

The equations for the cross sections are derived with the following assumptions:

1. There exists only one absorbing or scattering level.

Equations (3-9.1) and (3-9.2) must be modified if more than one state appears at, or close to, $E_{\mathbf{r}}$, or if the state at $E_{\mathbf{r}}$ is split into sublevels.

2. The level width is given entirely by decay processes.

In nuclei, the two competing modes are gamma-ray emission and internal conversion. Total width Γ and gamma-ray width Γ_γ are then related by the equation $\Gamma_\gamma = \frac{1}{1+\alpha} \Gamma$ (3-17) where α is the internal conversion coefficient. If other influences broaden the level, the line shape will not necessarily be Lorentzian.

3. The incoming photon is monoenergetic. Since a real source exhibits a continuous energy spectrum $I(E)$ where $I(E)dE$ is the number of gamma rays emitted with energies $E \rightarrow E + dE$, the cross sections must be averaged over the spectrum, yielding an effective

$$\text{cross section } \sigma_{\text{eff}} = \frac{\int_0^\infty \sigma(E) I(E) dE}{\int_0^\infty I(E) dE} \quad (3-18)$$

The following special cases of (3-18) will be examined:

3.1 The incoming γ -ray has an energy E_r ; its width is small compared to Γ , and the internal conversion coefficient $\alpha = 0$. In this case, essentially $I(E) = \delta(E - E_r)$ (3-19). Using equations (3-9.1), (3-9.2), (3-17), (3-18), (3-19), it follows that

$$\sigma_s(E_r) = \sigma_a(E_r) = \sigma_0 \quad (3-20).$$

This is the reason for designating σ_0 as the maximum resonance cross section.

3.2 The incoming γ -ray has a Lorentz energy spectrum $I(E)$ with a width Γ identical to the width of the absorbing state, and centered at E_r . When an experiment in which these assumptions are valid is performed, the recoil energy R is either negligible or has been compensated for, and the emitting and absorbing states are identical ---

that is, not broadened by external influences. From equations (3-9.2), (3-11), and (3-18) it follows that $\sigma_{\text{eff a}} = \frac{\sigma_0}{2} \frac{\Gamma_\gamma}{\Gamma} = \frac{\sigma_0}{2} \frac{1}{1+\alpha}$ (3-21).

It should be noted that Γ_γ is not an experimental width but a quantity characterizing the fraction of decays proceeding by photon emission. The actual widths of the incoming γ -ray and of the absorbing level are both given by Γ and not Γ_γ .

Equation (3-21) describes resonance absorption under the most ideal conditions:

- I. emission and absorption lines possess the natural line width
- II. emission and absorption lines are centered at the same energy.

For resonance fluorescence in the optical region, assumption II is valid but assumption I breaks down because the lines are considerably widened by Döppler broadening. In this case, the cross section can be calculated in the following manner:

Assume the target to be at rest, and the incoming photons to have an energy spectrum characterized by a Döppler width $\frac{pP}{M}$. Only a small part of the widened incoming spectrum overlaps with the resonance level. The fraction of incident photons capable of undergoing resonance absorption is approximately equal to $\Gamma / \frac{pP}{M}$. However, this fraction is centered at the resonance energy E_r and hence enjoys approximately the maximum resonance cross section $\sigma_0 \Gamma_\gamma / \Gamma$ given by equation (3-9.2) for $E = E_r$. The effective absorption cross section thus becomes:

$$\sigma_a^d \approx \sigma_0 \frac{\Gamma_\gamma}{\Gamma} \frac{\Gamma}{D} = \sigma_0 \frac{\Gamma_\gamma}{D} \quad (3-22)$$

$$D = pP/M \quad (3-23)$$

This estimate shows that the maximum cross section is reduced by a factor Γ_γ/D . Since internal conversion is impossible for optical transitions, $\alpha = 0$, and $\Gamma_\gamma = \Gamma$. Resonance experiments with optical transitions are feasible, and have been performed.

In nuclear experiments both conditions I and II do not hold. However, resonance experiments have been performed. To compensate for the recoil loss, the source can be mounted on the rim of a steel rotor which is driven at very high speeds. Gamma rays emitted tangentially thus gain sufficient energy for resonance absorption to occur. The recoil from a transition preceding the gamma ray to be investigated has been used to compensate for the recoil energy loss. Also, heating the source and absorber to increase the average kinetic energy has been done.

Even with these techniques, classical nuclear resonance fluorescence experiments are very difficult since I is not satisfied: the ratio $\Gamma_\gamma/pP/M$ is much smaller for nuclear transitions than for optical transitions.

3-2.3: Lattice Vibrations. The specific heat of solids decreases below a certain critical temperature. The first model to give an approximate prediction of this fact is the Einstein model (1906a, 1906b, 1911). A solid is assumed to contain a large number of independent linear oscillators, each vibrating with the same

frequency ω_E . This model predicted an exponential decrease of the specific heat at low temperatures, which was not in accordance with the experimentally observed T^3 dependence.

The Debye model (1912) predicted the T^3 dependence by introducing a continuum of oscillator frequencies with the distribution

$$C(\omega) = \begin{cases} \text{const.} \times \omega^2, & \omega \leq \omega_D \\ 0, & \omega > \omega_D \end{cases} \quad (3-24)$$

This distribution is derived by assuming the solid to be a homogeneous and isotropic medium, the group velocity of waves of all frequencies to be the same, and the total number of one-dimensional linear oscillators to be equal to three times the number N of atoms in a solid. While this model did predict the experimental data quite well, it was soon realized that the actual vibrational spectra deviate from an ω^2 - dependence at high frequencies, even though obeying at low frequencies. Calculations to find more detailed spectra were performed (Born and von Karman 1912, 1913); the spectra obtained exhibit a departure from those constructed assuming the Debye model.

For convenience the Debye model is often assumed to be valid. A temperature, characteristic of the material in question and called the Debye temperature Θ_D , is then defined by the equation $E_D = \hbar \omega_D = k \Theta_D$ (3-25). The Debye temperature can be experimentally determined from specific heat measurements, X-ray reflection, or elastic constants. However, the constant that appears in calculations of the Mössbauer effect must not be summarily identified with the Debye temperature as determined in a conventional

manner, without first making a careful investigation of the assumptions involved.

3-2.4: Classical Theory. The vector potential of an

electromagnetic wave, emitted by a classical oscillator of constant frequency ω_0 may be written as $\vec{A}(t) = \vec{A}_0 \exp(i\omega_0 t)$. (3-26)

Without loss of generality, we can assume $|\vec{A}(t)| = |\vec{A}_0| = 1$ (3-27)

If the frequency is a function of time, this equation is replaced by

$$\vec{A}(t) = \vec{A}_0 \exp\left[i \int_0^t \omega(t^1) dt^1\right] \quad (3-28).$$

If we assume for simplicity that the emitting oscillator moves in the x -direction

with a velocity $v(t) \ll c$, since the Döppler effect changes the frequency of the emitted wave, we have $\omega(t^1) = \omega_0 \left[1 + v(t^1)/c \right]$ (3-29).

Substituting (3-29) into (3-28) yields $\vec{A} = \vec{A}_0 \exp(i\omega_0 t) \exp[i\omega_0 x(t)/c]$

$$(3-30) \text{ or } \vec{A} = \vec{A}_0 \exp(i\omega_0 t) \exp[ix(t)/\lambda] \quad (3-31).$$

First, let us suppose the source of electromagnetic radiation moves in simple harmonic motion with a single frequency Ω and amplitude x_0 , that is $x = x_0 \sin \Omega t$ (3-33). This assumption corresponds to the Einstein model of a solid. The vector potential then

$$\text{becomes } \vec{A} = \vec{A}_0 \exp(i\omega_0 t) \exp(ix_0 \sin \Omega t / \lambda) \quad (3-34).$$

Using the expansion $\exp(iy \sin \theta) = \sum_{n=-\infty}^{\infty} J_n(y) \exp(in\theta)$ (3-35),

$$\text{equation (3-34) becomes } \vec{A} = \vec{A}_0 \sum_{n=-\infty}^{\infty} J_n(x_0/\lambda) \exp[i(\omega_0 + n\Omega)t]$$

(3-36). This is an electromagnetic wave, which is a superposition of partial waves with frequencies $\omega_0, \omega_0 \pm \Omega, \omega_0 \pm 2\Omega, \dots$. The amplitude of each wave is given by the Bessel function $J_n(x_0/\lambda)$.

The unshifted line is identified with the Mössbauer line; its intensity

is $f = |\vec{A}(n=0)|^2 = J_0^2 \left(\frac{x_0}{\lambda} \right)$ (3-37), which is also the emission probability of the unshifted component, since \vec{A} is normalized.

In order to use the above discussion for real solids, equations (3-33), (3-34), and (3-36) must be generalized to correspond to the correct frequency spectrum. To do this, the single frequency Ω and amplitude x_0 are replaced by a sum over frequencies Ω_m , with corresponding amplitudes x_m . Equation (3-37) then becomes

$$f = \prod_{m=1}^{3N} J_0^2 \left(\frac{x_m}{\lambda} \right) \quad (3-38).$$

The number $3N$ of frequencies in a

solid is very large. Each of the $J_0 \left(\frac{x_m}{\lambda} \right)$ is only slightly different from unity since the maximum amplitude x_m of each individual frequency component is extremely small. Thus J_0 can be expanded $J_0(y) = 1 - \frac{1}{4} y^2 + \dots$ (3-39) and equation (3-38) can be written $\ln f = 2 \sum_m \ln J_0 \simeq 2 \sum_m \ln \left[1 - \frac{1}{4} \left(\frac{x_m^2}{\lambda^2} \right) \right]$ (3-39).

Using $\ln(1-y) = -y + \dots$ this reduces to $\ln f \simeq -2 \sum_m \frac{1}{4} \left(\frac{x_m^2}{\lambda^2} \right)$ (3-40), since $x_m \ll \lambda$. In this expression, we see that f is a function

of the maximum excursions x_m . The mean-square deviation of the vibrating atom from its equilibrium position is $\langle x^2 \rangle = \frac{1}{2} \sum_m x_m^2$ (3-41). Substituting this into equation (3-40) we get $\ln f \simeq -\langle x^2 \rangle / \lambda^2$.

This equation is exact in the limit $N \rightarrow \infty$. Thus, the final result may be written $f = \exp(-\langle x^2 \rangle / \lambda^2)$ (3-42).

The following comments may be made regarding equation (3-42):

1. While it is not surprising that the classical treatment yields an unshifted line, the exact agreement between the classical

expression of equation (3-42) and the quantum mechanical result which follows directly from equation (3-68) is unexpected.

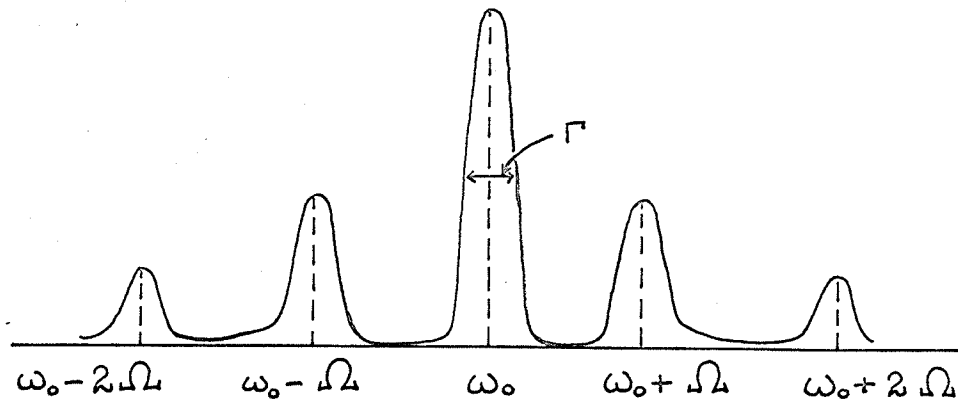
2. Equation (3-42) permits a simple physical interpretation: the continuously emitted electromagnetic wave comes from a region with linear dimensions $\langle x^2 \rangle^{\frac{1}{2}}$. If this linear dimension increases beyond the wavelength $\lambda = \lambda/2\pi$, pieces of the wave train emitted from different points in this region interfere destructively, and the fraction f of photons emitted without energy loss decreases rapidly.

3. The condition for appreciable emission without energy loss (that is, the amplitude of the emitting atom is small compared to the wavelength of the emitted photon) means that small spatial zero-point vibrations are essential for a large Mössbauer effect. The Heisenberg uncertainty principle then necessitates large zero-point momenta.

4. The wave train described by equation (3-34) is infinitely long, and the corresponding emission line infinitely narrow. In decays with a mean life τ , the lines have a width Γ according to equation (3-5), and the spectrum for an Einstein solid (corresponding to equation (3-36)) is of the form shown in Fig. 3-3. It is evident that the Mössbauer line will be distinct only if the line width is smaller than the separation from the first satellite ($\Gamma < \frac{1}{2} \Omega$); that is, if the nuclear lifetime is larger than the characteristic lattice time ($\tau > 1/\Omega$).

5. In order to describe an actual solid, which has interactions among the oscillators, it is necessary to revise Fig. 3-3

Fig. 3-3. Spectrum of a classical electromagnetic wave of finite length emitted by an Einstein solid.



since that figure is based upon the Einstein model with non-interacting oscillators. Whether an Einstein model with interactions or a Debye model is used to represent a real solid, the result is that only the unshifted line shows the natural width Γ ; all the satellites are broadened, overlap each other, and give rise to a continuum.

3-2.5: Physical Picture. Let us now examine what happens when the nucleus of an atom which is imbedded in a solid decays by gamma emission. Were the nucleus free, it would receive a recoil momentum \vec{p} and a recoil energy R , given by equation (3-3). Since the atom is bound in the solid, both the recoil momentum and energy are affected by this fact. Three topics will be considered: conservation of momentum, conservation of energy, and times involved.

1. Conservation of Momentum

Three possibilities exist. 1) The momentum may go into translational motion of the nucleus. The energy required to leave a lattice site is $\approx 10\text{eV}$, while the energy available from the recoil is $\approx 0.1\text{eV}$. Thus this possibility is eliminated from consideration. 2) The momentum may go into phonons (lattice vibrations). This is impossible, since the expectation value of the momentum for lattice vibrations vanishes. 3) The momentum may go into translational motion of the entire crystal. This must be the correct answer, for there are no other possibilities. Thus the momentum is unchanged, but is eventually taken up by the solid as a whole --- if the crystal is attached to a larger body, the earth, for example, the larger body

takes up the momentum.

2. Conservation of Energy

Four possibilities exist. The transition energy can be shared among the gamma ray, the individual atom, lattice vibrations, and the solid as a whole. In the previous section we saw that the atom does not leave its lattice site and thus does not acquire translational energy. The energy that goes into motion of the entire solid is negligible. In practice, therefore, the transition energy is divided between the gamma ray and the phonons. A Mössbauer transition occurs if the state of the lattice remains unchanged: that is, the gamma ray gets the entire transition energy.

For an Einstein solid, the smallest amount of energy that can be given to the solid is $E_E = \hbar \omega_E = k \Theta_E$ (3-43). If the recoil energy of a free nucleus is small compared to this excitation energy ($R \ll k \Theta_E$), the phonon emission probability will be small, the lattice will remain unexcited, and the gamma ray will leave possessing the full transition energy.

For a Debye solid, the problem is not so straightforward. First, let us assume that the decay takes place in such a way that a lattice vibration of the maximum energy (the shortest possible wavelength) is excited, $E_D = \hbar \omega_D = k \Theta_D$ (3-44). If this particular lattice wave were the only one to be excited, the Debye case would be no different from the Einstein case. However, while longer wavelength and therefore lower energy modes exist, they are not easily excited,

thus making a Mössbauer effect possible.

In the above it has been assumed that the oscillators are at a temperature of 0°K , where they are in their ground state. At finite temperatures, some of the oscillators are excited, and transitions with induced emission of phonons become possible.

While the foregoing discussion is evidently oversimplified and treats a quantum mechanical problem in a classical way, its essence is valid. Even though the characteristic energies for the solid are much smaller than the nuclear transition energy, and the nuclear decay occurs in one nucleus only, the entire crystal must be considered as the quantum mechanical system in which the decay occurs.

3. Time Considerations

If it is desired to ascertain whether or not a transition with energy transfer ΔE to the lattice has occurred, the energy of the photon or of the solid must be measured to within ΔE . The time T required for this measurement is given by the uncertainty principle, $T \cong \hbar / \Delta E = \lambda / u$ (3-45) where $2\pi\lambda$ is the wavelength belonging to a phonon with energy ΔE and velocity u . During the time T , the disturbance caused by the decay travels a distance L given by $L = Tu \cong \lambda$ (3-46). Thus, regions in the solid of linear dimensions λ or larger must be examined if one wishes to determine whether or not an amount of energy ΔE has been transferred to the lattice.

Measurement can not determine whether the original recoil

has been imparted to the decaying nucleus only, or has been shared among two, three, or more atoms within a region of linear dimensions λ .

The recoil energy given to the entire solid is approximately

$$R_{\text{solid}} = R_{\text{free atom}} \left(\frac{M_{\text{atom}}}{M_{\text{solid}}} \right) \approx R \left(\frac{d}{D} \right)^3 \quad (3-47)$$

where R is the recoil energy, d is the lattice parameter, and D is the linear dimension of the solid. The Debye energy is $E_D = \hbar W_D = \hbar u/\lambda \approx 2\pi\hbar u/2d$ (3-48),

and the recoil energy is of the same order of magnitude $R \approx \hbar u/d$

(3-49). The time required to measure the recoil energy of the entire

solid is, according to the uncertainty principle, $T_s \geq \hbar/R_{\text{solid}} \approx$

$$\hbar D^3/Rd^3 \approx D^3/ud^2 \quad (3-50),$$

and the time t for a signal with the sound velocity u to travel the linear dimension D is $t = D/u$ (3-51).

Thus the approximate ratio of the two times becomes $T/t \approx (D/d)^2$ (3-52).

Hence, the time required for a measurement of the recoil energy of the entire solid is very much larger than the time needed for a signal to travel through the crystal. After the measurement of the recoil energy is performed, the crystal is moving with uniform velocity (assuming it is cemented down). Thus it is impossible to tell how parts of the solid far away from the decaying nucleus "know" when and how to move.

3-2.6: Fundamental Theory. The theory of the Mössbauer effect involves calculating the probability for emission or absorption of a gamma ray from a nucleus embedded in a solid, with the lattice simultaneously undergoing a transition from one state to another. The

essential fact used is that the transition probability for a given transition is proportional to the square of the matrix element connecting the two states involved in the transition.

The probability for a transition in which the nucleus decays from the excited state N_i to the ground state N_f , while simultaneously, the lattice goes from its initial state L_i to its final state L_f , is

$$W(N_f \leftarrow N_i, L_f \leftarrow L_i) = \text{const.} \times |\langle f | H_{\text{int}} | i \rangle|^2 \quad (3-53)$$

where $|i\rangle$ and $\langle f|$ denote the initial and final states of the entire system, including the lattice, and H_{int} is the interaction hamiltonian responsible for this decay. The energy that can be transferred to the lattice during this transition is very small compared to the gamma ray energy. The dependence of the density of final states $\rho(E)$ on the energy transfer to the lattice is hence very small, $\rho(E)$ is assumed to be constant, and is absorbed into the constant in equation (3-53).

In order to perform calculations, an explicit form of the transition matrix element is required. This may be obtained as follows:

The hamiltonian for a particle of charge e , mass m which moves with momentum \vec{p} in an electromagnetic field specified by the vector potential \vec{A} and scalar potential ϕ , is $H = \frac{1}{2m} (\vec{p} - \frac{e}{c} \vec{A})^2 + e\phi$ (3-54) (Schiff 1955 p. 135). The term $(\vec{p} - \frac{e}{c} \vec{A})^2$ leads, in a first approximation, to the nonrelativistic interaction hamiltonian

$H_{\text{int}} = \text{constant} \times (\vec{p} \cdot \vec{A} - \vec{A} \cdot \vec{p})$. (3-55) When \vec{A} is expanded into plane waves, it is found that

$$\langle f | H_{\text{int}} | i \rangle = \text{constant} \times \langle f | \exp(i\vec{k} \cdot \vec{x}) p_A | i \rangle \quad (3-56),$$

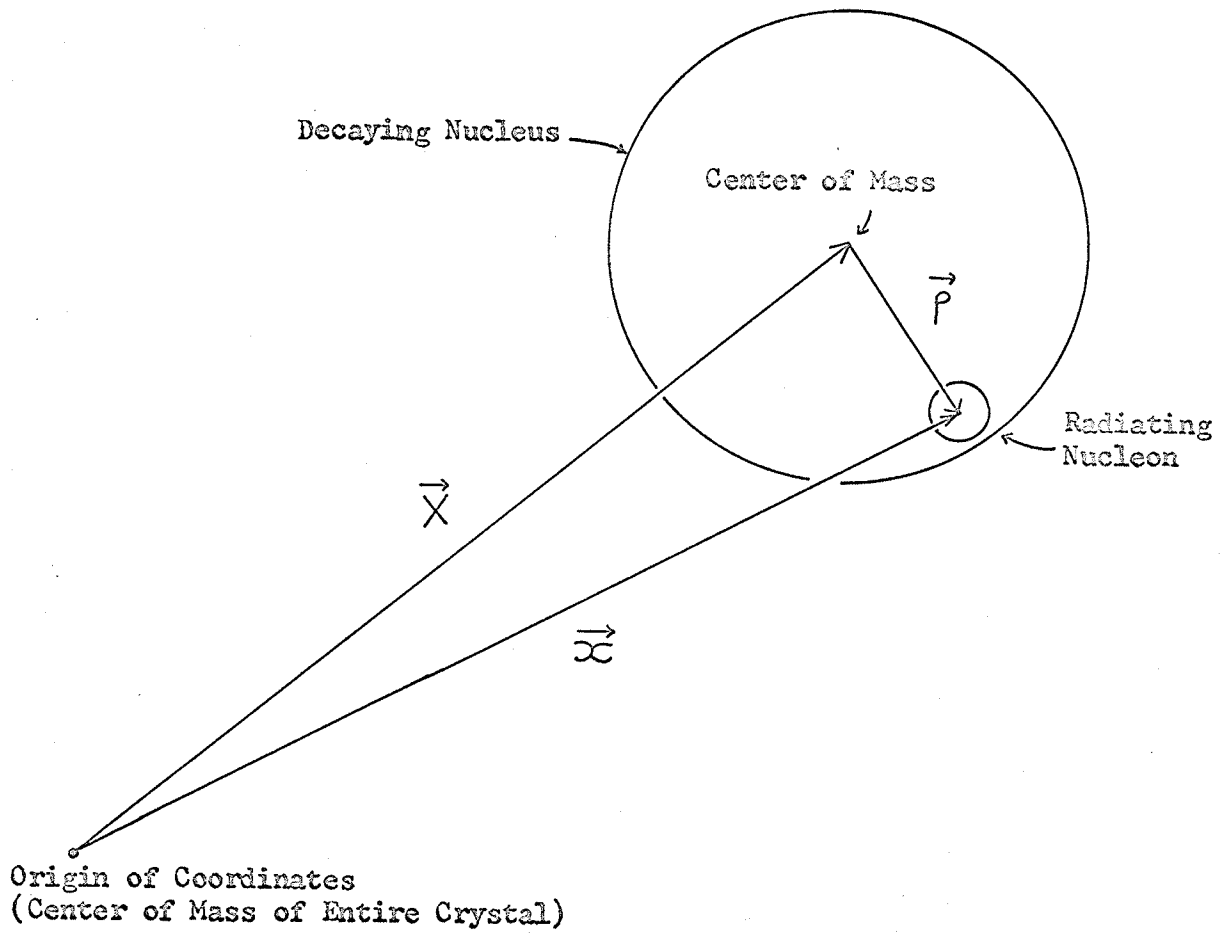
where the gradient operator p_A must be applied in the direction of the polarization vector of the electromagnetic wave $\vec{k} = \vec{p}/\hbar$, and where \vec{x} is the co-ordinate vector of the decaying nucleon. Equation (3-56) represents a single-particle description of the nucleus. If the decay occurs through many nucleons in the same nucleus, equation (3-56) must be modified by an appropriate sum over these nucleons being introduced. In the present case, this sum is omitted for simplicity.

Since the nuclear forces are strong and of short range, we can use the approximation that the nuclear decay is not influenced by the state of the lattice, and the lattice condition does not depend on the nuclear state. The state functions $|i\rangle$ and $\langle f|$ can then be written as products $|N_i\rangle |L_i\rangle$ and $\langle L_f| \langle N_f|$ of nuclear-state functions $|N_i\rangle$ and $\langle N_f|$ and lattice-state functions $|L_i\rangle$ and $\langle L_f|$, with $\langle L_f | L_i \rangle = \delta_{fi}$ and $\langle N_f | N_i \rangle = \delta_{fi}$.

Internal nuclear co-ordinates $\vec{\rho}$ are introduced (Fig. 3-4) by writing $\vec{x} = \vec{X} + \vec{\rho}$ (3-57) where \vec{X} is the co-ordinate vector of the center of mass of the decaying nucleus. The origin of co-ordinates is located at the center of mass of the entire crystal. The momentum operator is split into $p_A = p_X + p_\rho$ (3-58) where p_X acts on the center of mass co-ordinates of the nucleus, and p_ρ acts on the internal nuclear co-ordinates.

Substituting equations (3-57) and (3-58) into equation (3-56),

Fig. 3-4. Coordinates employed in the determination of transition matrix element.



the matrix element is separated into two parts, each part consisting of a product of a nuclear and a lattice matrix element:

$$\begin{aligned} \langle f | H_{\text{int}} | i \rangle = \text{constant} \times & \left\{ \langle N_f | e^{i\vec{k} \cdot \vec{p}_p} | N_i \rangle \langle L_f | e^{i\vec{k} \cdot \vec{X}} | L_i \rangle \right. \\ & \left. + \langle N_f | e^{i\vec{k} \cdot \vec{p}} | N_i \rangle \langle L_f | e^{i\vec{k} \cdot \vec{X}} |_{p_X} | L_i \rangle \right\} \quad (3-59). \end{aligned}$$

Using the closure $\sum_{n'} |n'\rangle \langle n'| = 1$ (3-60)

where the summation extends over all intermediate states, the ratio Υ_L of the lattice matrix elements in the two terms of equation (3-59) can be written

$$\Upsilon_L = \frac{\langle L_f | e^{i\vec{k} \cdot \vec{X}} |_{p_X} | L_i \rangle}{\langle L_f | e^{i\vec{k} \cdot \vec{X}} | L_i \rangle} = \frac{\sum_{L'} \langle L_f | e^{i\vec{k} \cdot \vec{X}} | L' \rangle \langle L' | p_X | L_i \rangle}{\langle L_f | e^{i\vec{k} \cdot \vec{X}} | L_i \rangle} \quad (3-61).$$

The momentum $\hbar \vec{k}$ transferred to the lattice during the nuclear decay is much larger than typical momenta components in the lattice.

Because of this, it can be said, even without detailed calculation, that the terms $\langle L_f | \exp(i\vec{k} \cdot \vec{X}) | L' \rangle$ for allowed intermediate states L' are of the same order of magnitude as the term

$\langle L_f | \exp(i\vec{k} \cdot \vec{X}) | L_i \rangle$. Thus they can then be taken out from under the summation sign, leading to

$$\Upsilon_L \approx \sum_{L'} \langle L' | p_X | L_i \rangle = \langle p_L \rangle \quad (3-62) \text{ where } \langle p_L \rangle \text{ denotes an average over lattice momentum components.}$$

Using the closure again, the ratio Υ_N of the nuclear matrix elements in the two terms of equation (3-59) can be written

$$\tau_N = \frac{\langle N_f | e^{i\vec{k}\cdot\vec{p}_p} | N_i \rangle}{\langle N_f | e^{i\vec{k}\cdot\vec{p}} | N_i \rangle} = \frac{\sum_{N'} \langle N_f | e^{i\vec{k}\cdot\vec{p}} | N' \rangle \langle N' | p_p | N_i \rangle}{\langle N_f | e^{i\vec{k}\cdot\vec{p}} | N_i \rangle} \quad (3-63).$$

In this case, the momentum transfer $\hbar\vec{k}$ is much smaller than typical nuclear momentum components. Thus the terms $\langle N_f | e^{i\vec{k}\cdot\vec{p}} | N' \rangle$ for allowed intermediate states N' are of the same order of magnitude as the term $\langle N_f | e^{i\vec{k}\cdot\vec{p}} | N_i \rangle$. Taking them out from under the summation sign in a manner similar to that employed above, τ_N becomes

$$\tau_N \approx \sum_{N'} \langle N' | p_p | N_i \rangle = \langle p_N \rangle \quad (3-64),$$

where $\langle p_N \rangle$ denotes an average over nuclear momentum components.

Using equations (3-62) and (3-64), the ratio of the first and second terms in equation (3-59) is $\frac{\tau_N}{\tau_L} \approx \frac{\langle p_N \rangle}{\langle p_L \rangle}$ (3-65), which is of the order of at least 10^5 . Therefore, the second term can be neglected with respect to the first term, and equation (3-59) reduces to, in good approximation,

$$\langle f | H_{int} | i \rangle = \text{const.} \times \langle L_f | e^{i\vec{k}\cdot\vec{X}} | L_i \rangle \langle N \rangle \quad (3-66)$$

where $\langle N \rangle$ represents the nuclear matrix element $\langle N_f | e^{i\vec{k}\cdot\vec{p}_p} | N_i \rangle$ which depends only on nuclear properties. $\langle L_f | e^{i\vec{k}\cdot\vec{X}} | L_i \rangle$ is the matrix element for transfer of a momentum $\hbar\vec{k}$ to the lattice through the atom of the decaying nucleus, with the lattice going from the state L_i to L_f . Using equation (3-66), we can now easily calculate f , the fraction of gamma rays emitted without energy loss to the

lattice ($L_f \leftarrow L_i$):

$$f = \frac{|\langle L_i | e^{i\vec{k}\cdot\vec{X}} | L_i \rangle|^2}{\sum_{L_f} |\langle L_f | e^{i\vec{k}\cdot\vec{X}} | L_i \rangle|^2} \quad (3-67)$$

Examining the denominator of equation (3-67), and using equation (3-60):

$$\begin{aligned} \sum_{L_f} |\langle L_f | e^{i\vec{k}\cdot\vec{X}} | L_i \rangle|^2 &= \sum_{L_f} \langle L_f | e^{i\vec{k}\cdot\vec{X}} | L_i \rangle \langle L_f | e^{i\vec{k}\cdot\vec{X}} | L_i \rangle^* \\ &= \sum_{L_f} \langle L_i | e^{-i\vec{k}\cdot\vec{X}} | L_f \rangle \langle L_f | e^{i\vec{k}\cdot\vec{X}} | L_i \rangle \\ &= \langle L_i | e^{-i\vec{k}\cdot\vec{X}} e^{i\vec{k}\cdot\vec{X}} | L_i \rangle \\ &= \langle L_i | L_i \rangle \\ &= 1 \end{aligned}$$

$$\text{Thus } f = |\langle L_i | e^{i\vec{k}\cdot\vec{X}} | L_i \rangle|^2 \quad (3-68).$$

This is the equation which is generally used for most calculations of the fraction of gamma rays emitted or absorbed without energy loss.

By integrating the matrix element $\langle L_i | \exp(i\vec{k}\cdot\vec{X}) | L_i \rangle$ over all lattice variables except \vec{X} , one obtains $f = \left| \int e^{i\vec{k}\cdot\vec{X}} \rho(\vec{X}) d^3X \right|^2$ (3-69)

where $\rho(\vec{X})$ is the probability of finding the radiating nucleus at a distance \vec{X} from its equilibrium position. This shows that f is the square of the Fourier transform of the probability density $\rho(\vec{X})$.

Two applications of equation (3-68) will now be briefly discussed.

1. The Einstein Solid

The ground state wave function for a linear harmonic oscillator of mass M and angular frequency ω is given by

$$\Psi_0(X) = \sqrt{\frac{M\omega}{\pi\hbar}} e^{-M\omega X^2/2\hbar} \quad (3-70).$$

Substituting equation (3-70) into equation (3-68) and replacing $\vec{k}\cdot\vec{X}$ by kX since this is a one dimensional problem, integrating yields the following for f :

$$f = \exp(-\frac{1}{2}k^2/2M\hbar\omega) = \exp(-R/\hbar\omega_D) \quad (3-71).$$

2. The Debye Solid

In this case, the individual atoms do not all have the same frequency, thus making the calculations more complicated. However, they have been performed, and the result is $f = e^{-2W}$ (3-72) where

$$W = \frac{3R}{k\Theta_D} \left[\frac{1}{4} + \left(\frac{T}{\Theta_D}\right)^2 \int_0^{\frac{\Theta_D}{T}} \frac{x dx}{e^x - 1} \right] \quad (3-73).$$

$$\text{At } T = 0^{\circ}\text{K}, \quad f = \exp\left(-\frac{3}{2}R/\hbar\omega_D\right) \quad (3-74).$$

This result is valid only for those materials where the concept of the Debye temperature is applicable. However, the Debye approximation is very useful for obtaining an idea of the order of magnitude of expected effects.

3-2.7: Nuclear Properties. (Wertheim 1964 p. 72ff)

The Mössbauer effect can be used to determine nuclear moments and

isomeric shifts.

Consider a nuclide with spin \vec{I} and magnetic dipole moment

$\vec{\mu}_n$. The hamiltonian describing the interaction of the magnetic dipole moment with a magnetic field \vec{H}_n is $\mathcal{H}_m = -\vec{\mu}_n \cdot \vec{H}_n$ (3-75).

The corresponding energy levels are

$$E_{m_I} = -\mu_n H_n m_I / I, \quad m_I = -I, -I+1, \dots, +I \quad (3-76).$$

Thus there are $2I+1$ equally-spaced levels of separation $g = \mu_n H_n / I$ (3-77).

In the Mössbauer effect, the gamma ray studied corresponds to a transition from a magnetic sublevel of the excited state E to a magnetic sublevel of the ground state G. Three cases will be examined for illustrative purposes.

1. The magnetic field at the nucleus vanishes: $\vec{H}_n = \vec{0}$.

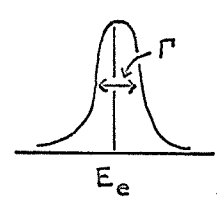
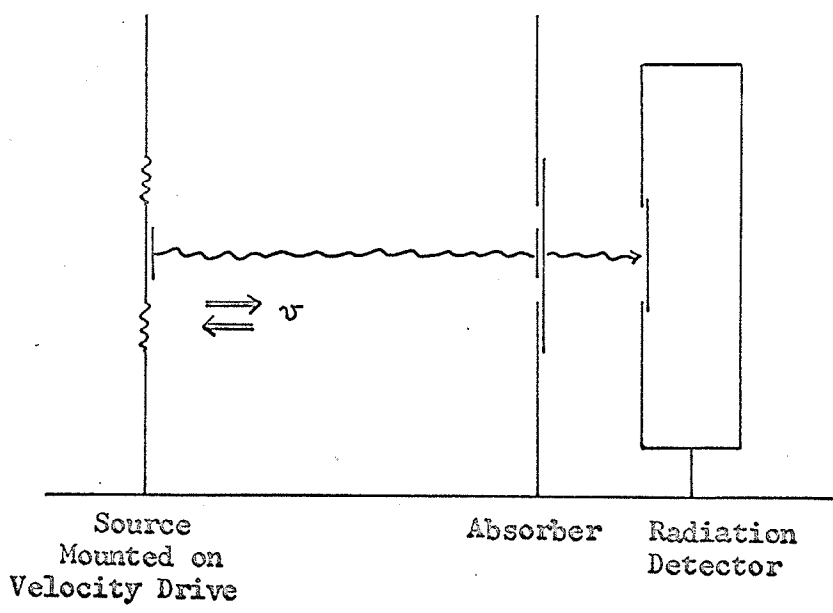
In this case the excited and ground states are $(2I_E+1)$ - and $(2I_G+1)$ -fold degenerate, and the emission and absorption lines are unsplit.

2. The magnetic field at the nucleus of the source or absorber is finite, and the nucleus has zero spin in the ground state ($I_G = 0$).

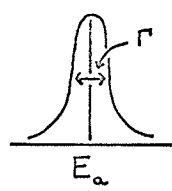
In this case, the excited and ground states are nondegenerate, and the emission or absorption line (which one depends upon whether the field is applied to the source or absorber; it is desirable to have either the source or absorber unsplit) will be split into $2I_E + 1$ equally spaced components with separation $g_E = \mu_n H_n / I_E$ (3-78).

If the separation g_E is larger than the width 2Γ of the overlap line (Fig. 3-5), that is, if $\mu_n H_n / I_E \geq 2\Gamma = 2\frac{\hbar}{\tau}$ (3-79), the number of components can be counted, thus enabling the spin I_E to be

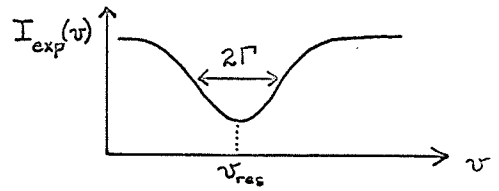
Fig. 3-5. Experimental setup, emission and absorption lines, and velocity spectrum obtained in a typical Mössbauer transmission experiment.



Emission line



Absorption line



Experimental Velocity Spectrum

found. If the magnetic field H_n is known, the magnetic moment μ_{nE} can then be found: $\mu_{nE} = \frac{g_E}{H_n} I_E$ (3-80).

If equation (3-79) does not hold, I_E can not be determined by counting the components, but an approximate value of μ_{nE} can be obtained by measuring the increase in linewidth as a function of increasing H_n .

3. The magnetic field at the nucleus is finite, and the nucleus has nonzero spin in both the ground and excited states.

This is the general case. Nonzero groundstate spin produces more than $2I_E + 1$ components. However, usually groundstate spin and moment can be determined with conventional techniques, thus simplifying the task of analyzing the spectrum. Polarization experiments can reduce the number of components, thereby facilitating identification, while the presence of very strong internal magnetic fields in ferro-, ferri-, antiferro-, and paramagnetic substances introduces complications, it does allow the determination of magnetic moments which would otherwise be difficult to find.

The effective magnetic field acting upon the nucleus is produced (Watson and Freeman 1961) by means of various magnetic **interactions** (Wertheim 1964 p. 76).

The Fermi contact interaction, the direct coupling between the nucleus and an s-electron, yields a magnetic field

$$H_S = -\frac{16\pi}{3} \mu \left\langle \sum (s\uparrow - s\downarrow) \right\rangle \quad (3-81)$$

where $s\uparrow$ and $s\downarrow$ are the s-electron spin densities at the nucleus

with spin up and spin down respectively, and μ is the Bohr magneton.

The orbital magnetic moment gives rise to a field

$$\vec{H}_L = -2\mu \langle 1/r^3 \rangle \langle \vec{L} \rangle \quad (3-82)$$

where \vec{L} is the atomic orbital angular momentum quantum number.

For trivalent iron in a weak crystal field environment, $H_L = 0$ since $L = 0$ in this case.

The dipolar interaction with the spin of the parent atom produces a magnetic field

$$\vec{H}_D = -2\mu \langle 3\vec{r}(\vec{S} \cdot \vec{r})/r^5 - \vec{S}/r^3 \rangle \quad (3-83)$$

where \vec{S} is the atomic spin angular momentum quantum number.

This term vanishes in a cubic metal in the absence of spin-orbit coupling.

The effective magnetic field acting upon the nucleus should not be confused with the internal field; the internal field exists everywhere inside the solid, while the effective magnetic field is largely the result of the interaction of the nucleus with its own electrons. The internal field H_i is a direct result of the application of an external field H_o , taking into account the Lorentz and demagnetizing fields:

$$H_i = H_o + \frac{4}{3}\pi M - DM \quad (3-84)$$

where M is the magnetization

and D is the demagnetization factor.

In order to investigate the quadrupole coupling $e\vec{Q} \cdot \nabla \vec{E}$ where $e\vec{Q}$ is the nuclear electric quadrupole moment and $\nabla \vec{E}$ the electric field gradient at the nuclear site, the source or absorber nuclei must

placed in an environment with a high electric field gradient, and the resulting splitting must be measured. To find either $e\vec{Q}$ or $\nabla\vec{E}$, one must be known or calculated, for only the product can be determined by the Mössbauer effect.

There also exists instances of a superposition of magnetic hyperfine and electric quadrupole interaction.

Frequency shifts can also be caused by the influence of temperature upon the motion of the nuclei in the solid. A consideration of the second-order Doppler effect is required (Pound and Rebka 1960)

$$\text{and yields } \frac{1}{\nu} \frac{\partial \nu}{\partial T} = - \frac{C_L}{2Mc^2} \quad (3-85)$$

where C_L is the specific heat of the lattice, and M is the gram atomic weight. The same equation may be deduced by regarding the shift as due to a relativistic time dilation (Josephson 1960). In the high-temperature classical limit where $C_L = 3R$, $\frac{1}{\nu} (\partial \nu / \partial T)_{T \rightarrow \infty} = -2.44 \times 10^{-15}/\text{OK}$. This is sufficient for it to be necessary to take the temperature coefficient of frequency into account in accurate measurements.

When a change in the nuclear radius occurs without a change in nucleon number as the nucleus goes from one state to another, the corresponding shift in energy is called an isomeric shift. The requirements for a nuclear isomeric shift to occur are:

1. the two nuclear states involved must have different charge distributions.
2. there must be electronic wave functions (usually from

s-electrons) which overlap appreciably with the nuclear wave functions.

3. these wave functions must be sensitive to external (chemical) changes.

To determine the shift of the nuclear energy levels, the following procedure is used:

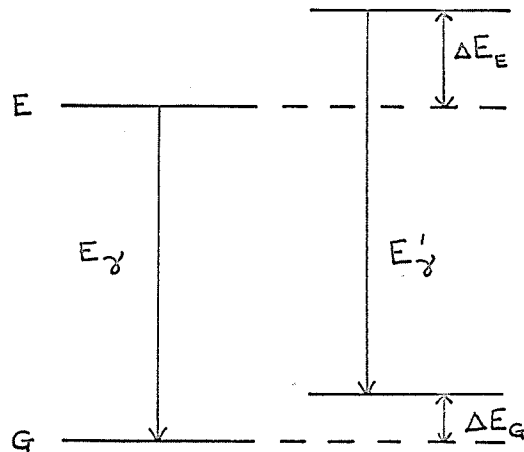
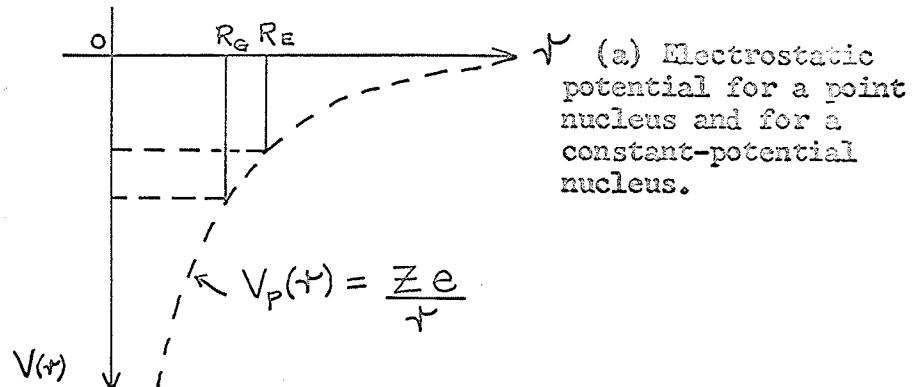
First, consider a point nucleus of charge $Z e$ with two levels G and E separated by E_γ . The electrostatic potential is $V_p(r) = Z e/r$ (3-86) (See Fig. 3-6(a)).

Next, consider another nucleus of equal charge but with radius R_G in the ground state G, and radius R_E in the excited state E. The two levels will lie higher for this nucleus than for the point nucleus, because of the diminished interaction with the electrons. To find the shift ΔE_G , it is necessary to determine the contribution to the total energy of the system which comes from the electrostatic interaction. Since the potential difference from R_G to ∞ is the same for both the point nucleus and finite nucleus, only the volume from 0 to R_G must be accounted for when determining the energy shift.

Assuming that the wave function $\Psi(r)$ of the relevant electrons is essentially constant over the distances involved, we can replace it with the constant $\Psi(0)$, and write the contribution from this volume to the interaction energy as $E(R_G) = -\int_0^{R_G} eV(r) |\Psi(0)|^2 4\pi r^2 dr$

(3-87) where $V(r)$ is the electrostatic potential created by the nucleus.

Fig. 3-6. Details of isomeric shift.



(b) Level shifts from point nucleus to finite nucleus.

For a point nucleus, $V_p(r) = Ze/r$ (3-86), and equation (3-87) becomes $E_p(R_G) = -2\pi Ze^2 R_G^2 |\psi(0)|^2$ (3-88).

For a finite nucleus, the energy depends upon the charge distribution. Assuming the surface-charge model (the electrostatic potential is constant from the center to the nuclear surface, and joins the outside potential at $r=R$; this potential is shown in Fig. 3-6(a)), equation (3-87) becomes

$$E_s(R_G) = -(4/3)\pi Ze^2 R_G^2 |\psi(0)|^2 \quad (3-89).$$

The difference between equations (3-88) and (3-89) yields the shift

$$\Delta E_G = E_s(R_G) - E_p(R_G) = (2/3)\pi Ze^2 R_G^2 |\psi(0)|^2 \quad (3-90).$$

A more realistic calculation, performed assuming a nuclear charge density $\rho(r)$ instead of a surface charge, yields a result of the same form as equation (3-90) but with R_G^2 replaced by

$$\langle R_G^2 \rangle = \frac{1}{Ze} \int \rho(r)r^2 dv = \frac{4\pi}{Ze} \int \rho(r)r^4 dr \quad (3-91).$$

Thus the transition energy between 2 levels E and G becomes

$$E'_\gamma = E_\gamma + \Delta E_E - \Delta E_G = E_\gamma + \frac{2}{3}\pi Ze^2 |\psi(0)|^2 [\langle R_E^2 \rangle - \langle R_G^2 \rangle] \quad (3-92).$$

In general, it is ordinarily impossible to observe such a small energy change. However, in a Mössbauer experiment with the source and absorber in different chemical environments such that the wave functions at the nuclei in the emitter e and absorber a are different, the difference in gamma ray energy $s_I(a,e)$ is given by equation (3-92) as $s_I(a,e) = E_a - E_e = \frac{2}{3}\pi Ze^2 [\langle R_E^2 \rangle - \langle R_G^2 \rangle] \left\{ |\psi(0)_a|^2 - |\psi(0)_e|^2 \right\}$ (3-93).

Equation (3-93) is the justification for the three requirements listed above. It predicts the correct order of magnitude for the isomeric shift. Thus, measurement of the isomeric shift permits the determination of information about differences in nuclear radius between ground and excited state, and about changes in the wave function of s-electrons for various substances.

3-3: MÖSSBAUER SPECTRA

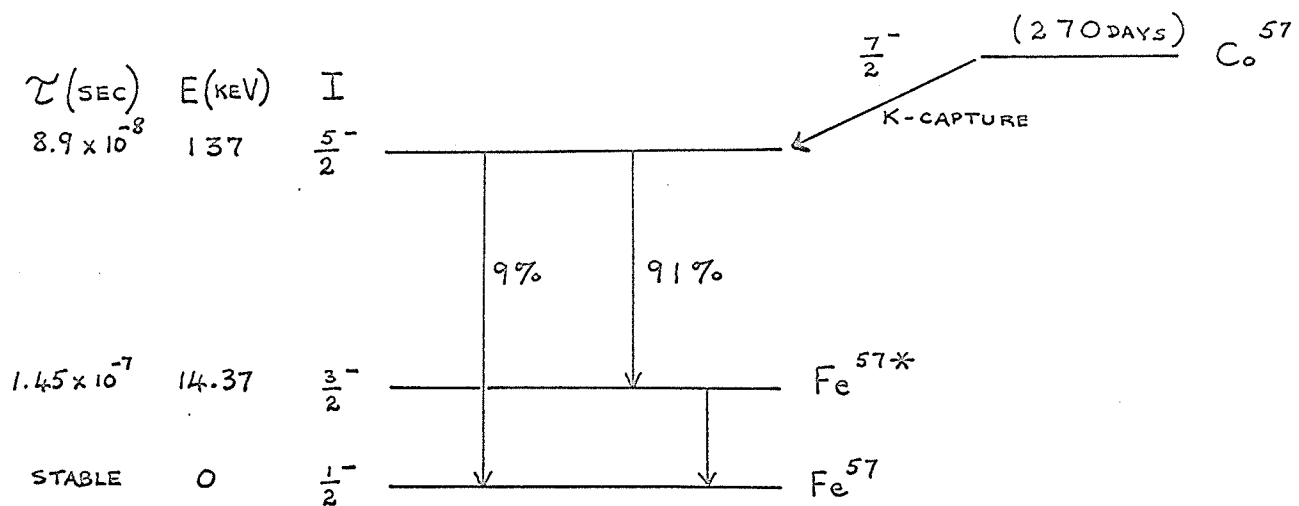
The isomer shift, hyperfine splitting, and quadrupole shift for Fe, α -Fe₂O₃, and γ -Fe₂O₃ are described below.

3-3.1: Introduction. The majority of Mössbauer experiments have been performed with Fe⁵⁷, since it is a stable isotope occurring with a natural abundance of 2.14%, has a suitable lifetime and energy in its first excited state, and the parent isotope Co⁵⁷ has a long lifetime, 270 days. Its decay scheme is presented in Fig. 3-7(a).

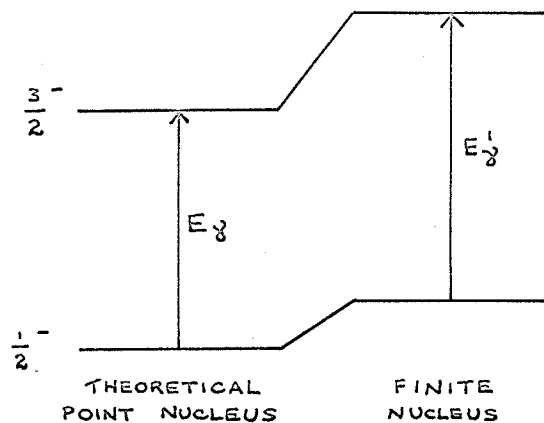
In most experiments it is preferable to use a line source; that is, the emitting Fe⁵⁷ atoms are bound in a paramagnetic solid like stainless steel, copper, or palladium, and the levels are unsplit. The resulting energy level diagram and absorption spectra are presented in Figs. 3-7(b) and (c) respectively.

3-3.2: Fe⁵⁷ in Unmagnetized Fe. For Fe⁵⁷ bound in unmagnetized iron, the energy level diagram and absorption spectrum are shown in Fig. 3-8.

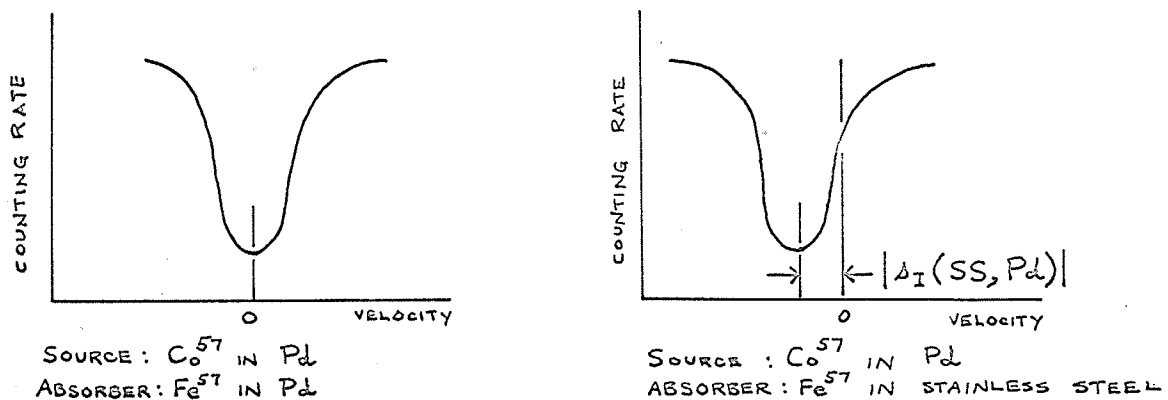
Fig. 3-7. Properties of Fe^{57} bound in paramagnetic materials



(a) The decay of Co^{57} to Fe^{57} .

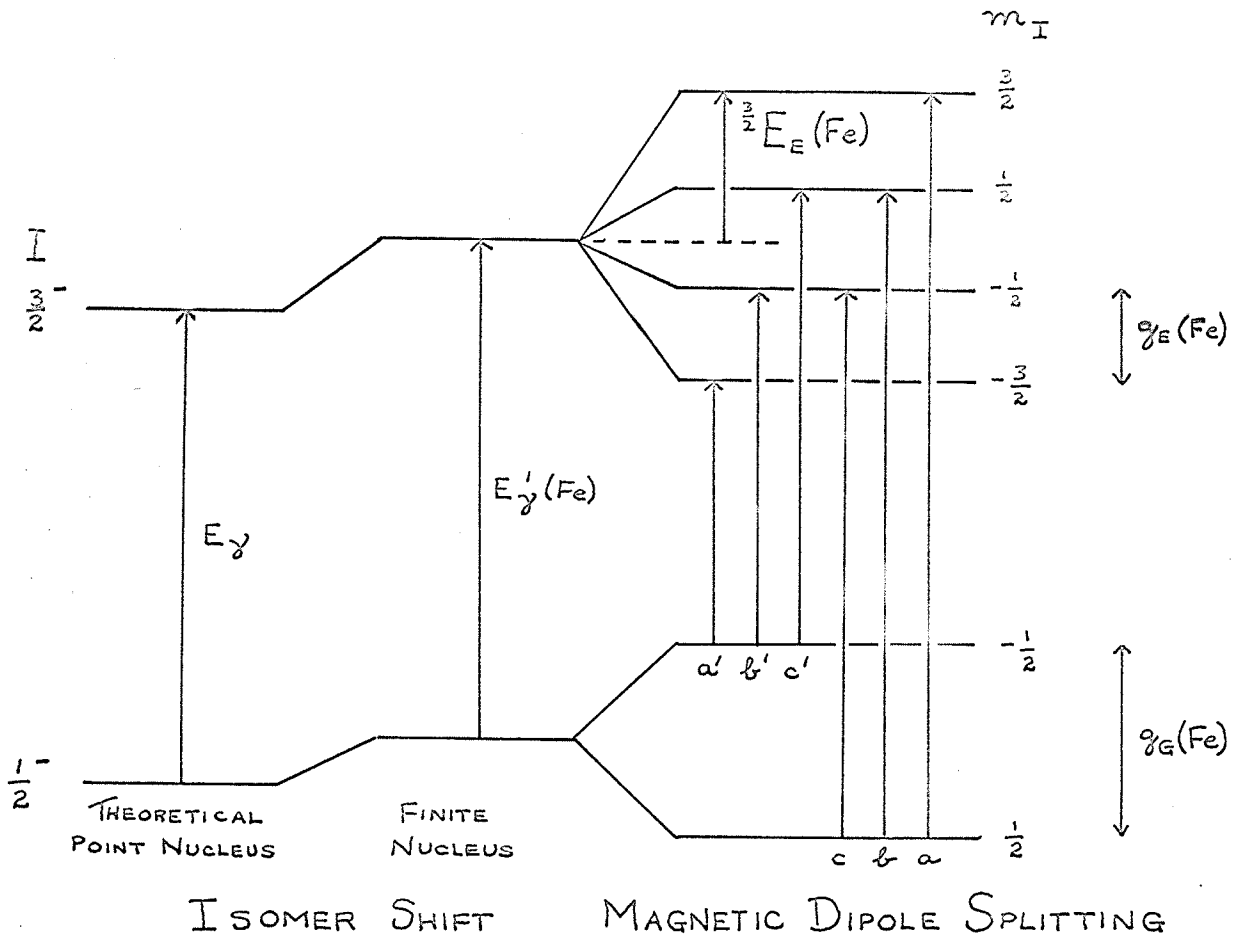


(b) Isomer shift.

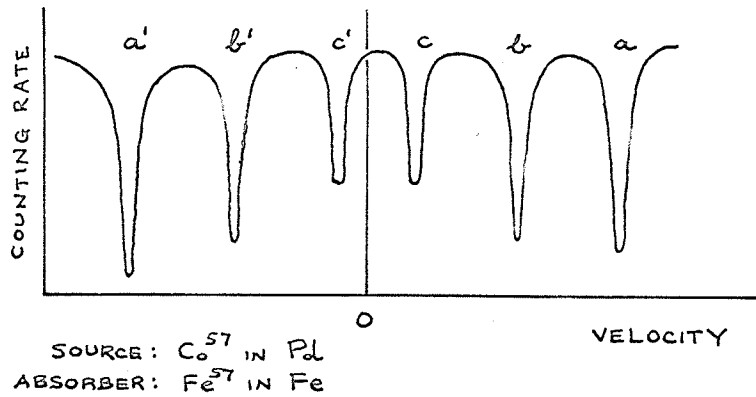


(c) Absorption spectra. Velocity is taken to be positive when the source is moving towards the absorber.

Fig. 3-8. Properties of Fe^{57} bound in unmagnetized iron



(a) Energy levels diagram.



(b) Absorption spectrum.

This spectrum is given by (Wertheim 1964 p. 72):

$$E_X^{m_{I_X}}(\text{Fe}) = -\mu_{nX} H_n(\text{Fe}) m_{I_X} / I_X \quad (3-94.1)$$

$$g_X(\text{Fe}) = \mu_{nX} H_n(\text{Fe}) / I_X \quad (3-94.2)$$

where

X \equiv G (ground state), E (excited state)

μ_{nX} \equiv nuclear magnetic moment in the X state

$H_n(\text{Fe})$ \equiv magnetic field at the iron nucleus in Fe

I_X \equiv nuclear spin of iron in the X state ($I_G = \frac{1}{2}$, $I_E = \frac{3}{2}$)

m_{I_X} \equiv nuclear magnetic quantum number for the state with spin I_X ($m_{\frac{1}{2}} = \frac{1}{2}, -\frac{1}{2}$; $m_{\frac{3}{2}} = \frac{3}{2}, \frac{1}{2}, -\frac{1}{2}, -\frac{3}{2}$)

$E_X^{m_{I_X}}(\text{Fe})$ \equiv energy level in the X state corresponding to m_{I_X} for Fe

$g_X(\text{Fe})$ \equiv splitting in the X state for Fe.

The peaks are:

m 3/2 \rightarrow m 1/2

$$3/2 \rightarrow 1/2 \quad a(\text{Fe}) = E_{\frac{1}{2}}(\text{Fe}) + \frac{3}{2} E_E(\text{Fe}) - \frac{1}{2} E_G(\text{Fe}) + s_I(\text{Fe}, \text{Pd}) \quad (3-95.1)$$

$$1/2 \rightarrow 1/2 \quad b(\text{Fe}) = E_{\frac{1}{2}}(\text{Fe}) + \frac{1}{2} E_E(\text{Fe}) - \frac{1}{2} E_G(\text{Fe}) + s_I(\text{Fe}, \text{Pd}) \quad (3-95.2)$$

$$-1/2 \rightarrow 1/2 \quad c(\text{Fe}) = E_{\frac{1}{2}}(\text{Fe}) + \frac{-1}{2} E_E(\text{Fe}) - \frac{1}{2} E_G(\text{Fe}) + s_I(\text{Fe}, \text{Pd}) \quad (3-95.3)$$

$$1/2 \rightarrow -1/2 \quad c'(\text{Fe}) = E_{\frac{1}{2}}(\text{Fe}) + \frac{1}{2} E_E(\text{Fe}) - \frac{-1}{2} E_G(\text{Fe}) + s_I(\text{Fe}, \text{Pd}) \quad (3-95.4)$$

$$-1/2 \rightarrow -1/2 \quad b'(\text{Fe}) = E_{\frac{1}{2}}(\text{Fe}) + \frac{-1}{2} E_E(\text{Fe}) - \frac{-1}{2} E_G(\text{Fe}) + s_I(\text{Fe}, \text{Pd}) \quad (3-95.5)$$

$$-3/2 \rightarrow -1/2 \quad a'(\text{Fe}) = E_{\frac{1}{2}}(\text{Fe}) + \frac{-3}{2} E_E(\text{Fe}) - \frac{-1}{2} E_G(\text{Fe}) + s_I(\text{Fe}, \text{Pd}) \quad (3-95.6)$$

where $E_{\frac{1}{2}}(\text{Fe}) \equiv$ transition energy for the unsplit case

$s_I(\text{Fe}, \text{Pd}) \equiv \delta$ for the case e = Pd, a = Fe

and the other quantities remain as previously defined.

The peak relative intensities are (Wertheim 1964 p. 75):

	Δm	total	angular dependence
a, a'	-1, +1	3	$9/4 (1 + \cos^2 \theta)$
b, b'	0, 0	2	$3 \sin^2 \theta$
c, c'	+1, -1	1	$3/4 (1 + \cos^2 \theta)$

where θ is the angle between the direction of the magnetic field in Fe and the direction of the emission of the gamma ray.

The splittings are

$$g_G(\text{Fe}) = \mu_{nG} H_n(\text{Fe}) / I_G \quad (3-96.1)$$

$$g_E(\text{Fe}) = \mu_{nE} H_n(\text{Fe}) / I_E \quad (3-96.2)$$

3-3.3: Fe⁵⁷ in α -Fe₂O₃. For Fe⁵⁷ bound in α -Fe₂O₃, the energy level diagram and absorption spectrum are shown in Fig. 3-9.

This spectrum is given by (Wertheim 1964 p. 82):

$$I_G = 1/2-$$

$$m_{IG} E_G(\alpha) = -\mu_{nG} H_n(\alpha) m_{IG} / I_G \quad (3-97.1)$$

$$g_G(\alpha) = \mu_{nG} H_n(\alpha) / I_G \quad (3-97.2)$$

$$I_E = 3/2-$$

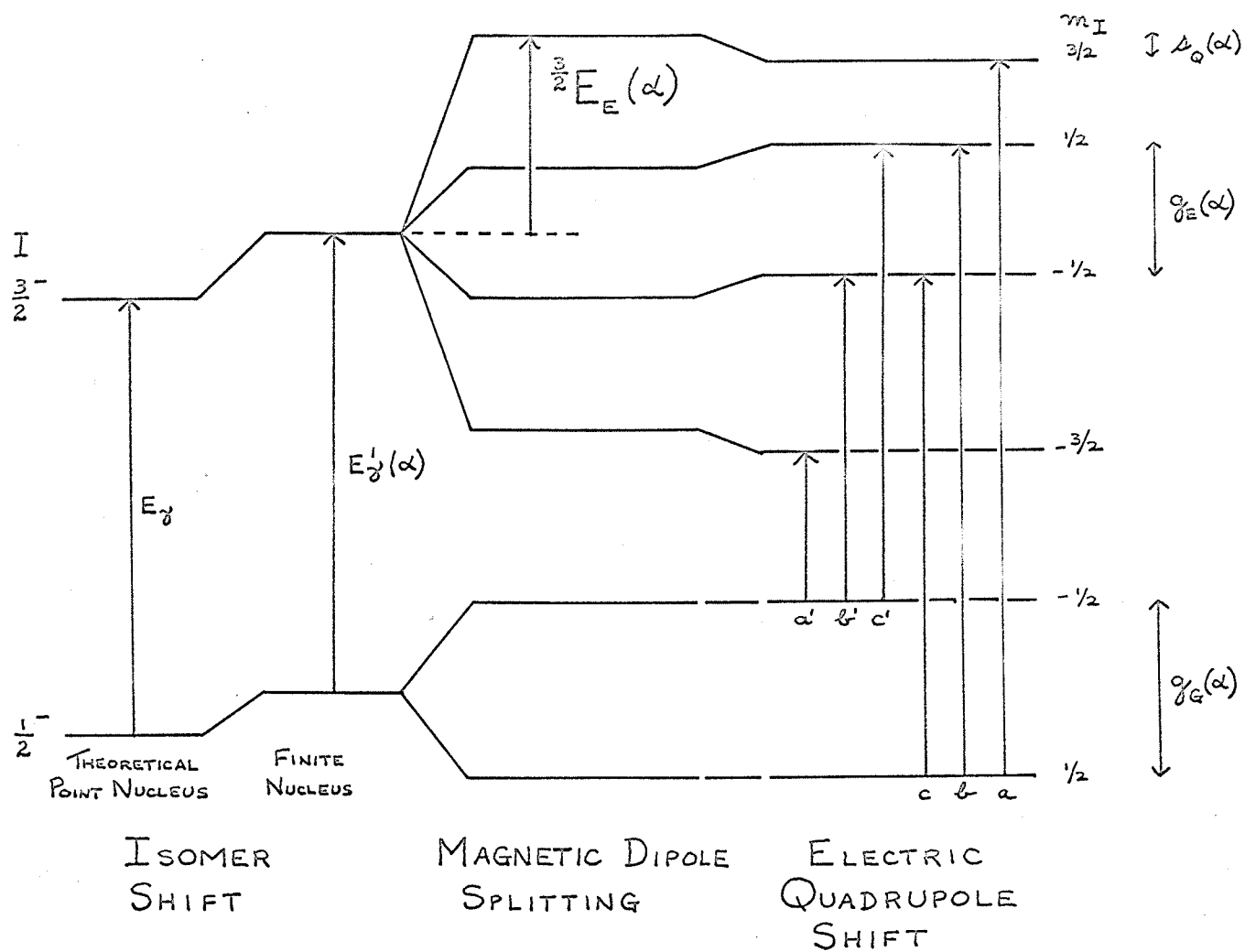
$$m_{IE} E_E(\alpha) = -\mu_{nE} H_n(\alpha) m_{IE} / I_E + (-1)^{|m_{IE}| + \frac{1}{2}} \frac{e^2 q(\alpha) Q \cdot 3 \cos^2 \theta(\alpha) - 1}{4} \quad (3-97.3)$$

for $e^2 q(\alpha) Q \ll \mu_{nE} H_n(\alpha)$

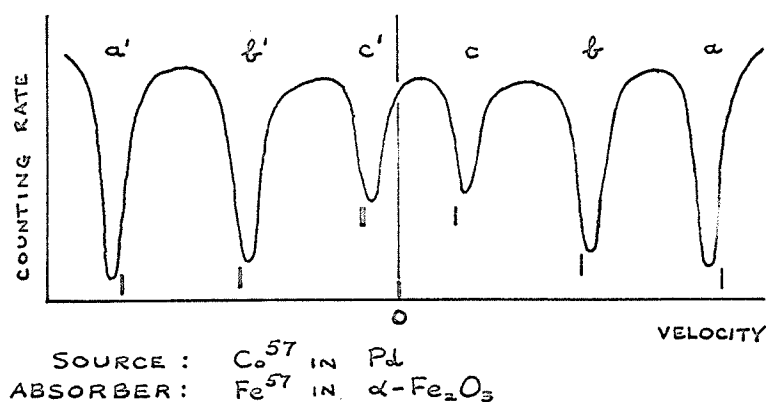
$$g_E(\alpha) = \mu_{nE} H_n(\alpha) / I_E \quad (3-97.4)$$

where $s_Q(\alpha) \equiv \frac{e^2 q(\alpha) Q}{4} \cdot \frac{3 \cos^2 \theta(\alpha) - 1}{2}$, the quadrupole shift

$e q(\alpha) \equiv$ z-component of axially symmetric electric field

Fig. 3-9. Properties of Fe^{57} bound in $\alpha\text{-Fe}_2\text{O}_3$ 

(a) Energy levels diagram.

(b) Absorption spectrum. The small vertical lines indicate the peak positions if $s_Q(\alpha) = 0$.

gradient tensor in α -Fe₂O₃ with symmetry axis at angle $\theta(\alpha)$ with respect to the magnetic axis,

$eQ \equiv$ nuclear electric quadrupole moment,

and the other quantities are similar to those defined for Fe.

For α -Fe₂O₃, $eq(\alpha)$ lies along the principal [111] axis of the crystal, and since the magnetic moments lie in the (111) plane at room temperature, $\theta(\alpha) = 90^\circ$.

The peaks are:

m 3/2 \rightarrow m 1/2

$$3/2 \rightarrow 1/2 \quad a(\alpha) = E_{\frac{1}{2}}'(\alpha) + \frac{3}{2}E_E(\alpha) - \frac{1}{2}E_G(\alpha) + s_I(\alpha, Pd) + s_Q(\alpha) \quad (3-98.1)$$

$$1/2 \rightarrow 1/2 \quad b(\alpha) = E_{\frac{1}{2}}'(\alpha) + \frac{1}{2}E_E(\alpha) - \frac{1}{2}E_G(\alpha) + s_I(\alpha, Pd) - s_Q(\alpha) \quad (3-98.2)$$

$$-1/2 \rightarrow 1/2 \quad c(\alpha) = E_{\frac{1}{2}}'(\alpha) - \frac{1}{2}E_E(\alpha) - \frac{1}{2}E_G(\alpha) + s_I(\alpha, Pd) - s_Q(\alpha) \quad (3-98.3)$$

$$1/2 \rightarrow -1/2 \quad c'(\alpha) = E_{\frac{1}{2}}'(\alpha) + \frac{1}{2}E_E(\alpha) - \frac{1}{2}E_G(\alpha) + s_I(\alpha, Pd) - s_Q(\alpha) \quad (3-98.4)$$

$$-1/2 \rightarrow -1/2 \quad b'(\alpha) = E_{\frac{1}{2}}'(\alpha) - \frac{1}{2}E_E(\alpha) - \frac{1}{2}E_G(\alpha) + s_I(\alpha, Pd) - s_Q(\alpha) \quad (3-98.5)$$

$$-3/2 \rightarrow -1/2 \quad a'(\alpha) = E_{\frac{1}{2}}'(\alpha) - \frac{3}{2}E_E(\alpha) - \frac{1}{2}E_G(\alpha) + s_I(\alpha, Pd) + s_Q(\alpha) \quad (3-98.6)$$

The peak intensities are identical in form to those given above for Fe.

3-3.4: Fe-57 in γ -Fe₂O₃. The spectrum of Fe⁵⁷ bound in γ -Fe₂O₃ consists of a superposition of two spectra, one for the A-sites and the other for the B-sites. Each one of these two spectra is similar in form to an α -Fe₂O₃ spectrum. That is, the energy level diagram, equations, and peak intensities given previously for an α -Fe₂O₃ spectrum, are also applicable in this case; by replacing α with γ A and γ B to represent the A- and B-site spectra respectively, we obtain the energy level diagrams and equations specifying the γ -Fe₂O₃ spectrum.

The energy level diagram and absorption spectrum are shown in Fig. 3-10.

The A-site spectrum is given by:

$$I_G = 1/2-$$

$${}^{mI_G}E_G(\gamma A) = -\mu_{nG} \text{Hn}(\gamma A) m_{I_G} / I_G \quad (3-99.1)$$

$$g_G(\gamma A) = \mu_{nG} \text{Hn}(\gamma A) / I_G \quad (3-99.2)$$

$$I_E = 3/2 -$$

$${}^{mI_E}E_E(\gamma A) = -\mu_{nE} \text{Hn}(\gamma A) m_{I_E} / I_E + (-1)^{|m_{I_E}|} + \frac{1}{2} \frac{e^{2q(\gamma A)Q}}{4} \cdot \frac{3 \cos^2 \theta(\gamma A) - 1}{2} \quad (3-99.3)$$

for $e^{2q(\gamma A)Q} \ll \mu_{nE} \text{Hn}(\gamma A)$

$$g_E(\gamma A) = \mu_{nE} \text{Hn}(\gamma A) / I_E \quad (3-99.4)$$

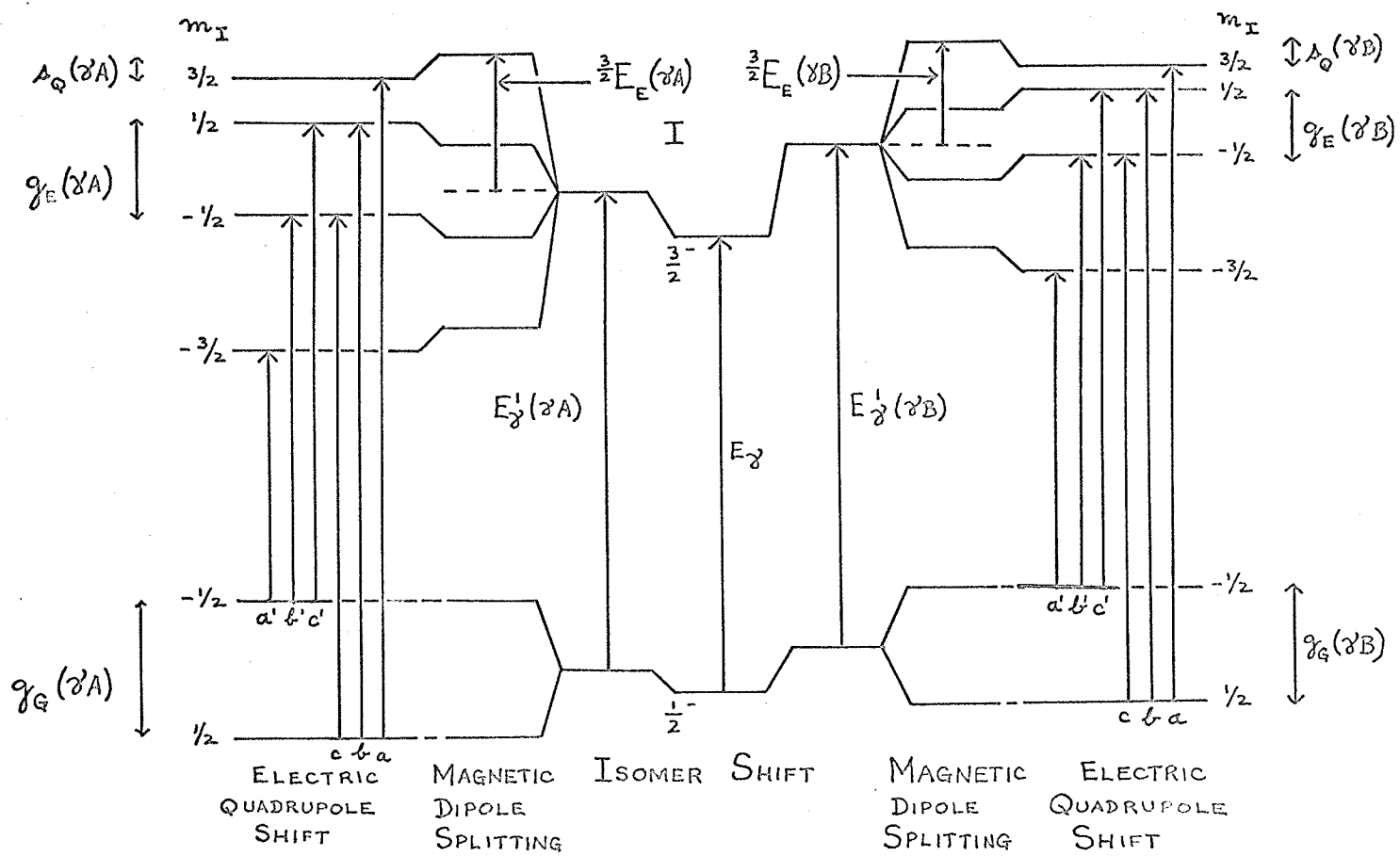
The B-site spectrum is given by:

$$I_G = 1/2-$$

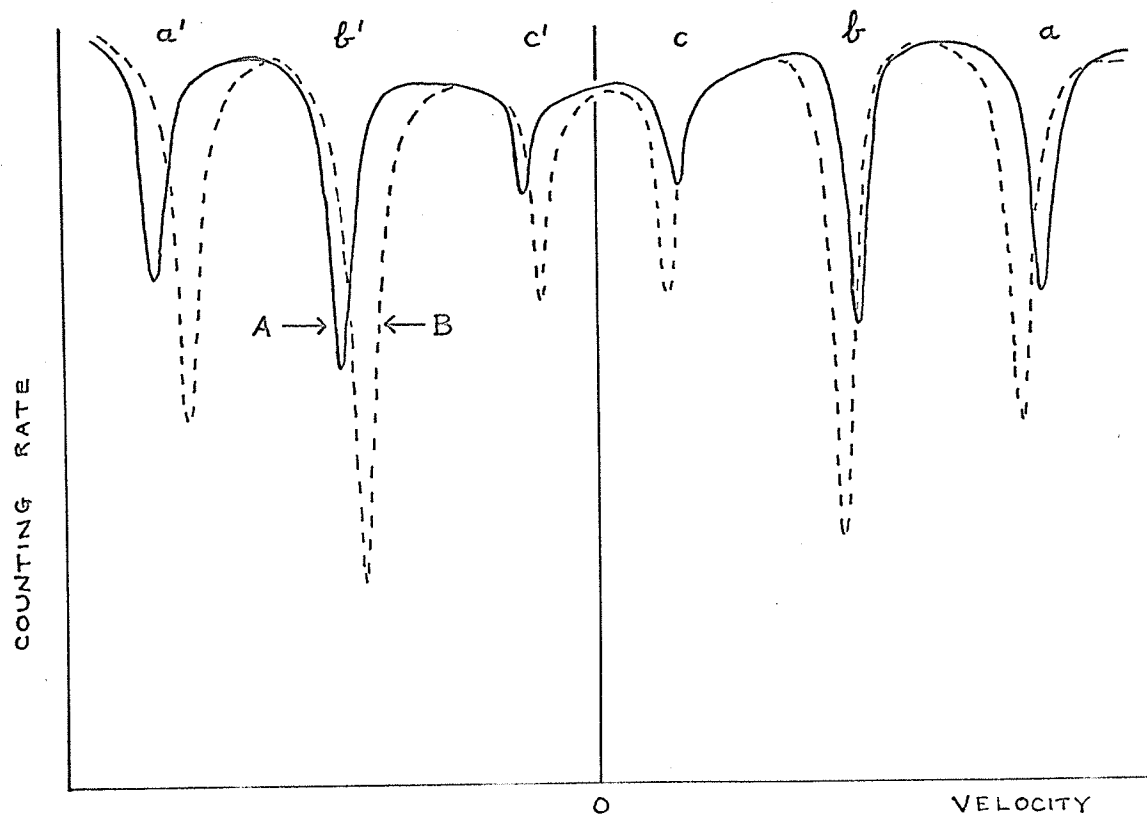
$${}^{mI_G}E_G(\gamma B) = -\mu_{nG} \text{Hn}(\gamma B) m_{I_G} / I_G \quad (3-99.5)$$

$$g_G(\gamma B) = \mu_{nG} \text{Hn}(\gamma B) / I_G \quad (3-99.6)$$

Fig. 3-10. Properties of ^{57}Fe bound in $\gamma\text{-Fe}_2\text{O}_3$



(a) Energy levels diagram.



SOURCE : Co^{57} IN Pd
 ABSORBER : Fe^{57} IN $\gamma\text{-Fe}_2\text{O}_3$

(b) Absorption spectrum. The A and B spectra were further separated by application of a 17kOe magnetic field so they could be resolved.

$$I_E = 3/2 -$$

$$m_{I_E}^{I_E}(\gamma B) = -\mu n_E \text{Hn}(\gamma B) m_{I_E} / I_E + (-1)^{|m_{I_E}|} + \frac{1}{2} \frac{e^2 q(\gamma B) Q}{4} \cdot \frac{3 \cos^2 \theta(\gamma B) - 1}{2}$$

(3-99.7)

for $e^2 q(\gamma B) Q \ll \mu n_E \text{Hn}(\gamma B)$

$$g_E(\gamma B) = \mu n_E \text{Hn}(\gamma B) / I_E \quad (3-99.8)$$

The peaks of the A-site spectrum are:

$$\begin{array}{l} m \ 3/2 \longrightarrow m \ 1/2 \\ 3/2 \longrightarrow 1/2 \quad a(\gamma A) = E'_{\gamma}(\gamma A) + 3/2 E_E(\gamma A) - 1/2 E_G(\gamma A) + s_I(\gamma A, Pd) + s_Q(\gamma A) \\ 1/2 \longrightarrow 1/2 \quad b(\gamma A) = E'_{\gamma}(\gamma A) + 1/2 E_E(\gamma A) - 1/2 E_G(\gamma A) + s_I(\gamma A, Pd) - s_Q(\gamma A) \\ -1/2 \longrightarrow 1/2 \quad c(\gamma A) = E'_{\gamma}(\gamma A) + 1/2 E_E(\gamma A) - 1/2 E_G(\gamma A) + s_I(\gamma A, Pd) - s_Q(\gamma A) \\ 1/2 \longrightarrow -1/2 \quad c'(\gamma A) = E'_{\gamma}(\gamma A) + 1/2 E_E(\gamma A) - 1/2 E_G(\gamma A) + s_I(\gamma A, Pd) - s_Q(\gamma A) \\ -1/2 \longrightarrow -1/2 \quad b'(\gamma A) = E'_{\gamma}(\gamma A) + 1/2 E_E(\gamma A) - 1/2 E_G(\gamma A) + s_I(\gamma A, Pd) - s_Q(\gamma A) \\ -3/2 \longrightarrow -1/2 \quad a'(\gamma A) = E'_{\gamma}(\gamma A) + 3/2 E_E(\gamma A) - 1/2 E_G(\gamma A) + s_I(\gamma A, Pd) + s_Q(\gamma A) \end{array}$$

(3-100.1) to (3-100.6)

The peaks of the B-site spectrum are:

$$\begin{array}{l} m \ 3/2 \longrightarrow m \ 1/2 \\ 3/2 \longrightarrow 1/2 \quad a(\gamma B) = E'_{\gamma}(\gamma B) + 3/2 E_E(\gamma B) - 1/2 E_G(\gamma B) + s_I(\gamma B, Pd) + s_Q(\gamma B) \\ 1/2 \longrightarrow 1/2 \quad b(\gamma B) = E'_{\gamma}(\gamma B) + 1/2 E_E(\gamma B) - 1/2 E_G(\gamma B) + s_I(\gamma B, Pd) - s_Q(\gamma B) \\ -1/2 \longrightarrow 1/2 \quad c(\gamma B) = E'_{\gamma}(\gamma B) + 1/2 E_E(\gamma B) - 1/2 E_G(\gamma B) + s_I(\gamma B, Pd) - s_Q(\gamma B) \\ 1/2 \longrightarrow -1/2 \quad c'(\gamma B) = E'_{\gamma}(\gamma B) + 1/2 E_E(\gamma B) - 1/2 E_G(\gamma B) + s_I(\gamma B, Pd) - s_Q(\gamma B) \\ -1/2 \longrightarrow -1/2 \quad b'(\gamma B) = E'_{\gamma}(\gamma B) + 1/2 E_E(\gamma B) - 1/2 E_G(\gamma B) + s_I(\gamma B, Pd) - s_Q(\gamma B) \\ -3/2 \longrightarrow -1/2 \quad a'(\gamma B) = E'_{\gamma}(\gamma B) + 3/2 E_E(\gamma B) - 1/2 E_G(\gamma B) + s_I(\gamma B, Pd) + s_Q(\gamma B) \end{array}$$

(3-100.7) to (3-100.12)

The peak intensities for both A and B sites are identical to those given for Fe.

IV. EXPERIMENTAL TECHNIQUES

4-1: THE ELRON MÖSSBAUER EFFECT RADIATION ANALYZER

4-1.1: Description of apparatus. The Mössbauer spectra were obtained by means of a Mössbauer Effect Radiation Analyzer and auxiliary processing equipment manufactured by Elron Electronics Industries Ltd., of Haifa, Israel (Figs. 4-1 and 4-2).

The Mössbauer Effect Radiation Analyzer provides automatic analog or digital recording of the spectrum (Lipkin et al. 1964).

The analyzer consists of:

- | | |
|--------------------------------|------------------|
| 1. Linear Velocity Transducer | (Model MVT-1) |
| 2. Transducer Driving Unit | (Model MD -1) |
| 3. Electronic Scalar | (Model NIS-13-S) |
| 4. Digital-to-Analog Converter | (Model MDA-13-S) |
| 5. Electronic Counter | (Model NIC-16) |
| 6. Power Control Unit | |

These units require 115 v. 60 ~.

In addition to the analyzer, the following auxiliary radiation detection equipment is used:

- | | |
|---|-------------------|
| 1. Proportional Counter (sealed gas-filled 90% A-10% CH ₄
manufactured by Twentieth Century Electronics Co.
Ltd. | (Model PX 130f/A) |
| 2. Preamplifier | (Model PCP-1) |
| 3. Active Integrator | (Model CA-26B) |

Fig. 4-1. Experimental Apparatus

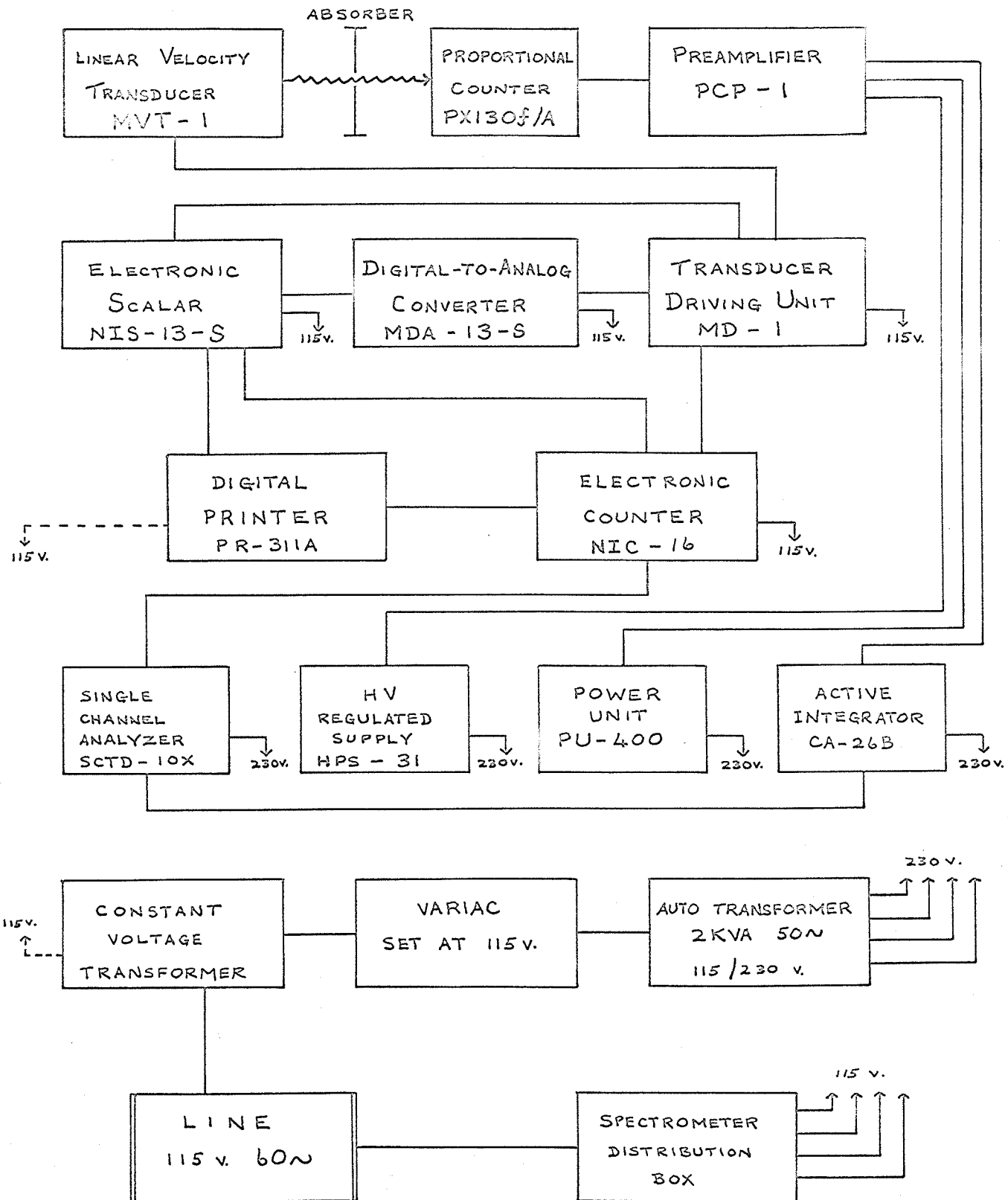


Fig. 4-2. Experimental Setup

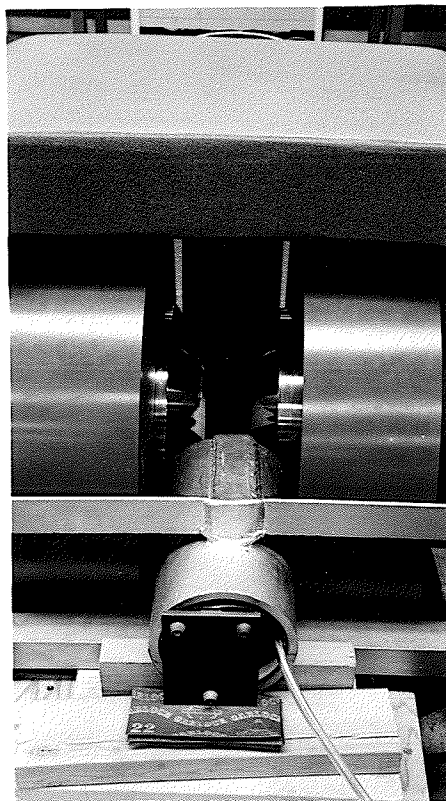
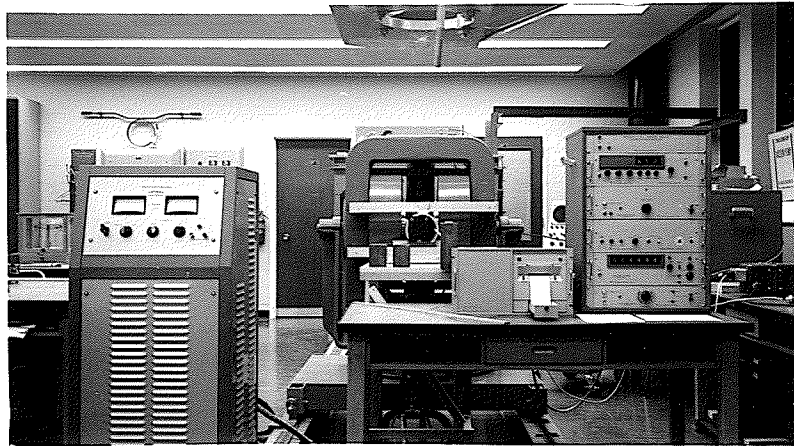
Left to right:

Electromagnet Power Supply
Electromagnet
Digital Printer
Spectrometer

Shielded Transducer

between

Electromagnet Pole Tips



4. Power Unit (Model PV-400)
5. HV Regulated Supply (Model HPS-31)
6. Single Channel Analyzer (Model SCTD-10X)

These units require 230v. 60 \sim .

The output data were recorded in digital form on printed tape with an Elron Digital Printer (Model PR-311A), which requires 115v. 60 \sim .

4-1.2: Theory of Operation. The central component of the analyzer is the Linear Velocity Transducer. It has two coils: a driving coil and a pickup coil, and a moving platform on which the source is mounted. The source should weigh less than 10 grams.

The pickup coil produces a voltage proportional to the velocity of the moving platform. This pickup voltage is compared with a reference voltage, and when the two voltages are not equal, an error voltage results. This error voltage is fed into a high-gain amplifier, which energizes the driving coil to nullify the error. Thus the velocity of the resulting motion is proportional to the reference voltage. The stroke and direction of the moving platform are governed by contacts which limit the stroke to 5 mm maximum and reverse the direction of movement at the end of the stroke.

Velocity is uncalibrated; it is determined with a known emitter and absorber Mössbauer spectrum once the system is set up.

The pertinent specifications of the Mössbauer Effect Radiation Analyzer Motion Control System are:

Movement: Linear-Sawtooth or Parabolic Displacement

Velocity Range: Variable - ranges 1) -10, +10 mm/sec
(constant velocity, sawtooth displacement)

2) -50, +50 mm/sec (constant acceleration,
parabolic displacement)

Length of Stroke: Variable - 2 → 6 mm

Maximum Velocity: Can be set internally to 5, 10, 20, 50 mm/sec
approximately, or externally to any desired setting
up to 50 mm/sec.

Velocity Resolution: 0.2% of maximum velocity setting

Velocity Accuracy: Constant to within ± 0.02 mm/sec $\pm 0.5\%$
maximum during each stroke and during one hour.
Average velocity drift ± 0.05 mm/sec
maximum during 24 hr. at ambient temperature constant
to within $\pm 5^\circ\text{C}$.

Operating Temperature Range: 0 → 50°C.

While the time dependence of the velocity-determining reference voltage (and therefore of the velocity itself) can be arbitrarily chosen if so desired, two particular choices are of interest. In the first mode of operation, the velocity-determining reference voltage is constant with respect to time; thus the displacement is a linear function of time: the sawtooth mode. In the second mode of operation, the velocity-determining reference voltage is directly proportional to time; thus the displacement is a quadratic function of time: the parabolic mode. The total time necessary to obtain a spectrum is approximately the same for both modes. The advantages and disadvantages of each mode are discussed below.

A proportional counter sealed with 70 cm. of the gas mixture

90% argon - 10% methane is used as a radiation detector. Its output pulses are fed into the Active Integrator CA-26B, where they are amplified and integrated, and thence to the single-channel analyzer SCTD-10X where the 14.4 keV peak is selected.

Sawtooth Mode

In the sawtooth mode of operation, the velocity-determining reference voltage is obtained from the Digital-to-Analog Converter MDA-13-S, which is driven by Scalar NIS-13S. Since the scalar has 3 decimal digits, a resolution of up to 1/1000 can be selected, equivalent to a 1000-channel multichannel analyzer. To change from one velocity to the next, a Proceeding Command is given to the NIS-13-S scalar by the central timer included in the Counter NIC-16. The output pulses of the single-channel analyzer are counted by the Counter NIC-16. However, during the reverse motion (flyback) of the moving part of the Linear Velocity Transducer, the counter and its time base are inhibited, so that counts are collected during the predetermined net time of constant velocity periods only. The flyback velocity is of the order of 10 cm/sec. The counting time controlled by the built-in timer is selectable in steps of 0.1, 0.3, 1, ..., 1000 sec.

To obtain a graphical record of transmission versus velocity, the X input of an X-Y recorder is driven by the velocity reference voltage output of MDA-13-S, while the Y input is connected to the counter NIC-16 via a Digital-to-Analog converter (DA-13). For recording the output data in digital form, a digital printer is connected to the scalar (NIS-13-S) to record the velocity channel

number, and to the counter (NIC-16) to record the corresponding transmission.

Parabolic Mode

In the parabolic mode of operation, an external audio oscillator and a modulator are required. The oscillator drives the scalar (NIS-13-S) which causes parabolic motion of the transducer. Standard pulses from a single channel analyzer are applied to a modulator, which modulates the pulse heights according to the instantaneous velocity of the transducer. The amplitude-modulated pulses are then applied to a multichannel analyzer.

Comparison of Sawtooth Mode and Parabolic Mode

The parabolic mode does not require a flyback time like the sawtooth mode does; consequently, the time needed to record a spectrum is somewhat less for the parabolic mode than for the sawtooth mode. Since in the parabolic mode the transducer sweeps through all the velocities of the spectrum each cycle, a rough (that is, poor statistics) idea of what the spectrum looks like can be obtained very quickly. In addition, slow spectrum drifts due to factors beyond the control of the experimenter can be minimized by using the parabolic mode: for example, if the counting rate slowly changed due to a slow drift in pulse height, the reference line of the spectrum remains horizontal in the parabolic mode, but becomes sloped in the sawtooth mode. However, the sawtooth mode is useful for examining parts of the spectrum without having to spend the time required to obtain the

whole spectrum, which would be necessary in an unmodified parabolic mode. The audio oscillator could undoubtedly be modified to yield the required output, but that would be a project in itself. In order to scan the required portion of the spectrum in the same time which the sawtooth mode would take, the time scale would have to be expanded, and this is not a simple thing to do with the precision necessary in this experiment. With stable equipment, however, the sawtooth mode yields satisfactory data. A rough idea of what a spectrum is like is readily and quickly obtained with the sawtooth mode using a resolution of 100 channels and a low counting time.

In the sawtooth mode, the velocity is variable within the range $-10, +10$ mm/sec constant velocity, sawtooth displacement. In the parabolic mode, the velocity is variable within the range $-50, +50$ mm/sec constant acceleration, parabolic displacement. Accordingly, for a particular Mössbauer spectrum it may be necessary to choose the parabolic mode over the sawtooth mode, simply because the velocity range of the sawtooth mode is not large enough.

Thus, both modes have their own particular advantages and disadvantages, and it is the aim of the experiment itself which determines which mode to use. In this case, the sawtooth mode was used exclusively since a multichannel analyzer was not available.

4-2: PREPARATION OF SOURCES AND ABSORBERS

The radioactive source used in the experiment was manufactured by New England Nuclear Corp., of Boston, Massachusetts. It was

prepared by electrodeposition of cobalt-57 on to a piece of palladium foil 0.5" in diameter x 0.001" thick, followed by diffusion of the deposited cobalt into the Pd matrix material by annealing for 2 hrs at 900°C in H₂. The active area is a 0.25" diameter spot. The source was 5.5 m c on 2/3/65, 200 mr/hr (γ) contact radiation, and had a specific activity of 6 mc/ μ gmCo.

Two types of absorbers were used: powders and thin slices from aligned single crystals.

The powders were mixed with liquid paraffin which was melted by immersing a beaker of it into hot water, and while cooling were pressed into the shape of discs \sim 2" x 0.5" thick. The discs were rigidly mounted between the source and detector to minimize vibrations. Thin crystal slices in the (111) plane were required; accordingly, it was necessary to align the crystal before cutting a slice from it. The orientation was performed by X-ray diffraction. α -Fe₂O₃ is an extremely hard, brittle rhombohedral crystal which crystallizes with (110) faces; this latter fact simplified the alignment procedure considerably. The crystal selected to be cut was first glued (110) - face down to a specially constructed heavy-duty goniometer. The glue used was Hugh Courtwright Quartz Cement #70. To affix the crystal to the goniometer, the movable part of the goniometer fixture is removed and heated to \sim 200°C on a hot plate until the small quantity of Quartz Cement on it melts; then the crystal is placed in the cement on the goniometer and both are allowed to cool to room temperature. The resulting bond is very strong and holds the crystal firmly during

slicing. The crystal can be removed from the mount by heating, and any cement remaining on the crystal can be dissolved (although slowly) in acetone.

When the crystal is attached to the goniometer, the goniometer is placed on a fixture to which is also attached a Unicam X-Ray back reflection camera for von Laue (Kittel 1963 p. 56) photographs. The crystal is 30 mm from the film. This fixture is then placed on an X-ray machine and a Laue photograph of the (110) plane is taken. The crystals were irradiated by Mo X-rays, 20 ma at 45kV for ~ 15 minutes. It is developed using the standard processing method for X-ray film. This photograph serves to verify that the (110) plane has been obtained; small adjustments in orientation can now be made with the aid of a Greninger chart to ensure that the [110] direction is parallel to the x-ray beam. Next, the (110) plane is rotated about the [110] axis through an angle (determined from the (110) Laue photograph) so that the intersection of the (110) and (111) planes is a horizontal straight line **normal** to the X-ray beam. Since the angle between the (110) and (111) planes is 57° , the crystal is then rotated either up or down 57° ; the [111] direction is now parallel to the X-ray beam. At this point a second Laue photograph is taken, and any needed orientation adjustments are made; these are usually caused by the fact that the crystal is not mounted at the intersection of the axes of rotation, resulting in slightly off-center patterns after a rotation.

The goniometer is now removed from the X-ray fixture, and the crystal is cut in the (111) plane with a Micro-Matic Precision

Wafering Machine Model WMSA manufactured by Micromech Mfg. Corp., of Union, New Jersey. This first slice removed is rather thick, in order to produce a large flat (111) surface on the crystal. The crystal is then removed from the goniometer and glued (111) -face-down to a small flat ceramic tile, and another cut is made so that the large chunk of crystal falls away from the thin (0.010") slice, which remains glued to the tile. The thin slice is removed by dissolving the glue in acetone. In this way, thin slices can also be made from the first thick slice. This method is more likely to yield unbroken small slices than the alternate method of sawing a thin slice off the end of a crystal, due to the presence of blade flutter, vibrations, slightly irregular table feed, etc.

The thin slices thus produced were oriented in the (111) plane within a degree. They were mounted, mosaic-style, on sheets of lucite, utilizing vacuum grease as the adhesive.

4-3: EXPERIMENTAL DIFFICULTIES ENCOUNTERED AND OVERCOME

The Elron Mössbauer Effect Radiation Analyzer performed adequately from the beginning. However, some difficulties were encountered with the auxiliary apparatus used for radiation detection, and also with the pointer.

The proportional counter originally supplied with the system was a gas flow-thru type. It was manufactured by 20th Century as a sealed counter with 70 cm. of the gas mixture 90%A-10% CH₄ in it and

sold to Elron. These counters have a finite useful lifetime because of eventual unavoidable air contamination and decomposition of the CH_4 (Wilkinson 1950 p. 149ff), so when this counter became unusable, Elron converted it to a flow-thru counter by drilling entrance and exit holes at opposite ends of the tube and inserting plastic nipples to connect up with tubing from the gas supply.

The gas mixture was supplied by a large cylinder of compressed gas. The cylinder pressure was lowered by two reducing valves in series to a pressure just slightly above atmospheric pressure. The gas was then passed through the tube and into a large beaker of transparent motor oil. The flow rate was observed by noting the size, formation rate, and speed of the bubbles; it was adjusted until just enough gas was flowing through to prevent any air from entering the tube.

Upon investigation, it was determined that while the peak position in the pulse-height vs. channel no. spectrum was relatively insensitive to flow rate, it was exceedingly sensitive to small pressure changes. (+10 mm Hg change in pressure produced a -10% change in pulse energy and therefore peak position. This effect confirmed the predictions of Rossi and Staub (1949 p. 72ff).) Since the exit tube was vented directly to the atmosphere, small changes in atmospheric pressure were transmitted directly to the tube, resulting in the peak shifting out of the window in the single channel analyzer and producing a marked decrease in the counting rate. To circumvent this, the window in the single channel analyzer could have been

broadened or the single channel analyzer operated in the integral counting mode, but this would have increased the background tremendously and decreased the resolution. The counter was filled and then sealed, but it still behaved erratically. Accordingly, the flow counter was returned to Elron and a replacement sealed counter (20th Century 90% A + 10% CH₄) was sent. This counter has given satisfactory service. Thus it is apparent that when a proportional counter is used as a detector for this type of experiment, it must be of the sealed type.

The Elron auxiliary radiation detection equipment requires a 230v. 60~ supply. The small 115/230 v. auto transformer included with the equipment proved inadequate, so a larger one was substituted. In order to minimize the effect of line voltage changes on the pulse height, a constant voltage transformer and a Variac (set at 115 v.) were inserted in series between the 115 v. 60~ line and the auto transformer.

The Elron Active Integrator was found to contain numerous cold-soldered connexions, and even when these were repaired it still reacted unfavorably when subjected to the vibrations of the Elron Printer which was mounted in the same cabinet. Thus the Printer was removed from the cabinet and isolated from the Integrator: the Integrator now functions adequately. The Elron HV Regulated Supply gave trouble until the potentiometer was cleaned. It now functions satisfactorily.

The Elron Printer had some loose connections and poorly soldered joints too, but it did not stop repetitive printing until

the 50 ~ pinion was replaced by a 60 ~ one. The machine does run off 115V. though, unlike the rest of the Elron auxiliary apparatus. The Printer is supplied with 115V. through the constant voltage transformer, and runs satisfactorily. It is physically **isolated** from the rest of the apparatus in order that the vibrations which it produces while printing will not affect the other equipment.

The quality of performance of the total Mössbauer system (Mössbauer Effect Radiation Analyzer, Radiation Detection Equipment, and Printer) is such that it can now be left running continuously for days without need for constant attention on the part of the experimenters.

V. EXPERIMENTAL RESULTS AND DISCUSSION

The experimental procedure can be divided into two parts: the determination of the magnetic field at the iron nucleus for the different A and B lattice sites in γ -Fe₂O₃ ($H_N(\gamma A)$ and $H_N(\gamma B)$ respectively) by applying an external magnetic field to separate the A and B Mössbauer spectra; and the determination of the time rate of change as a function of temperature for the conversion of γ -Fe₂O₃ to α -Fe₂O₃. The results were obtained from γ -Fe₂O₃ Mössbauer spectra calibrated by α -Fe₂O₃ Mössbauer spectra.

5-1: MAGNETIC FIELD DETERMINATION

5-1.1: Data Analysis Procedures. The A-site and B-site

γ -Fe₂O₃ spectra were separated by computer techniques. Each pair (one A, one B) of overlapping peaks was analyzed individually, the separation being performed by the least squares approximation method of fitting a curve of Lorentzian form to each A and B peak. The program employs the variable metric minimization method for line shape fitting; it determines, numerically, local minima of differentiable functions of N variables. In the process of locating each minimum, a matrix which characterizes the behavior of the function about the minimum is determined. For a region in which the function depends quadratically on the variables, no more than N iterations are

required. By a suitable choice of starting values and without modification of the procedure, linear constraints can be imposed upon the variables (Davidon 1959).

The α -Fe₂O₃ spectra which were used for calibration were analyzed manually. First, the channel number of each peak position was determined by inspection. Next, the spectral parameters were calculated by hand in units of channels. Finally, the α -Fe₂O₃ spectra themselves were calibrated; this involved the comparison of our results with previously published data in order to determine the velocity/channel calibration scale. The maximum possible error involved in these calculations was determined simultaneously. Details of the particular method of analysis employed to calibrate α -Fe₂O₃ spectra are outlined in what follows.

The six peaks of the α -Fe₂O₃ spectrum may be written:

$$\begin{bmatrix} a(\alpha) \\ b(\alpha) \\ c(\alpha) \\ c'(\alpha) \\ b'(\alpha) \\ a'(\alpha) \end{bmatrix} = \begin{bmatrix} 1 & 3/2 & 1/2 & 1 \\ 1 & 1/2 & 1/2 & -1 \\ 1 & -1/2 & 1/2 & -1 \\ 1 & 1/2 & -1/2 & -1 \\ 1 & -1/2 & -1/2 & -1 \\ 1 & -3/2 & -1/2 & 1 \end{bmatrix} \begin{bmatrix} k + s_I(\alpha) \\ g_E(\alpha) \\ g_G(\alpha) \\ s_Q(\alpha) \end{bmatrix} \quad (5-1)$$

where $k = E_{\gamma}^i(\alpha)$, and all other symbols are as previously defined.

By defining

$$S(\alpha) \equiv \begin{bmatrix} a(\alpha) \\ b(\alpha) \\ c(\alpha) \\ c'(\alpha) \\ b'(\alpha) \\ a'(\alpha) \end{bmatrix}, \quad K(\alpha) \equiv \begin{bmatrix} 1 & 3/2 & 1/2 & 1 \\ 1 & 1/2 & 1/2 & -1 \\ 1 & -1/2 & 1/2 & -1 \\ 1 & 1/2 & -1/2 & -1 \\ 1 & -1/2 & -1/2 & -1 \\ 1 & -3/2 & -1/2 & 1 \end{bmatrix}, \quad P(\alpha) \equiv \begin{bmatrix} k + s_I(\alpha) \\ g_E(\alpha) \\ g_G(\alpha) \\ s_Q(\alpha) \end{bmatrix} \quad (5-2.1) \quad (5-2.2) \quad (5-2.3)$$

$$\text{we can write } S(\alpha) = K(\alpha) P(\alpha). \quad (5-3)$$

It is desirable to use all 6 lines in the calculation of each spectral parameter, rather than 4 or less (which it is always possible to do), since the results obtained in this manner should be more physically reliable than a determination using less than the full spectrum of 6 lines, even though this procedure tends to increase the maximum possible error in each parameter.

Expressing each spectral parameter as a linear combination of the 6 lines, we have:

$$\begin{bmatrix} k + s_I(\alpha) \\ g_E(\alpha) \\ g_G(\alpha) \\ s_Q(\alpha) \end{bmatrix} = \begin{bmatrix} A_1 & B_1 & C_1 & C'_1 & B'_1 & A'_1 \\ A_2 & B_2 & C_2 & C'_2 & B'_2 & A'_2 \\ A_3 & B_3 & C_3 & C'_3 & B'_3 & A'_3 \\ A_4 & B_4 & C_4 & C'_4 & B'_4 & A'_4 \end{bmatrix} \begin{bmatrix} a(\alpha) \\ b(\alpha) \\ c(\alpha) \\ c'(\alpha) \\ b'(\alpha) \\ a'(\alpha) \end{bmatrix} \quad (5-4.1)$$

$$\text{and by defining } A(\alpha) \equiv \begin{bmatrix} A_1 & B_1 & C_1 & C'_1 & B'_1 & A'_1 \\ A_2 & B_2 & C_2 & C'_2 & B'_2 & A'_2 \\ A_3 & B_3 & C_3 & C'_3 & B'_3 & A'_3 \\ A_4 & B_4 & C_4 & C'_4 & B'_4 & A'_4 \end{bmatrix}$$

where all the elements of $A(\alpha)$ are constants to be determined (5-4.2)

$$\text{we can write } P(\alpha) = A(\alpha) S(\alpha) \quad (5-4.3)$$

Substituting equation (5-3) into equation (5-4.3) yields $A(\alpha) K(\alpha) = 1$ (5-5) which represents 16 equations with 24 unknowns. These equations are solved to yield A_i, B_i, B'_i, A'_i in terms of C_i, C'_i ($i = 1, 2, 3, 4$), and $A(\alpha)$ becomes

$$B(\alpha) \equiv \begin{bmatrix} 1/4 + 1/2C_1 - 1/2C'_1 & 1/4 - 3/2C_1 + 1/2C'_1 & C_1 \\ 1/2 + 1/2C_2 - 1/2C'_2 & -1/2 - 3/2C_2 + 1/2C'_2 & C_2 \\ -1/2 + 1/2C_3 - 1/2C'_3 & 3/2 - 3/2C_3 + 1/2C'_3 & C_3 \\ 1/4 + 1/2C_4 - 1/2C'_4 & -1/4 - 3/2C_4 + 1/2C'_4 & C_4 \end{bmatrix}$$

$$\begin{bmatrix} C'_1 & 1/4 + 1/2C_1 - 3/2C'_1 & 1/4 - 1/2C_1 + 1/2C'_1 \\ C'_2 & 1/2 + 1/2C_2 - 3/2C'_2 & -1/2 - 1/2C_2 + 1/2C'_2 \\ C'_3 & -3/2 + 1/2C_3 - 3/2C'_3 & 1/2 - 1/2C_3 + 1/2C'_3 \\ C'_4 & -1/4 + 1/2C_4 - 3/2C'_4 & 1/4 - 1/2C_4 + 1/2C'_4 \end{bmatrix}$$

(5-6).

Since the values of C_i, C'_i ($i = 1, 2, 3, 4$) are arbitrary, they can be chosen to weight any 2 lines as desired. However, in the absence of any specific requirement that one or two particular lines be given certain weights significantly larger or smaller than the weights

assigned the other lines by reason of their being more or less accurate than the others, it is preferable to assign, to all peaks, weights that are as nearly equal as possible, or at least equal to within an order of magnitude. The particular values chosen for C_i, C'_i affect the size of the maximum possible error. Since there is no straightforward way to mathematically determine values of C_i, C'_i which minimize the maximum possible error, suitable values were chosen by inspection; $B(\alpha)$ becomes

$$C(\alpha) \equiv \begin{bmatrix} 1/4 & 1/2 & -1/4 & -1/4 & 1/2 & 1/4 \\ 3/8 & 3/8 & -3/4 & -1/2 & 7/8 & -3/8 \\ 1/2 & -1/2 & 1 & -1 & 1/2 & -1/2 \\ 1/4 & -1/2 & 1/4 & 1/4 & -1/2 & 1/4 \end{bmatrix} \quad (5-7.1)$$

$$\text{with } \begin{bmatrix} C_1 & C'_1 \\ C_2 & C'_2 \\ C_3 & C'_3 \\ C_4 & C'_4 \end{bmatrix} = \begin{bmatrix} -1/4 & -1/4 \\ -3/4 & -1/2 \\ 1 & -1 \\ 1/4 & 1/4 \end{bmatrix} \quad (5-7.2)$$

$$\text{Thus } \begin{bmatrix} k + s_I(\alpha) \\ g_E(\alpha) \\ g_G(\alpha) \\ s_Q(\alpha) \end{bmatrix} = \begin{bmatrix} 1/4 & 1/2 & -1/4 & -1/4 & 1/2 & 1/4 \\ 3/8 & 3/8 & -3/4 & -1/2 & 7/8 & -3/8 \\ 1/2 & -1/2 & 1 & -1 & 1/2 & -1/2 \\ 1/4 & -1/2 & 1/4 & 1/4 & -1/2 & 1/4 \end{bmatrix} \begin{bmatrix} a(\alpha) \\ b(\alpha) \\ c(\alpha) \\ c'(\alpha) \\ b'(\alpha) \\ a'(\alpha) \end{bmatrix} \quad (5-8.1)$$

or $P(\alpha) = C(\alpha) S(\alpha)$ (5-8.2)

Assuming $\Delta a = \Delta b = \Delta c = \Delta c' = \Delta b' = \Delta a' \equiv \Delta \nu$,

$$\Delta P(\alpha) \equiv \begin{bmatrix} \Delta(k + s_I(\alpha)) \\ \Delta g_E(\alpha) \\ \Delta g_G(\alpha) \\ \Delta s_Q(\alpha) \end{bmatrix} = \begin{bmatrix} 2 \\ 3\frac{1}{4} \\ 4 \\ 2 \end{bmatrix} \Delta \nu \quad (5-9).$$

If the peak position errors are not all equal, $\Delta P(\alpha)$ can be found by evaluating $\Delta P(\alpha) = C(\alpha) \Delta S(\alpha)$. (5-10)

In this manner $P(\alpha)$ and $\Delta P(\alpha)$ are determined.

For an α -Fe₂O₃ calibration spectrum, the maximum possible error in the zero velocity k (channel 500) is ± 0.5 channel, and the (maximum possible) error in determining each peak position is ± 0.5 channel. The errors in the parameters are thus

$$\begin{bmatrix} \Delta(k + s_I(\alpha)) \\ \Delta g_E(\alpha) \\ \Delta g_G(\alpha) \\ \Delta s_Q(\alpha) \end{bmatrix} = \begin{bmatrix} 2 \\ 3\frac{1}{4} \\ 4 \\ 2 \end{bmatrix} (\pm \frac{1}{2} \text{ch}) = \pm \begin{bmatrix} 1 \\ 1.6 \\ 2 \\ 1 \end{bmatrix} \text{ch.} \quad \text{with } \Delta k = \pm 0.5 \text{ ch.} \quad (5-11)$$

and $\Delta E(\alpha) = \Delta(3g_E(\alpha) + g_G(\alpha)) = 4.8 + 2 = 6.8$ channel. (5-12)

When the α -Fe₂O₃ spectral parameters had been obtained for a particular spectrum, it was calibrated using the following procedure.

$$\mu_{nG} = 0.09024 \text{ nm} \quad (\text{Muir et al. 1965 p. 20})$$

$$\mu_{nE} = -0.154 \text{ nm} \quad (\text{Muir et al. 1965 p. 20})$$

$$\mu_n = 5.0505 \times 10^{-24} \text{ erg/0e} \quad (\text{Morrish 1965 p. 649})$$

$$H_n(\alpha) = 515 \text{ kOe} \quad (\text{Kistner and Sunyar 1960})$$

$$I_G = 1/2 \quad (\text{Garif'ianov et al. 1957})$$

$$I_E = I_G + 1 = 3/2$$

$$|g_{nG}(\alpha)| = |\mu_{nG}| H_n(\alpha)/I_G = 4.694 \times 10^{-19} \text{ erg}$$

$$|g_{nE}(\alpha)| = |\mu_{nE}| H_n(\alpha)/I_E = 2.670 \times 10^{-19} \text{ erg}$$

The total length of the spectrum from $a'(\alpha)$ to $a(\alpha)$ is

$$E(\alpha) = a(\alpha) - a'(\alpha) = 3g_E(\alpha) - g_G(\alpha) = 1.271 \times 10^{-18} \text{ erg}.$$

Converting this to cm/sec by using

$$c = 2.998 \times 10^{10} \text{ cm/sec} \quad (\text{Morrish 1965 p. 649})$$

$$1\text{eV} = 1.602 \times 10^{-12} \text{ erg} \quad (\text{Morrish 1965 p. 649})$$

$$E_\gamma = 14.39 \text{ keV} \quad (\text{Muir et al. 1965 p. 20})$$

we obtain $V(\alpha) = c \frac{E(\alpha)}{E_\gamma} = 1.652 \text{ cm/sec}$. Equating this to the value

of $E(\alpha)$ found from the parameters expressed in channels, the

calibration scale is determined. To estimate the error in $V(\alpha)$,

published accurate values for the spectral parameters are used

(Kistner and Sunyar 1960):

$$s_I(\alpha, SS) = 0.047 \pm 0.003 \text{ cm/sec}$$

$$g_E(\alpha) = 0.345 \pm 0.003 \text{ cm/sec}$$

$$g_G(\alpha) = 0.611 \pm 0.005 \text{ cm/sec}$$

$$s_Q(\alpha) = 0.012 \pm 0.003 \text{ cm/sec}$$

from which $\frac{\Delta V(\alpha)}{V(\alpha)} = 0.85\%$

5-1.2: Results and Discussion. Determination of the magnetic fields $H_n(\gamma A)$ and $H_n(\gamma B)$ at the iron nuclei for the different A and B lattice sites in γ -Fe₂O₃.

The γ -Fe₂O₃ sample, which consisted of a powder of spherical particles with less than 1% α -Fe₂O₃ present as an impurity, was held rigidly in a matrix of paraffin, inserted between the pole pieces of an electromagnet, and subjected to an applied magnetic field of $17,400 \pm 300$ gauss. The resulting Mössbauer spectrum (see Fig. 5-1) was analyzed by computer, and the following results were obtained:

a(γA)	$\Delta a(\gamma A)$	a(γB)	$\Delta a(\gamma B)$
b(γA)	$\Delta b(\gamma A)$	b(γB)	$\Delta b(\gamma B)$
c(γA)	$\Delta c(\gamma A)$	c(γB)	$\Delta c(\gamma B)$
c'(γA)	$\Delta c'(\gamma A)$	c'(γB)	$\Delta c'(\gamma B)$
b'(γA)	$\Delta b'(\gamma A)$	b'(γB)	$\Delta b'(\gamma B)$
a'(γA)	$\Delta a'(\gamma A)$	a'(γB)	$\Delta a'(\gamma B)$

912.0	0.9	893.6	0.5	in units of channels.
741.7	0.5	730.6	0.4	
579.0	3.5	569.0	1.5	
436.0	1.0	451.0	0.7	
267.4	0.8	289.0	0.5	
96.6	0.8	127.3	0.5	

These results were determined in two steps. First, the γ spectra were separated under the constraint that the full-widths at

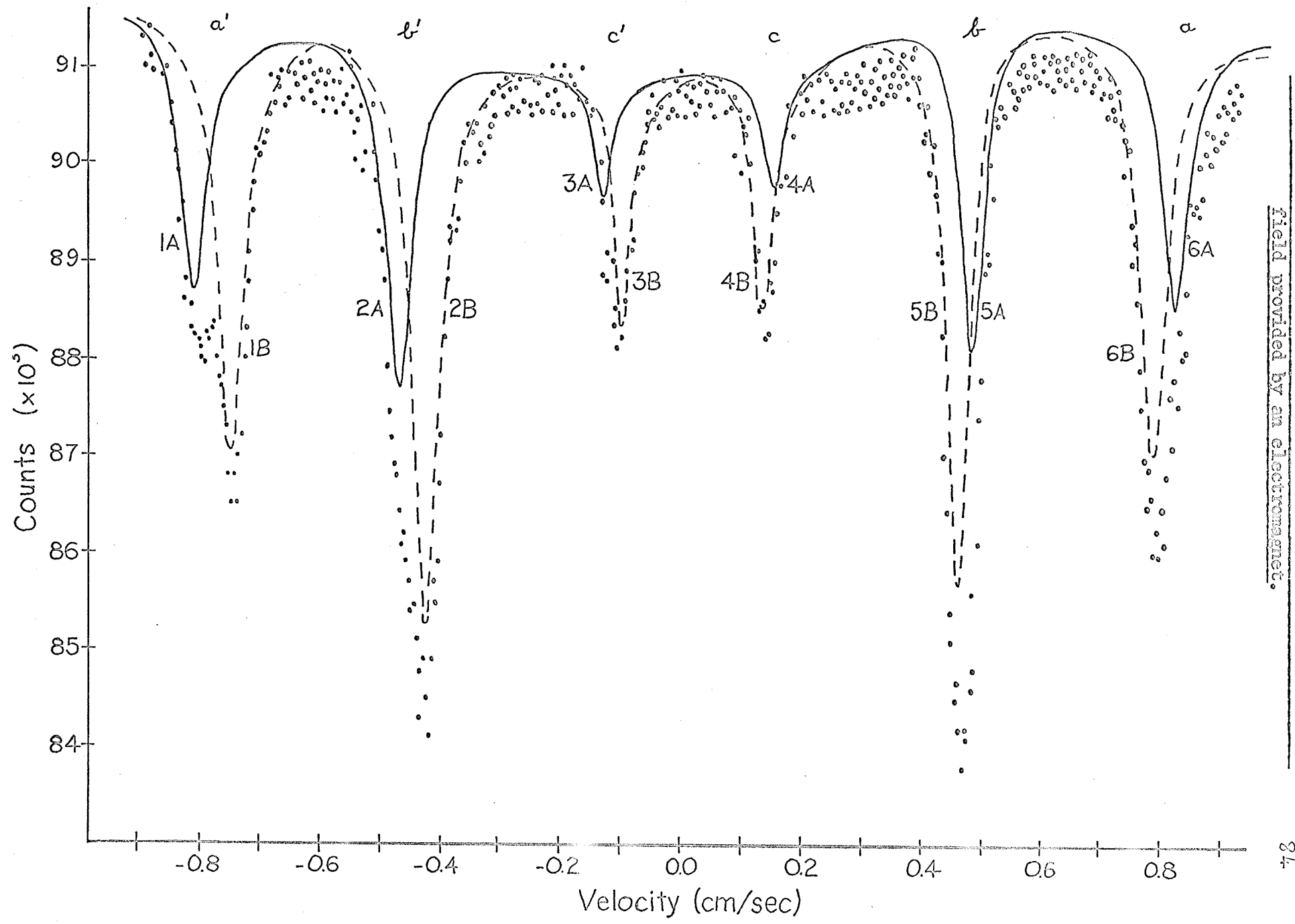


Fig. 5-1. Mössbauer spectrum of γ -Fe₂O₃ in a 1710e magnetic field provided by an electromagnet.

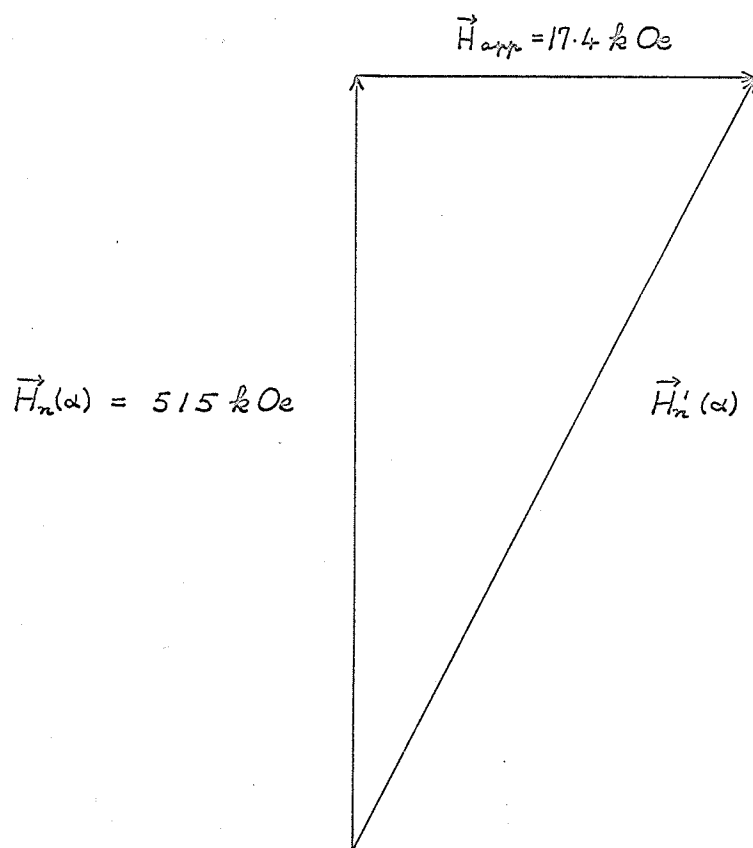
half height of corresponding peaks be identical. This produced well-resolved a' and b' peaks with small errors but poorly resolved a and b peaks with large errors. Accordingly, the additional constraint that the intensities of a-a' and b-b' peaks be identical was imposed, and this produced well-resolved peaks with smaller errors. Unfortunately the c-c' peaks remain poorly resolved with large errors.

The velocity transducer was shielded from the applied magnetic field by being placed inside a steel pipe. This changed the transducer velocity scale (cm/sec/ch) since the transducer is an electromechanical device and the steel pipe affected the flux path of the permanent magnets inside the transducer. Hence it was necessary to run an α -Fe₂O₃ spectrum with the transducer shielded inside the pipe in order to obtain an α -Fe₂O₃ spectrum for calibration purposes. The steel pipe was successful in shielding the transducer from the magnetic field of the electromagnet; the change in the transducer velocity scale caused by the applied magnetic field was of negligible proportions.

When the α -Fe₂O₃ spectrum was analyzed preparatory to its being used to calibrate the γ -Fe₂O₃ spectrum, the calculations neglected to take into account the fact that the applied magnetic field changed the effective magnetic field at the nucleus. That this procedure is correct can be justified as follows (see Fig. 5-2): The Dzialoshinsky moment \vec{M}_D (Morrish 1965 p. 480) lines up with the applied magnetic field \vec{H}_{app} . Since \vec{M}_D is nearly perpendicular to $\vec{H}_n(\alpha)$, the resultant field \vec{H}' is approximately given by

$$H_n'(\alpha)^2 \doteq H_n(\alpha)^2 + H_{app}^2. \quad (5-13.1)$$

Fig. 5-2. The change in the effective magnetic field at the nucleus caused by an applied magnetic field.



$$\text{Thus } \frac{H_n'(\alpha)}{H_n(\alpha)} \doteq \sqrt{1 + \left(\frac{H_{\text{app}}}{H_n(\alpha)}\right)^2} \quad (5-13.2)$$

and since $H_{\text{app}} \ll H_n(\alpha)$

$$\frac{H_n'(\alpha)}{H_n(\alpha)} \doteq 1 + 1/2 \left(\frac{H_{\text{app}}}{H_n(\alpha)}\right)^2 \quad (5-13.3).$$

$$\text{Evaluating yields } \frac{H_n'(\alpha)}{H_n(\alpha)} \doteq 1 + 1/2 \left(\frac{17.4 \text{ kOe}}{515 \text{ kOe}}\right)^2 = 1 + \frac{0.53}{1000} .$$

Hence the effect upon the line positions of the α - Fe_2O_3 spectrum is a shift of $\approx 1/2$ -channel, which is negligible under present circumstances. An additional effect is the broadening of each line by ≈ 1 channel; but as linewidths are not of interest in the calibration spectrum, this effect can also be overlooked.

To the first order, the quadrupole shifts $s_Q(\gamma A)$ and $s_Q(\gamma B)$ vanish upon application of a large enough magnetic field. This may be shown in the following manner.

The saturation magnetization of γ - Fe_2O_3 is 11,150 Oe (Brown and Johnson 1962). Thus for $H_{\text{app}} = 17,400$ Oe, all the magnetic dipoles in the polycrystalline powdered sample of γ - Fe_2O_3 are aligned with \vec{H}_{app} . Since the individual γ particles each consist of many randomly oriented tightly bound crystals, the application of \vec{H}_{app} will not change the orientation of the crystals with respect to \vec{H}_{app} (Boyle and Hall 1962). Hence, the angle between the magnetic axis and the symmetry axis of the electric field gradient tensor in each small crystal varies in a random fashion from crystal to crystal. When the quadrupole shift is averaged over the whole sample by

integrating over the surface of a sphere, it vanishes. However, the quadrupole interaction does produce a broadening of the peaks. Thus if it is desired to measure the quadrupole shift, it should be done with $H_{\text{app}} = 0$. However, this is difficult to accomplish since the $H_{\text{app}} = 0$ spectrum is unresolved.

The γ - Fe_2O_3 spectral parameters which were required to determine the magnetic fields were determined as follows:

$$g_E(\gamma A)1 = a(\gamma A) - b(\gamma A) \quad (\text{from eqn. (5-6)}).$$

$$g_E(\gamma A)2 = b'(\gamma A) - a'(\gamma A)$$

$$\text{thus } g_E(\gamma A) = 1/2 (g_E(\gamma A)1 + g_E(\gamma A)2)$$

$$\Delta g_E(\gamma A)1 = |g_E(\gamma A)1 - g_E(\gamma A)|$$

$$\Delta g_E(\gamma A)2 = |g_E(\gamma A)2 - g_E(\gamma A)|$$

$$\text{thus } \Delta g_E(\gamma A) = 1/2 (\Delta g_E(\gamma A)1 + \Delta g_E(\gamma A)2)$$

Similarly for $g_E(\gamma B) \pm \Delta g_E(\gamma B)$.

$$s_I(\gamma A, \text{Pd})1 = 1/2(a(\gamma A) + a'(\gamma A)) - k \quad (\text{from eqn. (5-6)}).$$

$$s_I(\gamma A, \text{Pd})2 = 1/2(b(\gamma A) + b'(\gamma A)) - k$$

$$\text{thus } s_I(\gamma A, \text{Pd}) = 1/2(s_I(\gamma A, \text{Pd})1 + s_I(\gamma A, \text{Pd})2)$$

$$\Delta s_I(\gamma A, \text{Pd})1 = |s_I(\gamma A, \text{Pd})1 - s_I(\gamma A, \text{Pd})|$$

$$\Delta s_I(\gamma A, \text{Pd})2 = |s_I(\gamma A, \text{Pd})2 - s_I(\gamma A, \text{Pd})|$$

$$\text{thus } \Delta s_I(\gamma A, \text{Pd}) = 1/2 (\Delta s_I(\gamma A, \text{Pd})1 + \Delta s_I(\gamma A, \text{Pd})2)$$

Similarly for $s_I(\gamma B, \text{Pd}) \pm \Delta s_I(\gamma B, \text{Pd})$.

$$\begin{aligned}
 H_n(\gamma B) &= (H_n(\gamma B) - H_{\text{app}}) + (H_{\text{app}}) \\
 &= \left(\frac{g_E(\gamma B)}{g_E(\alpha)} \times H_n(\alpha) \right) + (H_{\text{app}}) \\
 &= \left(\frac{162.4 \text{ channel}}{173.3 \text{ channel}} \times 515 \text{ kOe} \right) + (17 \text{ kOe}) = 499 \text{ kOe}
 \end{aligned}
 \tag{5-14.2}$$

To estimate the error in the calculations for the magnetic fields, it is necessary to examine the errors inherent in the α -Fe₂O₃ calibration spectrum as well as the errors in the γ -Fe₂O₃ spectrum.

The α -Fe₂O₃ spectrum (see Fig. 5-3) used for calibration is:

$$\begin{array}{l}
 \left[\begin{array}{c} a \\ b \\ c \\ c' \\ b' \\ a' \end{array} \right] = \left[\begin{array}{c} 916.0 \\ 751.5 \\ 579.0 \\ 450.5 \\ 277.0 \\ 93.0 \end{array} \right] ; \left[\begin{array}{c} k + s_I(\alpha, \text{Pd}) \\ g_E(\alpha) \\ g_G(\alpha) \\ s_Q(\alpha) \\ E(\alpha) \end{array} \right] = \left[\begin{array}{c} 509.1 \\ 173.3 \\ 302.8 \\ -4.6 \\ 822.7 \end{array} \right]
 \end{array}$$

in units of channels.

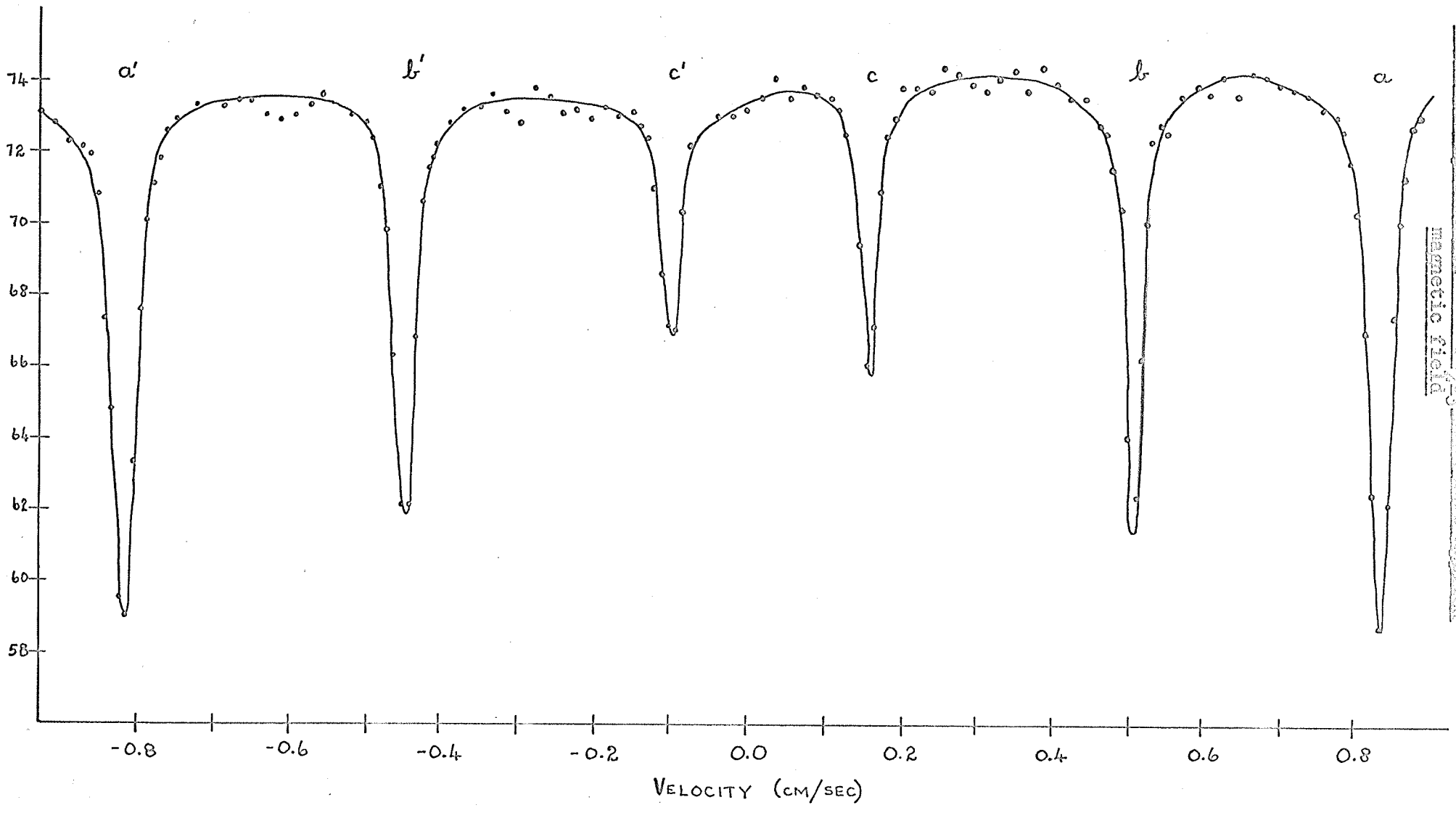
This spectrum was taken with the transducer shielded and the external magnetic field applied to the α -Fe₂O₃ sample. In this case, $k=500$ channel. Since $822.7 \text{ channel} \equiv 1.652 \text{ cm/sec}$, $1 \text{ channel} \equiv 0.00201 \text{ cm/sec}$.

From eqn. (5-14.1), it may be shown that

$$\Delta H_n(\gamma A) = \left(\frac{\Delta g_E(\gamma A)}{g_E(\gamma A)} + \frac{\Delta g_E(\alpha)}{g_E(\alpha)} + \frac{\Delta H_n(\alpha)}{H_n(\alpha)} \right) \left(\frac{g_E(\gamma A)}{g_E(\alpha)} \times H_n(\alpha) \right) + \Delta H_{\text{app}}$$

$$\text{Now } \Delta g_E(\gamma A) = 0.25 \text{ channel}$$

Fig. 5-3. Mössbauer spectrum of α -Fe₂O₃ with zero applied magnetic field



$$\Delta g_E(\alpha) = 1.6 \text{ channel}$$

$$\Delta H_n(\alpha) = 5 \text{ kOe} \quad (\text{Wertheim and Buchanan 1962})$$

$$\Delta H_{\text{app}} = 0.3 \text{ kOe}$$

However, the maximum possible error in $g_E(\alpha)$ is not a good indicator of the upper limit of the uncertainty in this parameter, as it is rather too large: a computer fit of the $\alpha\text{-Fe}_2\text{O}_3$ data would have reduced it. By taking the hyperfine field for $\alpha\text{-Fe}_2\text{O}_3$ to be exact, the error in $H_n(\gamma A)$ is determined to be about 1%, or 5 kOe. A similar result is obtained for $H_n(\gamma B)$.

The isomer shifts and associated errors are found as follows.

The spectrometer was adjusted so that 500 channel \equiv 0 cm/sec. Thus

$$s_I(\gamma A, \text{Pd}) = (k + s_I(\gamma A, \text{Pd})) - k = 504.4 - 500 = 4.4 \text{ channel}$$

$$s_I(\gamma B, \text{Pd}) = (k + s_I(\gamma B, \text{Pd})) - k = 510.1 - 500 = 10.1 \text{ channel}$$

and converting to velocity by multiplying by 0.00201 cm/sec/channel

$$s_I(\gamma A, \text{Pd}) = 0.0089 \text{ cm/sec}$$

$$s_I(\gamma B, \text{Pd}) = 0.020 \text{ cm/sec}$$

It is conventional to express the isomeric shift with respect to stainless steel. Accordingly, a spectrum was taken with 310 stainless steel as absorber, and it was found that $k + s_I(\text{SS}, \text{Pd}) = 484$ channels. This spectrum was taken with the transducer unshielded; consequently, a second $\alpha\text{-Fe}_2\text{O}_3$ spectrum, also taken with the transducer unshielded, was required for calibration:

$$\begin{array}{c} a \\ b \\ c \\ c' \\ b' \\ a' \end{array} = \begin{array}{c} 950 \\ 774 \\ 586 \\ 446 \\ 257.5 \\ 58.5 \end{array} \begin{array}{c} [k + s_I(\alpha, Pd)] \\ g_E(\alpha) \\ g_G(\alpha) \\ s_Q(\alpha) \\ E(\alpha) \end{array} = \begin{array}{c} 509.9 \\ 187.4 \\ 327.5 \\ -5.6 \\ 889.6 \end{array} \quad \text{in units of channels.}$$

Here, $k = 500$ channels.

Since 889.6 channels $\equiv 1.652$ cm/sec, 1 channel $\equiv 0.00186$ cm/sec.

$$\begin{aligned}
 \text{Thus } s_I(SS, Pd) &= (k + s_I(SS, Pd)) - k = 484 - 500 \text{ channels} \\
 &= -16 \text{ channels} \\
 &= -16 \text{ channels} \times 0.00186 \text{ cm/sec/channel} \\
 &= -0.030 \text{ cm/sec}
 \end{aligned}$$

$$\begin{aligned}
 \text{Hence } s_I(\gamma A, SS) &= s_I(\gamma A, Pd) - s_I(SS, Pd) \\
 &= 0.009 + 0.030 \text{ cm/sec} = 0.039 \text{ cm/sec}
 \end{aligned}$$

$$\text{and similarly } s_I(\gamma B, SS) = 0.020 + 0.030 \text{ cm/sec} = 0.050 \text{ cm/sec}$$

The errors in the isomer shift are estimated in the following manner:

$$\begin{aligned}
 \Delta(k + s_I(\gamma A, Pd)) &= 0.65 \text{ channel} \\
 \Delta(k + s_I(\gamma B, Pd)) &= 0.32 \text{ channel} \\
 \Delta k &= 0.5 \text{ channel}
 \end{aligned}$$

$$\therefore \Delta s_I(\gamma A, Pd) = 0.65 + 0.5 = 1.2 \text{ channels} \quad (27\%)$$

$$\Delta s_I(\gamma B, Pd) = 0.32 + 0.5 = 0.82 \text{ channels} \quad (8.1\%)$$

Now $\Delta E(\alpha) = 6.8$ channel; hence, for the first α - Fe_2O_3 calibration

spectrum

$$\frac{\Delta E(\alpha)}{E(\alpha)} = \frac{6.8 \text{ channel}}{822.7 \text{ channel}} = 0.83\%$$

But $\frac{\Delta V(\alpha)}{V(\alpha)} = 0.85\%$

Therefore, the maximum possible calibration error is $0.83 + 0.85\% = 1.7\%$

i.e. 1 channel $\equiv 0.00201 \text{ cm/sec} \pm 1.7\%$

Converting the isomeric shift errors into units of cm/sec,

we have

$$\begin{aligned} \Delta s_I(\gamma A, Pd) &\longrightarrow \left(\frac{\Delta s_I(\gamma A, Pd)}{s_I(\gamma A, Pd)} + 1.7\% \right) s_I(\gamma A, Pd) \\ &= (0.27 + 0.017) \times 4.4 \text{ channel} \times 0.00201 \text{ cm/sec/ch} \\ &= 0.0025 \text{ cm/sec} \quad (28\%) \end{aligned}$$

similarly $\Delta s_I(\gamma B, Pd) = 0.0020 \text{ cm/sec} \quad (10\%)$

In order to determine the errors for the isomeric shifts expressed with respect to stainless steel, it is necessary to examine a second $\alpha\text{-Fe}_2\text{O}_3$ spectrum.

$$\Delta s_I(SS, Pd) = 0.5 \text{ ch} \quad (3.1\%)$$

Since $\Delta E(\alpha)$ remains unchanged,

$$\frac{\Delta E(\alpha)}{E(\alpha)} = \frac{6.8 \text{ channels}}{889.6 \text{ channels}} = 0.76\%$$

Thus the calibration error is $0.76 + 0.85 = 1.6\%$

i.e. 1 channel $\equiv 0.00186 \text{ cm/sec} \pm 1.6\%$

Converting $\Delta s_I(SS, Pd)$ into units of cm/sec, we have

$$\Delta s_I(SS, Pd) \longrightarrow \left(\frac{\Delta s_I(SS, Pd)}{s_I(SS, Pd)} + 1.6\% \right) s_I(SS, Pd)$$

$$\begin{aligned}
 &= (3.1\% + 1.6\%) \times 16 \text{ ch} \times 0.00186 \text{ cm/sec/ch} \\
 &= 0.0014 \text{ cm/sec} \quad (4.7\%)
 \end{aligned}$$

$$\begin{aligned}
 \text{Hence } \Delta s_I(\gamma A, SS) &= \Delta s_I(\gamma A, Pd) + \Delta s_I(SS, Pd) \\
 &= 0.0025 + 0.0014 \text{ cm/sec} \\
 &= 0.0039 \text{ cm/sec} \quad (10\%)
 \end{aligned}$$

$$\text{Similarly } \Delta s_I(\gamma B, SS) = 0.0034 \text{ cm/sec} \quad (6.8\%)$$

The isomeric shift, quadrupole shift, and their corresponding errors as determined from this second α - Fe_2O_3 spectrum are:

$$\begin{aligned}
 (k + s_I(\alpha, Pd)) \pm \Delta(k + s_I(\alpha, Pd)) &= 509.9 \pm 1 \text{ ch} \\
 k \pm \Delta k &= 500 \pm 0.5 \text{ ch}
 \end{aligned}$$

$$\therefore s_I(\alpha, Pd) \pm \Delta s_I(\alpha, Pd) = 9.9 \pm 1.5 \text{ ch} = 9.9 \text{ ch} \pm 15\%$$

Converting to cm/sec:

$$\begin{aligned}
 s_I(\alpha, Pd) \pm \Delta s_I(\alpha, Pd) &= (9.9 \text{ ch} \pm 15\%)(0.00186 \text{ cm/sec/ch} \pm 1.6\%) \\
 &= 0.0184 \text{ cm/sec} \pm 17\% \\
 &= 0.0184 \pm 0.0031 \text{ cm/sec}
 \end{aligned}$$

Relative to stainless steel:

$$\begin{aligned}
 s_I(\alpha, SS) \pm \Delta s_I(\alpha, SS) &= [s_I(\alpha, Pd) \pm \Delta s_I(\alpha, Pd)] - [s_I(SS, Pd) \pm \\
 &\quad \Delta s_I(SS, Pd)] \\
 &= [0.0184 \pm 0.0031] - [-0.0298 \pm 0.0014] \text{ cm/sec} \\
 &= 0.048 \pm 0.005 \text{ cm/sec} = 0.0048 \text{ cm/sec} \pm 11\%
 \end{aligned}$$

$$s_Q(\alpha) \pm \Delta s_Q(\alpha) = -5.6 \pm 1 \text{ ch.} = -5.6 \text{ ch} \pm 18\%$$

$$\begin{aligned}
 \text{Converting to cm/sec:} &= (-5.6 \text{ ch} \pm 18\%)(0.00186 \text{ cm/sec/ch} \pm 1.6\%) \\
 &= -0.0104 \text{ cm/sec} \pm 20\% \\
 &= -0.010 \pm 0.002 \text{ cm/sec}
 \end{aligned}$$

The results are summarized and compared with other published results in the table in Fig. 5-4.

Since $s_I(\gamma A, SS) < s_I(\gamma B, SS)$ and $H_n(\gamma A) < H_n(\gamma B)$, the covalent binding of the tetrahedral site ions is larger than that of the octahedral site ions; since the Fe^{3+} ion - O^{2-} ion distance is less for the A sites than for B sites, this is one result that can be predicted theoretically (Watson and Freeman 1961).

The relative number of Fe^{3+} ions at the A and B sites can be determined by finding the intensity ratio of the two lines of each doublet. The first two doublets have the best resolution, and the intensity ratios are 0.64 ± 0.05 and 0.60 ± 0.05 respectively.

The theoretical intensity ratio is 0.33 for all vacancies in A sites, 0.60 for all vacancies in B sites, and 0.50 for an equal number of vacancies in A and B sites. Hence, this confirms that the vacancies are located in B sites exclusively.

5-2: TEMPERATURE CONVERSION RATE DETERMINATION

Determination of the time rate of change as a function of temperature for the conversion of γ - Fe_2O_3 to α - Fe_2O_3 .

The preparation of the γ - Fe_2O_3 absorbers which were used in this part of the experiment involved a three-stage process:

First, the sample of granulated γ - Fe_2O_3 was crushed into a fine powder;

Second, the sample was placed inside an electric furnace and heated, in air, at a certain temperature for a definite length of

REFERENCE	ABSORBER	APPLIED FIELD (k Oe)	INTERNAL FIELD (k Oe)	ISOMER SHIFT RELATIVE TO STAINLESS STEEL (cm/sec)	QUADRUPOLE SHIFT (cm/sec)
PRESENT WORK	$\alpha\text{-Fe}_2\text{O}_3$	—	515 ± 5	0.048 ± 0.005	-0.010 ± 0.002
PRESENT WORK	$\gamma\text{-Fe}_2\text{O}_3$ A-SITE	17.4	489 ± 5	0.039 ± 0.004	—
		B-SITE	17.4	499 ± 5	0.050 ± 0.003
BAUMINGER ET AL. 1961	$\gamma\text{-Fe}_2\text{O}_3$ A + B SITES	—	505 ± 20	—	—
KELLY ET AL. 1961	$\gamma\text{-Fe}_2\text{O}_3$ A + B SITES	—	496 ± 20	—	—

Fig. 5-4. Summary of results of the magnetic field determination

time, then allowed to cool to room temperature.

Third, the powder was added to melted paraffin, stirred to obtain an even consistency, and the resulting mixture pressed into a mold while cooling to form the completed absorber.

In order to simplify the relative intensity calculations, the thickness of each absorber was adjusted by carefully removing thin layers of material until the transmission of each absorber was approximately the same. The density of the absorbers was $< 0.2 \text{ mgm/cm}^2$.

It was necessary to crush the γ - Fe_2O_3 samples in order to obtain consistent results. The conversion rate is dependent upon the total surface area of the particles in the sample being heated, and the γ - Fe_2O_3 available was a coarse powder composed of particles which varied widely in size, and hence in surface area. Since it was difficult to ensure that the particle distribution be the same for each sample fabricated, samples identical in all other respects yielded different results, even though subjected to the same heating conditions.

Crushing the γ - Fe_2O_3 to a powder of uniformly-sized particles produced consistent and reproducible results.

The background was $16 \pm 0.3\%$ with instrumental noise negligible.

Each Mössbauer spectrum obtained to study the γ - $\text{Fe}_2\text{O}_3 \longrightarrow \alpha$ - Fe_2O_3 conversion process was analyzed manually using the following procedure:

First, a spectrum of pure α - Fe_2O_3 and one of pure unheated

γ -Fe₂O₃ were obtained. The $a'(\alpha)$ peak positions were noted and marked on the a' peak of the conversion spectrum. An estimation of the amount of α -Fe₂O₃ present was made, and the corresponding $a'(\alpha)$ peak was superimposed upon the a' peak of the conversion spectrum (see Fig. 5-5). The $a'(\alpha)$ peak was then subtracted from the a' peak of the conversion spectrum, and the resulting peak was examined to see how closely it approximated the $a'(\gamma)$ peak. This process was repeated until a good $a'(\gamma)$ peak was obtained. Since some peaks in the conversion spectrum were poorly resolved and difficult to analyze, in general not all six peaks were separated for all conversion spectra. The a' peak could always be separated; where more than one peak was analyzed, the reported intensity ratio is the average of the intensity ratios for the peaks that could be analyzed.

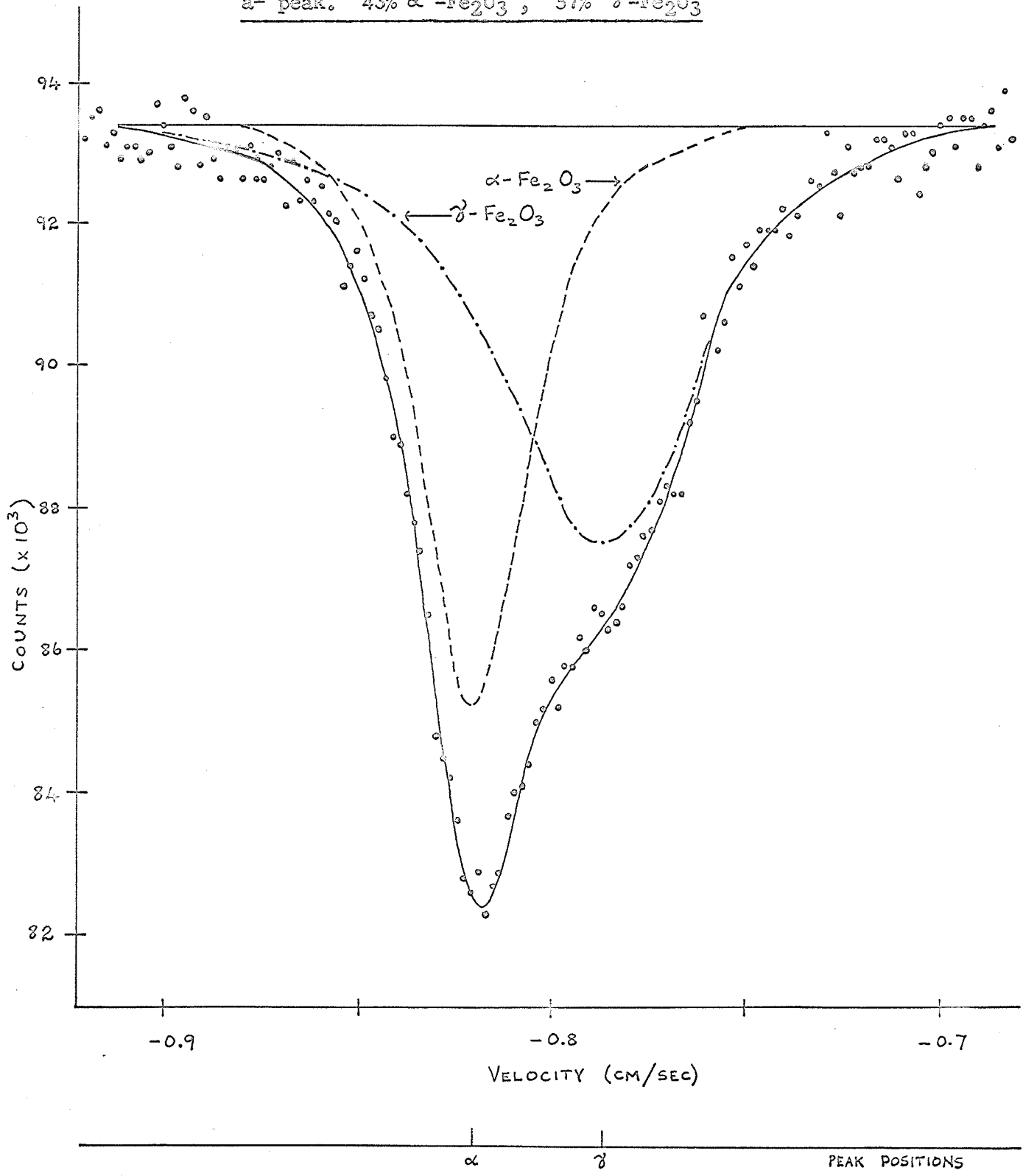
The peak intensities were found by measuring the areas under the curves with a planimeter.

In performing the α - γ separation as outlined above, it was implicitly assumed that both α -Fe₂O₃ and γ -Fe₂O₃ have Debye temperatures which are identical within the limits of accuracy imposed by the intrinsic nature of the separation procedure. The reason for this is, since the intensity depends upon the recoilless fraction which, in turn, is a function of the Debye temperature, if the α -Fe₂O₃ and γ -Fe₂O₃ Debye temperatures are markedly different the intensity ratios will not be equal to the ratios of the actual amounts of α -Fe₂O₃ and γ -Fe₂O₃ present.

The error in the intensity ratios is approximately 10%, due

Fig. 5-5. Mössbauer spectrum of γ -Fe₂O₃ heated at 900°F for 15 hr. ¹⁰⁰

a¹ peak. 43% α -Fe₂O₃, 57% γ -Fe₂O₃



to uncertainties in the positions, widths, and heights of the separated peaks: these were caused both by the separation technique and by the inherent characteristics of the spectrometer itself. The errors in determining the furnace temperature with a thermocouple and the peak area with the planimeter were much smaller and can be neglected in comparison to the above figure.

The results are summarized in the table in Fig. 5-6. These may be represented (Daniels and Alberty 1961 p.297) by a first-order rate reaction expressed in the form

$$\frac{I_{\gamma}}{I_{\gamma} + I_{\alpha}} = e^{-mt} \quad (5-16)$$

where m is the rate constant at a given temperature,

t is the time,

I_{γ} is the intensity of γ -Fe₂O₃

and I_{α} is the intensity of α -Fe₂O₃.

Plotting $\ln \frac{I_{\gamma}}{I_{\gamma} + I_{\alpha}}$ against t for each temperature, four straight lines passing through the origin are obtained, each with a different slope- m .

Since kinetic data over a range of temperature can be represented (Daniels and Alberty 1961 p. 315) by the equation

$$m(T) = s e^{-T_A/T} \quad (5-17)$$

where m is the rate constant which depends upon temperature,

s is a constant, the frequency factor,

T_A is the activation temperature,

and T is the temperature,

plotting $\ln m$ against $1/T$ we obtain

Fig. 5-6. Summary of Results of the conversion rate determination.

TEMPERATURE (° K)	HEATING TIME (HR)	$\frac{I_{\gamma}}{I_{\gamma}+I_{\alpha}}$	HEATING TIME (HR)	$\frac{I_{\gamma}}{I_{\gamma}+I_{\alpha}}$	HEATING TIME (HR)	$\frac{I_{\gamma}}{I_{\gamma}+I_{\alpha}}$	HEATING TIME (HR)	$\frac{I_{\gamma}}{I_{\gamma}+I_{\alpha}}$	m (HR ⁻¹)
744	3	0.91	23	0.70	37.5	0.53	—	—	0.016
756	10	0.74	15	0.57	20	0.53	—	—	0.038
772	5	0.60	11	0.35	15	0.20	—	—	0.10
800	1	0.83	2	0.40	3	0.25	5	0.11	0.56

$$T_A = 35,200 \pm 100^\circ\text{K}$$

$$s = (6.6 \pm 0.5) \times 10^{18} \text{ hr}^{-1}$$

The relatively small magnitude of the errors indicates a reasonable degree of accuracy in the separation procedure, but it does not take into account the assumption of equal Debye temperatures for α -Fe₂O₃ and γ -Fe₂O₃.

VI. SUMMARY

This investigation has yielded the following information:

The magnetic fields at the nuclei of the iron atoms situated at the tetrahedral or A sites of the γ -Fe₂O₃ spinel lattice are of magnitude 489 ± 5 kOe, while at the octahedral or B sites they are 499 ± 5 kOe. When the γ -Fe₂O₃ is magnetized to saturation, these two fields are aligned antiparallel.

The isomer shifts relative to stainless steel are:

0.039 ± 0.004 cm/sec for the A-site spectrum, and 0.050 ± 0.003 cm/sec for the B-site spectrum.

The intensity ratio of the A-site spectrum to the B-site spectrum confirms the vacancy distribution of 3 cations in A sites to every 5 cations in B sites.

The time rate of temperature conversion for the reaction

γ -Fe₂O₃ \longrightarrow α -Fe₂O₃ can be predicted by assuming the equation $m(T) = s e^{-T_A/T}$ holds over the region of interest. The experimental values for the parameters s and T_A are $(6.6 \pm 0.5) \times 10^{18} \text{ hr}^{-1}$ and $(35.2 \pm 0.1) \times 10^3 \text{ }^\circ\text{K}$ respectively.

These results were presented by G. A. Sawatzky (G.A. Sawatzky et al. 1966) at the 1966 Summer Meeting of the American Physical Society, and have recently been published (R.J. Armstrong et al. 1966).

Thus, it is apparent that the Mössbauer effect, used as an investigation technique, provides a method for determining new data on γ -Fe₂O₃, and in addition, confirms previous measurements performed by different methods on the same material.

LIST OF REFERENCES

- Abragam, A., 1964 - L'Effet Mössbauer et ses applications à l'étude des champs internes. Gordon and Breach, Science Publishers, Inc., New York, N.Y., U.S.A.
- Armstrong, R.J., Morrish, A.H., and Sawatzky, G.A., 1966 - Phys. Letters 23, 414.
- Bauminger, R., Cohen, S.G., Marinov, A., Ofer, S., and Segal, E., 1961 - Phys. Rev. 122, 1447.
- Blasse, G., 1964 - Philips Res. Repts. Suppl. No. 3, p.3, 20.
- Born, M., and Von Karman, Th., 1912 - Phys. Z. 13, 297.
- Born, M., and Von Karman, Th., 1913 - Phys. Z. 14, 15.
- Boyle, A.J.F., and Hall, H.E., 1962 - Rept. Prog. Phys. 25, 441.
- Brown, W.F., Jr., and Johnson, C.E., Jr., 1962 - J. Appl. Phys. 33, 2752.
- Compton, D.M.J., and Schoen, A.H., editors, 1962 - The Mössbauer Effect: Proceedings of the Second International Conference on the Mössbauer Effect held at Saclay, France on September 13-15, 1961. John Wiley and Sons, Inc., New York, N.Y., U.S.A.
- Curry, N.A., Johnston, G.B., Besser, P.J., Morrish, A.H., 1965 - Phil. Mag. 12, 221.
- Daniels, F., and Alberty, R.A., 1961 - Physical Chemistry, 2nd ed. John Wiley and Sons, Inc., New York, N.Y., U.S.A.
- Davidon, W.C., 1959 - Variable Metric Method for Minimization. ANL Report 5990, Revised Edition, Nov.
- Debye, P., 1912 - Ann. Physik 39, 789.
- Dekker, A.J., 1965 - Solid State Physics, 8th printing Prentice-Hall Inc., Englewood Cliffs, N.J., U.S.A.
- DePasquali, G., Frauenfelder, H., Margulies, S., and Peacock, R.N., 1960 - Phys. Rev. Letters 4, 71.
- Einstein, A., 1906a - Ann. Physik 22, 180.
- Einstein, A., 1906b - Ann. Physik 22, 800.
- Einstein, A., 1911 - Ann. Physik 34, 170.

- Ferguson, G.A., Jr., and Hass, M., 1958 - Phys. Rev. 112, 1130.
- Frauenfelder, H., 1962 - The Mössbauer Effect W.A. Benjamin, Inc., New York, N.Y., U.S.A.
- Garif'ianov, N.S., Zaripov, M.M., and Kozyrev, B.M., 1957 - Doklady Akad. Nauk S.S.S.R. 113, 1243 [translation: Soviet Phys. Doklady 2, 195].
- Goodenough, J.B., and Loeb, A.L., 1955 - Phys. Rev. 98, 391.
- Gorter, E.W., 1954 - Philips Res. Repts. 9, 295.
- Hanna, S.S., Heberle, J., Littlejohn, C., Perlow, G.J., Preston, R.S., and Vincent, D.H., 1960 - Phys. Rev. Letters 4, 28.
- Henry, W.E., and Boehm, M.J. 1955 - Phys. Rev. 101, 1253.
- Hodgman, C.D., ed., 1963 - Handbook of Chemistry and Physics, 44th ed. The Chemical Rubber Publishing Co., Cleveland, O., U.S.A.
- Jackson, J.D., 1955 - Can. J. Phys. 33, 575.
- Josephson, B.D., 1960 - Phys. Rev. Letters 4, 341.
- Kelly, W.H., Folen, V.J., Hass, M., Schreiner, W.N., and Beard, G.B., 1961 - Phys. Rev. 124, 80.
- Kistner, O.C., and Sunyar, A.W., 1960 - Phys. Rev. Letters 4, 412.
- Kittel, C., 1963 - Introduction to Solid State Physics, 2nd ed., 7th printing John Wiley and Sons, Inc., New York, N.Y., U.S.A.
- Lipkin, J., Schechter, B., Shtrikman, S., and Treves, D., 1964 - Rev. Sci. Inst., 35, 1336.
- Morrish, A.H., 1965 - The Physical Principles of Magnetism John Wiley and Sons, Inc., New York, N.Y., U.S.A.
- Morrish, A.H., Johnston, G.B., and Curry, N.A., 1963 - Phys. Letters 2, 177.
- Mössbauer, R.L., 1958a - Z. Physik 151, 124.
- Mössbauer, R.L., 1958b - Naturwissenschaften 45, 538.
- Mössbauer, R.L., 1959 - Z. Naturforsch. 14a, 211.

- Muir, A.H., Jr., Ando, K.J., and Coogan, H.M., Compilers, 1965 - Mössbauer Effect Data Index, Issue 3, North American Aviation Science Center, Thousand Oaks, Calif., U.S.A.
- Pound, R.V., and Rebka, G.A., Jr., 1959 - Phys. Rev. Letters 3, 554.
- Pound, R.V., and Rebka, G.A., Jr., 1960 - Phys. Rev. Letters 4, 274.
- Rossi, Bruno B., and Staub, Hans H., 1949 - Ionization Chambers and Counters Experimental Techniques, 1st ed. McGraw-Hill Book Co., Inc., New York, N.Y., U.S.A.
- Sawatzky, G.A., Armstrong, R.J., and Morrish, A.H., 1966 - Bull. Am. Phys. Soc. 11, 474.
- Schiff, L.I., 1955 - Quantum Mechanics, 2nd ed. McGraw-Hill Book Co., Inc., New York, N.Y., U.S.A.
- Schiffer, J.P., and Marshall, W., 1959 - Phys. Rev. Letters 3, 556.
- Shull, C.G., Strauser, W.A., and Wollan, E.O., 1951 - Phys. Rev. 83, 333.
- Watson, R.E., and Freeman, A.J., 1961 - Phys. Rev. 123, 2027.
- Wertheim, G.K., 1964 - Mössbauer Effect: Principles and Applications Academic Press Inc., New York, N.Y., U.S.A.
- Wertheim, G.K., and Buchanan, D.N.E., 1962 - The Mössbauer Effect Proceedings of the Second International Conference on the Mössbauer Effect held at Saclay, France on September 13-15, 1961 edited by D.M.J. Compton and A.H. Schoen John Wiley and Sons, Inc., New York, N.Y., U.S.A. p.136.
- Wilkinson, D.H., 1950 - Ionization Chambers and Counters. Cambridge University Press, Cambridge, England p. 149ff.